UNIVERSITÀ DEGLI STUDI DI MILANO

Scuola di Dottorato in Fisica, Astrofisica e Fisica Applicata
Dipartimento di Fisica

Corso di Dottorato in Fisica, Astrofisica e Fisica Applicata
Ciclo XXVII

Optimization of the production of terbium radionuclides for theranostic applications

Settore Scientifico Disciplinare: PHYS-06/A, PHYS-01/A, CHEM-03/A

Supervisore: Prof.ssa Flavia Maria GROPPI GARLANDINI

Co-Supervisore: Prof. Simone MANENTI

Coordinatore: Prof. Aniello MENNELLA

Tesi di Dottorato di:
Michele COLUCCI

Anno Accademico 2023/2024

Commission of the final examination:

External Member:
Prof. Alexandra IOANNIDOU

External Member:
Prof. Mariagabriella PUGLIESE

Internal Member:
Prof. Roberta VECCHI

Final examination:

Date 04/12/2024

LASA laboratory, Università degli Studi di Milano - Dipartimento di Fisica, and INFN Milano, Segrate (MI), Italy

Essere stati amati tanto profondamente ci protegge per sempre,
anche quando la persona che ci ha amato non c'è più.
È una cosa che ci resta dentro,
nella pelle.

– J. K. Rowling, Harry Potter e la Pietra Filosofale

Cover illustration:

The cover features Antonio Canova's *"Amore e Psiche"*, a masterpiece that embodies the themes of my research through different interpretations: the union of therapy and diagnostics in theranostics; the bond between vector and radionuclide forming a radiopharmaceutical; and the collision of particle and target in nuclear reactions, releasing energy symbolized by love and beauty.
Photo by Michele Colucci.

Internal illustrations:

Michele Colucci

MIUR subjects:

PHYS-06/A (ex FIS/07)

PHYS-01/A

CHEM-03/A

PACS:

25.40.-h (Nucleon-induced reactions)

25.45.-z (^{2}H-induced reactions)

25.55.-e (^{3}H-, ^{3}He-, and ^{4}He-induced reactions)

87.57.-b (Nuclear medicine imaging, dosimetry, labeling, metabolic studies)

82.80.Jp (Activation analysis and other radiochemical methods)

82.80.Bg (Chromatography)

Keywords:

Radionuclide production, Terbium, Theranostic, Nuclear Reactions, Production Cross-Sections, Health Physics, Radiochemistry, Radiopharmaceuticals

Contents

List of Figures

List of Tables

Aim of this work

Motivation

The discovery of artificial radioactivity by Frederic Joliot and Irene Curie in 1934 had an almost immediate impact on medicine. Currently, over 50 million nuclear medicine procedures are performed annually worldwide, utilizing artificially produced radionuclides for both diagnostic and therapeutic purposes. Unsealed radioactive sources are used to label radiopharmaceuticals, which accumulate in tissues of interest due to the biological pathways of the molecules they constitute. The emission of ionizing radiation from these radiopharmaceuticals can then be exploited either for diagnostic purposes – to localize the site of accumulation and determine the lesion's position and nature – or for therapeutic purposes, releasing sufficient energy to damage diseased tissue.

Theranostics integrates diagnostics and therapy to personalize treatment in nuclear medicine by using a pair of radionuclides linked (separately) to the same radiopharmaceutical – one for imaging and the other for therapy. To avoid variations in biodistribution, these theranostic pairs should ideally be chemically identical. The primary advantages of theranostics include the ability to evaluate the expression of therapeutic targets, provide precise imaging for treatment planning, quantify dose distribution in both tumors and healthy tissues using PET-based diagnostics, and monitor therapeutic progress while assessing heterogeneous target expression.

In radionuclide production for medical applications, optimization plays a critical role. The objective is to maximize the yield of the desired radionuclide while ensuring the highest purity. Radioactive contamination must be minimized, as any radiation from contaminants adds to the patient's total dose without contributing to diagnosis or therapy. Stable nuclei contamination should also be avoided since the number of available receptors in target cells is limited, and adequate doses must be delivered without saturating these receptors. Therefore, Radionuclidic Purity and Specific Activity are key parameters in this process.

When producing radionuclides via nuclear reactions induced by charged particles (e.g., in a cyclotron), several parameters can be adjusted to maximize both yield and purity. These parameters include the target material, particle type, beam energy, target thickness, irradiation time, and cooling period. Due to the impracticality of experimentally testing all these parameters, the activity produced on a thick target is calculated by integrating the thin target yield, which is in turn related to the nuclear reaction cross-section. Thus, determining the production cross-sections of the desired radionuclide and potential contaminants is the first fundamental step in the optimization process.

Among theranostic radionuclides under development, terbium isotopes (^{149}Tb, ^{152}Tb, ^{155}Tb, and ^{161}Tb) stand out due to their unique properties (Müller et al. [2018]).

- ^{149}Tb is a short-lived ($T_{1/2}$ = 4.12 h (NNDC [2023])) radionuclide and it is the only α-emitter of the Tb family. It is a candidate for targeted alpha therapy (TAT). Moreover, ^{149}Tb is also a β^+ emitter, allowing its detection through Positron Emission Tomography (PET) exams simultaneously with ^{149}Tb radiopharmaceutical administration.
- ^{152}Tb ($T_{1/2}$ = 17.5 h (NNDC [2023])) is a β^+ emitter that can be used as a diagnostic tool and for dosimetry and the monitoring of the distribution of the ^{149,161}Tb isotopes which act as the therapeutic counterparts.
- ^{155}Tb ($T_{1/2}$ = 5.32 d (NNDC [2023])) is a potential Single Photon Emission Computed Tomography (SPECT) candidate thanks to its gamma emissions at 86.55 keV (32 %) and 105.32 keV (25.1 %). It can be used for dosimetry calculation before therapy, for example in a matched pair with ^{161}Tb or ^{149}Tb. Moreover its intense Auger and conversion electrons emissions make it suitable for Auger Targeted Radiotherapy (TRT).
- ^{161}Tb ($T_{1/2}$ = 6.89 d (NNDC [2023])) mainly decays by emitting β^- particles, but it also has the characteristic of emitting Auger and conversion electrons. On average, 2.24 Auger and conversion electrons are emitted per β^- particle. This characteristic of ^{161}Tb could make it an alternative to ^{177}Lu for cancer treatment as it can have a higher killing potential if internalized within the cell.

Figure 1 provides a schematic overview of the nuclear properties and potential applications of these terbium isotopes in nuclear medicine.

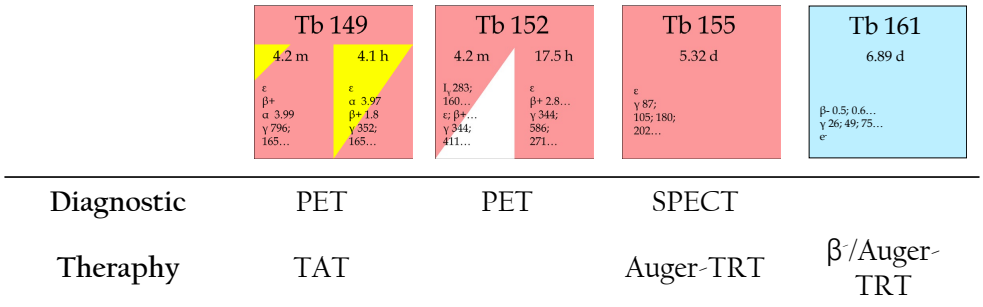

Figure 1: Nuclear properties of terbium radioisotopes and their potential application in nuclear medicine. Nuclear data from NNDC [2023].

The versatility of these theranostic radionuclides has earned them the title of "Swiss Army knife of nuclear medicine". However, their clinical use is limited by production challenges. Some isotopes (^{149}Tb, ^{152}Tb) are far from the stability line of the nuclide chart, and undesirable contaminants necessitate precise optimization of the production process. While ^{161}Tb can be efficiently produced using nuclear reactors, the remaining terbium isotopes are currently manufactured only through spallation reactions on heavy targets using high-energy proton beams (up to 1.4 GeV) coupled with online or offline mass separation systems. Only a few facilities worldwide, such as CERN-MEDICIS and

TRIUMF-ISAC, are capable of producing these radionuclides, and they currently cannot meet global demand.

Thesis Overview

Main Results

Driven by the motivations described above, the present Thesis aims to compare different production methods of theranostic radionuclides of terbium by determining the cross sections of the nuclear reactions for optimizing their yield and radionuclidic purity by combination of bombardment parameters. Three main reasons guided the selection of the five different nuclear reactions studied in this thesis: the absence or reduced number of nuclear data, the presence of discrepancies between different datasets, or the necessity of nuclear data for the characterization and optimization of a given production route. All the irradiations were performed at the cyclotron facility GIP ARRONAX (Saint-Herblain, France), while the activity measurements were done both at GIP ARRONAX and at LASA laboratory (Segrate, Italy). The main results are summarized below.

^{159}Tb(p,*x*): This nuclear reaction has been studied in the range 35–63 MeV and 19 cross-section points were obtained. Three other datasets were present in the literature (Engle et al. [2016], Steyn et al. [2014], Tárkányi et al. [2017]), covering part of the nuclear reactions studied here. None of them measured the cross-section of the reaction ^{159}Tb(p,x)^{154m1}Tb. The cross sections here determined are in accordance with the literature. The most important result of this part is the complete optimization, from the physical point of view, of the indirect production of ^{155}Tb obtained from the decay of ^{155}Dy. With an activity of 1.2 GBq$\cdot\ \mu$A^{-1} obtainable in 30 h of irradiation, and a potential radionuclidic purity higher than 99.9 %, this route represents one of the most favorable. A characterization from the radiochemical point of view is still required and is part of a future project at the LASA laboratory. Part of these results have been published in Colucci et al. [2024].

^{nat}Gd(α,*x*): Three previous datasets were also present in the literature. However, the production of ^{153}Dy, ^{151}Tb, ^{152}Tb was investigated here for the first time. In addition, the study by Gayoso et al. [1996] only discusses the production of terbium radionuclides, while the studies by Moiseeva et al. [2022] and Ichinkhorloo et al. [2021] stop at 60 MeV and 50 MeV respectively: in this work the energy range is extended up to 65 MeV. Even if the direct production of terbium theranostic radionuclides on natural gadolinium is not feasible, the indirect production of ^{155}Tb has been discussed and optimized: the purity is high, but the yields remain low due to the fact that the cross-section of the reaction ^{nat}Gd(α,x)^{155}Dy is not very high, and the use of enriched targets is suggested. This work will be extended at lower energies in the coming months with a new experiment already in progress and then published in a scientific journal.

^{nat}Eu(α,*x*): This nuclear reaction has been studied here for the first time. The energy range covered is 20–65 MeV, with a total of 18 points. Among the theranostic radioisotopes of terbium produced here are ^{149,152,155}Tb. For ^{149}Tb, the yield is very low, while for the others, the purity is not sufficient for medical applications. The production of ^{152}Tb on enriched ^{151}Eu was already discussed by Moiseeva et al. [2021]. Using simulations obtained with the TALYS 1.96 nuclear code (Koning and Rochman [2012]), the production of ^{152}Tb and ^{155}Tb on enriched ^{153}Eu targets was

investigated. The latter seems particularly advantageous in terms of produced activity (300 MBq/μA with an irradiation time of 5 days) and radionuclidic purity (>97 %). An experimental determination of the cross-sections for the reactions ^{153}Eu(α,x) is necessary to confirm these results. This work is in the final stages of preparation for submission to a scientific journal.

^{nat}Dy(p,x): The cross sections of these reactions have been studied for 13 points in the energy range between 35 and 57 MeV. Four different datasets were present, covering different energy ranges between 10 and 65 MeV (Tárkányi et al. [2013, 2015], Shahid et al. [2020], Červenák and Lebeda [2022]). Some discrepancies were present among these datasets; these have been investigated and discussed based on the new nuclear data presented in this work. This work is in the preparation phase for submission to a scientific journal.

^{nat}Dy(d,x): In the energy range between 12 and 32 MeV, where 16 points of cross-section data were obtained, only one work was present in the literature by Tárkányi et al. [2014a], with which good agreement was found in most cases. This work was discussed in two different publications (Colucci et al. [2022, 2023]).

In addition to this, a protocol for the radiochemical separation of trace amounts of Tb from a bulk material of Gd, with Dy contamination, was developed. Extraction chromatography was used with good results in terms of separation yield and the purity of the final product.

Organizational Note

The present Thesis consists of six chapters. Chapter 1 is an introductory chapter, providing an overview of the use of radionuclides in medicine and their production. In the same chapter, the family of terbium theranostic radionuclides is introduced with a brief review of the applications and current production capabilities.

Chapter 2 contains all the theoretical background necessary to understand this thesis: radioactive decay theory, the interaction of photons and heavy charged particles (p, d, α) with matter, nuclear reaction theory, and the equations necessary for determining the cross sections, including in the presence of complex decay schemes.

In Chapter 3, the experimental techniques are presented, including gamma and alpha spectrometry, the stacked-foils technique, and the working principles of ICP-OES. Furthermore, the facilities where all experiments have been performed are briefly described, i.e., the LASA laboratory (Segrate, Italy) and the GIP ARRONAX in Saint-Herblain (France).

The results are discussed in two separate chapters. In Chapter 4, all the cross-section measurements are presented and discussed, while in Chapter 5, the optimization of the most promising production routes is discussed, including the direct and indirect production of ^{155}Tb and the production of ^{152}Tb through the reaction ^{153}Eu(α, 5n). The optimization quantities, including the thick target yield, radionuclidic purity, and specific activity, are defined and discussed at the beginning of the same chapter.

Finally, in Chapter 6, the radiochemistry of terbium is introduced, with the definition of a separation protocol for Tb from bulk quantities of Gd.

CHAPTER 1

Introduction

Nine million seven hundred forty-three thousand eight hundred thirty-two is the number of people who died because of cancer in 2022 (for detailed data, see Global Cancer Observatory [2022]). This staggering number underscores the urgent need to address the global impact of this disease. Fortunately, advancements in scientific research offer hope in reducing mortality rates and enhancing the quality of life for cancer patients.

Since its early days, radioactivity has been used for medical applications. This chapter will show radioactivity's role in cancer diagnosis and cure, from the discovery of artificial radioactivity to the use of radiopharmaceuticals in nuclear medicine. At the end of the chapter, the terbium radionuclide's family will be introduced, being the main focus of this work.

1.1 Artificial radioactivity and medicine: a long story short

The discovery of artificial radioactivity in 1934 by Frederic Joliot and Irene Curie marked a significant breakthrough in nuclear science, as it was the first time a radioactive nuclide was synthesized and chemically identified at the scale of just a few atoms. The first radionuclide produced was ^{30}P obtained form the irradiation of thin aluminum foils with the α particles emitted by an intense polonium source. Nowadays we would write the reaction as ^{27}Al(α,n)^{30}P. They received the Nobel Prize in chemistry in 1935, 24 years after that Marie S. Curie received the same prize for the discovery of polonium and radium, that served as source for the discovery of artificial radioactivity.

The impact of artificial radioactivity on medicine was almost immediate after its discovery. By the late 1930s, artificial radionuclides had become central to several pioneering biological and medical research studies. For instance, Georg von Hevesy (George De Havesy in English), who had earlier suggested using radioisotopes as tracers in biological systems[1], utilized the artificially produced ^{32}P to study phosphorus metabolism. His groundbreaking work established the tracer principle, still central in modern nuclear medicine, that led to the development of diagnostic techniques such as positron emission tomography (PET) by the mid-20th century (McCready [2000]). Another important contribution from George De Havesy is its discovery that radioactive radionuclides cannot be chemically separated from the stable isotopes of the same element; in fact, he was not able to separate RaD (^{210}Pb) from natural lead (McCready [2000]).

In 1937, John Lawrence, known as the "father of nuclear medicine", began using ^{32}P to treat patients with polycythemia vera, a blood disorder characterized by an excess of red blood cells. This application marked one of the earliest therapeutic uses of artificial

[1] In 1924, George De Hevesy already performed experiments with rabbits using natural radioactive sources of bismuth-210, but he found that due to the toxicity of these elements, they were not adept for biological studies.

radioactive isotopes. By the 1940s, other artificial radioisotopes like iodine-131 (^{131}I) were being used both for the diagnosis and treatment of thyroid diseases, like thyroid carcinoma and hyperthyroidism, taking advantage of the ability of the thyroid gland to selectively uptake iodine (McCready [2000]).

The development of cyclotron technology in 1932 by Ernest Lawrence enabled the large-scale production of short-lived positron-emitting isotopes, including carbon-11 (^{11}C), oxygen-15 (^{15}O), and fluorine-18 (^{18}F). By the late 1940s, these isotopes had become indispensable in PET imaging, allowing for real-time metabolic process observation and unprecedented insights into human physiology and pathology. The introduction of these radionuclides significantly expanded the diagnostic capabilities of nuclear medicine, making it possible to detect cancer, assess myocardial perfusion, and investigate neurological conditions with far greater precision than previously possible (Guillaumont and Trubert [1995], McCready [2000]).

The production of artificial radionuclides through neutron activation during the late 1930s and early 1940s extensively diversified the available tools for nuclear medicine. Enrico Fermi's pioneering work with neutron capture reactions, starting in 1934, expanded the array of possible therapeutic and diagnostic radionuclides, establishing an approach that became particularly relevant with the advent of nuclear reactors in the 1940s (Guerra et al. [2012]). The discovery of technetium-99m (^{99m}Tc), which later became the most widely-used radionuclide of nuclear medicine due to its ideal physical and chemical properties, including a short half-life and gamma-ray emission suitable for imaging without excessive radiation dose, took place in 1937 (Guillaumont and Trubert [1995]).

In the last part of the 20th century, the utilization of artificial radioisotopes had become a routine part of medical practice, contributing to the diagnosis, staging, and treatment of numerous diseases. Today, radionuclides produced artificially are integral to advanced diagnostic imaging techniques, such as PET and single-photon emission computed tomography (SPECT), and to innovative therapeutic strategies, such as peptide receptor radionuclide therapy (PRRT) and targeted alpha therapy (TAT) (McCready [2000]).

1.2 Use of Radionuclides in Nuclear Medicine

In medicine, ionizing radiation produced by the decay of radionuclides is utilized across several sub-fields:

- **External Radiotherapy**: Historically, high-energy gamma emissions from sealed ^{60}Co sources have been used to treat tumors by exposing patients to a precisely shaped radiation field. This method, known as cobalt therapy, is still primarily used in developing countries. In most other regions, electron accelerators capable of generating high-energy X-rays have largely replaced cobalt sources (Page et al. [2014]). However, ^{60}Co continues to be employed in gamma-knife techniques for the precise treatment of small brain tumors (see Lindquist [1995] for more details).

- **Brachytherapy**: One of the earliest therapeutic applications of radionuclides is brachytherapy that originally used ^{226}Ra for treating skin and gynecological cancers. In brachytherapy, sealed radionuclide sources are placed inside or near the tissue to be treated, allowing for a uniform dose distribution within the desired volume through the emitted gamma radiation or atomic X-rays. Radionuclides such as ^{192}Ir and ^{60}Co are utilized in high-dose-rate (HDR) and pulsed-dose-rate

(PDR) treatments, often employing temporary stents to target tumors within lumens, such as the esophagus, or body cavities. Conversely, short-lived radionuclides like palladium-103 and iodine-125 are used in low-dose-rate (LDR) therapy, where permanent seeds containing radionuclides are implanted, commonly for prostate and ocular cancers. Technological advancements have significantly improved treatment accuracy and reduced radiation exposure to surrounding tissues (Lukens et al. [2014]).

- **Nuclear Medicine**: Unsealed radionuclide sources are used to label radiopharmaceuticals for both diagnostic imaging and therapeutic purposes (targeted radiotherapy). These radiopharmaceuticals accumulate within the tissue of interest due to the biological pathways of the molecules that constitute them, as explained in Section 1.3.

The radionuclides studied and discussed in this thesis are used for the latter technique in the list. Over 50 million nuclear medicine procedures are performed annually worldwide across more than 10,000 hospitals, with the number increasing each year. Of these procedures, 90 % are for diagnostic purposes, and the remaining 10 % are for therapeutic applications (World Nuclear Association [2024]).

Both nuclear imaging and radiotherapy rely on the tracer principle introduced by De Hevesy, which is based on the concept that radiopharmaceuticals administered in small quantities can produce high-contrast images or deliver therapeutic doses without significantly altering the organism's biochemistry. This approach is particularly beneficial for molecularly sensitive processes, such as metabolism, receptor binding, and cellular transport, that are influenced by even small amounts of external molecules (Mankoff [2019]). The following sections provide further details on these two types of procedures, and on the theranostic concept in nuclear medicine.

1.2.1 Diagnostic applications

Every organ has its own unique biochemistry, and biomolecules follow specific pathways within the body. The basic principle of nuclear imaging involves using radiolabeled biomolecules that are analogous to those already present in the organism. This allows for tracking their distribution throughout the body via emitted radiation, which enables the detection and quantification of organ function or abnormal physiology in various diseases (Mankoff [2019]).

In projection radiography and computed tomography (CT), images are generated by the transmission of X-rays passing through the patient. In contrast, images in Positron Emission Tomography (PET) and Single Photon Emission Computed Tomography (SPECT) are produced by the emission of gamma radiation from within the patient's body. In diagnostic applications, radiopharmaceuticals are labeled with radioisotopes that emit gamma photons, such as ^{99m}Tc[2] or ^{123}I (used in SPECT), or with isotopes that decay via β^+ emission, releasing positrons, like ^{18}F, ^{11}C, or ^{15}O (used in PET).

In PET, the emitted positron annihilates within the patient, producing two nearly back-to-back gamma photons with a specific energy of $E_\gamma = 511\,\text{keV}$ (positron annihilation is further explained in Section 2.1.3). These two photons define a line of response (LOR) and must be detected "simultaneously" by two scintillators positioned opposite each other relative to the annihilation point (see Figure 1.1).

[2] In diagnostic nuclear medicine, ^{99m}Tc is the most commonly used radionuclide, accounting for 80 % of all nuclear imaging procedures and 85 % of all nuclear medicine practices (World Nuclear Association [2024]).

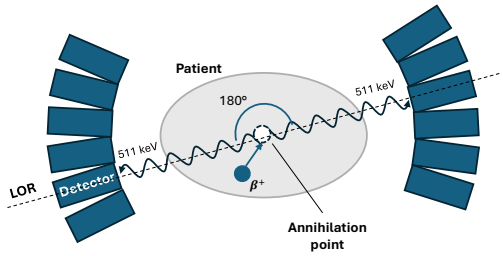

Figure 1.1: Positron emission, annihilation, and coincidence detection in PET scanners.

In SPECT, the detector system typically consists of a large NaI or CsI crystal scintillator, which converts absorbed gamma photons into visible light. This scintillator is optically coupled to a matrix of photomultiplier tubes (PMTs), which detect the scintillation photons that are spread across multiple PMTs. The interaction position within the crystal and the energy of the gamma photon are determined using the Anger logic technique. Here, each PMT signal is weighted by an impedance matrix to locate the centroid of the detected signals, and the signals are summed to determine the gamma photon's energy. If the energy is lower than that characteristic of the radionuclide injected into the patient, it indicates that the gamma photon has undergone Compton scattering and is, therefore, rejected. A multi-hole collimator is placed in front of the scintillator to reduce the number of scattered photons detected and to correlate the interaction position with the emission position within the patient. This entire system is known as a gamma camera or Anger camera. 3D tomographic images are obtained by rotating the gamma camera around the patient.

In PET, a ring geometry is used to optimize detection based on the symmetry of the emissions. The fundamental unit of a PET system is the block detector, which consists of a scintillating material block (e.g., BGO) with dimensions of $4 \times 4 \times 3\,\mathrm{cm}^3$, segmented into smaller pieces by longitudinal cuts. A greater thickness is needed due to the higher energy of the radiation, while segmentation improves spatial resolution. The scintillator is coupled to four PMTs, whose signals are weighted to determine the location of the segment where the interaction occurred. Tomographic algorithms, filtering, and corrections are essential steps in image processing that help produce the final diagnostic image.

One of the advantages of these techniques is their almost infinite contrast: the natural radioactivity within the body is very low, allowing a radiopharmaceutical to be easily distinguished from native molecules that provide no signal to the detectors. In contrast, other diagnostic techniques (e.g., computed tomography or magnetic resonance imaging) detect signals from all tissues, with contrast arising only from differences in signal intensity.

The image quality in PET and SPECT is generally lower than that achieved with X-ray systems, primarily due to the unknown location of the source, which is precisely the information sought in a nuclear medicine examination. Additionally, PET systems face unavoidable uncertainties, such as the finite range of the positron and the imperfect collinearity of the two emitted photons, resulting in lower spatial resolution (Volterrani

et al. [2010]). However, the functional information provided by these systems is not attainable with X-ray imaging, which instead offers precise morphological details. For this reason, several dual systems, such as SPECT/CT or PET/CT, have been proposed and are now clinically used to combine both diagnostic tools (Goldman [2007]).

Choice of radionuclides for imaging

The ideal diagnostic radionuclides should emit radiation with sufficient intensity to be easily detected, while minimizing low-penetrating radiation to reduce the patient's exposure to radiation (with positron emission being a necessary exception for PET applications). The half-life of the radionuclide should be appropriately matched to the time needed for the radiopharmaceutical to be administered and to accumulate in the target tissue, ensuring a strong signal during image acquisition. Afterward, the activity should rapidly decrease due to radioactive decay and the biological clearance of the radiopharmaceutical (Zanzonico [2019]).

For SPECT studies, radionuclides that decay via electron capture (EC) or isomeric transition (IT) and emit a strong gamma-ray within the 100–250 keV energy range are ideal. The lower limit of gamma-ray energy is determined by the attenuation properties of body tissues, while the upper limit is set by the detector's efficiency, which generally reaches its maximum around 150 keV. Additionally, the absence of corpuscular radiation is important to minimize the radiation dose to the patient. Two radionuclides that meet these criteria are the well-known ^{99m}Tc ($T_{1/2}$ = 6.0 h) and ^{123}I ($T_{1/2}$ = 13.2 h).

In PET studies, the energy of the emitted positron is a critical factor. The positron travels a certain distance within the tissue before being thermalized and annihilating with an electron. A high-energy positron with a long path length can degrade image resolution. Furthermore, gamma-rays with energies close to that of the annihilation photons should be absent, as they may interfere with the scan. Radionuclides with a high positron branching ratio are preferred to enhance counting statistics (Qaim [2020]). ^{18}F ($T_{1/2}$ = 109.8 min) is a radionuclide that satisfies all these requirements and is therefore widely regarded as the gold standard for PET imaging.

1.2.2 Targeted radiotherapy

The primary objective of targeted radiotherapy (TRT) is to deliver ionizing radiation specifically to the tissue requiring treatment, often to eradicate cancer cells, by utilizing the natural biological pathways of radiopharmaceuticals. This process can damage cancer cells either directly, by causing DNA damage such as single or double-strand breaks and cross-links, or indirectly, through the production of highly toxic reactive oxygen species (ROS) like hydroxyl radicals ($OH^{\bullet}$) resulting from the radiolysis of water. If these DNA damages are not adequately repaired, they can lead to apoptosis or other forms of radiation-induced cell death (Grzmil et al. [2019]).

TRT offers some advantages over other systemic treatments, such as chemotherapy. One key benefit is that the molecular doses of radiopharmaceuticals used in TRT are relatively low, minimizing the risk of non-specific off-target biochemical effects commonly associated with the high doses of chemotherapeutic agents. However, the effectiveness of TRT can be limited by the availability of suitable radiopharmaceuticals that specifically target the disease in question and by the potential toxicity to healthy organs involved in the transport and absorption of the radiopharmaceuticals, such as the kidneys, liver, and circulatory system (Mankoff [2019]).

Choice of radionuclides for TRT

Generally, radionuclides that emit corpuscular radiation, such as β^- particles, Auger electrons, or alpha particles, are required to deliver high radiation doses within a confined volume of tissue to achieve therapeutic effects (see Chapter 2 for a detailed explanation of the different decay modes).

Two key factors to consider are the linear energy transfer (LET) [$eV \cdot \mu m^{-1}$] to the tissue and the range of the corpuscular radiation. Alpha particles exhibit the highest LET (approximately 80 $keV \cdot \mu m^{-1}$), followed by Auger electrons (4-26 $keV \cdot \mu m^{-1}$), and β^- particles (0.2-2 $keV \cdot \mu m^{-1}$) (Grzmil et al. [2019]). A higher LET increases the likelihood of inducing double-strand breaks in DNA and enhances the concentration of ROS, both of which elevate the probability of cell death. Consequently, there is growing interest in targeted alpha therapy (TAT) (Sollini et al. [2020], Nelson et al. [2021]) to exploit the high LET of alpha particles.

The range of the emitted particles is also critical when designing radiopharmaceuticals. β^- particles typically have a range of several millimeters in biological tissues, whereas alpha particles have ranges on the order of tens of micrometers, depending on their energy. The range of Auger electrons is usually less than 5 µm (Grzmil et al. [2019]). Short-range radiation is more effective in treating small tumors, while longer-range radiation is more effective for larger tumors or those with heterogeneous characteristics. For instance, variations in vascularization can lead to uneven distribution of the radiopharmaceutical; in such cases, longer-range β^- particles can help achieve a more complete therapeutic response, through the so-called cross-fire effect.

The half-life of the radionuclide is also a crucial factor. In therapeutic applications, radionuclides with longer half-lives than those used for diagnostics are often selected. The physical half-life of the radionuclide should ideally match the biological half-life of the molecule to which it is bound. This alignment maximizes dose delivery to the tumor while minimizing the risks associated with a long-lived radionuclide circulating freely in the body. Common examples of half-lives for therapeutic radionuclides are 6.7 days for ^{177}Lu and 2.7 days for ^{90}Y.

Finally, it is important to consider whether the selected radionuclide has long-lived radioactive decay products that could accumulate in other parts of the body, including healthy tissues. For example, ^{225}Ac has excellent therapeutic properties as an alpha emitter, but its long decay chain may pose limitation on the maximum dose that could be safely administered.

1.2.3 The theranostic concept

Selecting an appropriate radionuclide for therapeutic applications should be customized to suit the specific type of cancer, the stage of the disease, and the individual patient's characteristics, including their response to treatment. This approach aligns with the broader trend toward more personalized medicine.

Traditionally, the selection of patients for a particular therapy is based on clinical parameters such as tumor stage or results from molecular biomarker tests. However, this approach often overlooks the unique characteristics of each patient, the potential heterogeneous distribution of molecular targets within the tumor, and does not facilitate a proper dosimetric evaluation.

Theranostics (*thera*py + diag*nostic*) partially addresses these challenges. In nuclear medicine, theranostics involves the use of a pair of radiopharmaceuticals — one for imaging and the other for subsequent therapy. This concept has been utilized in a limited

manner since the mid-20th century, particularly with the use of radioiodine for thyroid diseases. However, its potential expanded dramatically in the early 1990s with the introduction of versatile trivalent radiometals (e.g., ^{111}In and ^{90}Y) paired for SPECT imaging and TRT (Qaim et al. [2018]).

Ideally, to effectively overcome the limitations of conventional radiotherapy, the two radiopharmaceuticals in a theranostic pair should be chemically identical. Even slight differences in chemical structure can cause significant variations in biodistribution, off-target binding, and clearance times within the patient (Burkett et al. [2023]).

This challenge was addressed in 1992 at the Forschungszentrum Jülich in Germany, where a method was proposed using radionuclide pairs of the same element, such as ^{86}Y for PET imaging and ^{90}Y for therapy (Rösch et al. [2017]). Since then, many "true theranostic pairs" have been proposed, including ^{44g}Sc/^{47}Sc (Müller et al. [2018]), ^{64}Cu/^{67}Cu (Ahmedova et al. [2018]), and ^{72}As/^{77}As (Sanders and Cutler [2021]), as well as four terbium radioisotopes that will be discussed in detail in the next chapter and throughout this thesis (Müller et al. [2018]).

There are also examples of single radionuclides that are inherently theranostic, meaning they can be used for both diagnosis and therapy. ^{64}Cu is one of the most notable examples (Boschi et al. [2018]). Among the terbium isotopes, ^{149}Tb and ^{155}Tb also hold significant potential in this regard (Müller et al. [2018]).

On the other hand, it remains common practice to conduct theranostic studies using radionuclides from different elements with similar chemical properties, such as the ^{68}Ga/^{177}Lu pair (Weineisen et al. [2015]).

The key advantages of theranostics can be summarized in five main points (Bodei et al. [2022]):

1. The use of a diagnostic agent allows for evaluating the expression of the therapeutic target on the cells, determining whether the accumulation of the radiopharmaceutical in a specific patient and tumor is effective. It enables clinicians to "treat what you see" by providing a clear image of the tumor's location and burden.

2. When a PET radionuclide is used as the diagnostic agent, it allows quantification of the dose delivered to both the tumor and healthy tissues.

3. It allows a followup on the progress of the therapy.

4. It helps assess the extent of heterogeneous target expression within the tumor, allowing clinicians to select a therapeutic radionuclide with particles that have a long range to exploit the cross-fire effect — a strategy not feasible with non-radioactive molecular therapies.

5. Finally, it reduces the risk of failure in the development of new ligands in oncology, where the failure rate is typically very high (90 % of drugs do not progress from preclinical to clinical stages). Early biodistribution studies using diagnostic agents can inform and expedite the development of new radiopharmaceuticals.

1.3 Radiopharmaceuticals: definitions and mode of action

A radiopharmaceutical is usually composed of two elements: a radioactive atom and, eventually, a molecule of biological interest called a vector. Different molecules can serve as vectors, including organic molecules, antibodies, sugars, etc. The role of the vector is to transport the radionuclide to the target of interest (e.g., the cancer tissues). Few

radionuclides do not require a vector; for example, the thyroid has an excellent uptake for iodine naturally. Therefore, ^{131}I for the therapy of thyroid issues does not require a vector and it is usually administered in form of [^{131}I]-NaI, or ^{201}Tl behaves chemically like potassium and therefore, it accumulates in the muscular tissues.

In all the other cases, a radiolabeling process is required, where the radionuclide is connected to the vector either via a simple covalent bond or via a complexation bond. The former is generally used for carbon radioisotopes (i.e. ^{11}C) that is abundantly present in biological molecules, or for elements belonging to the halogens (e.g., iodine or fluorine), and an outstanding example is the ^{18}F-FDG (fluorodeoxyglucose) commonly used for PET imaging of tumors. It is a glucose analogue, i.e. a glucose molecule where a hydroxyl group (OH^-) is substituted by ^{18}F, as shown in Figure 1.2. Instead, complexation chemistry is used for radioisotopes of cationic metal elements, e.g., ^{99m}Tc or yttrium-90 (^{90}Y). It consists of the formation of multiple bonds between the radionuclide and the negative ions of the molecule that form a complex. Not all molecules dispose of the negative ions for the complexation of the radionuclide; therefore, to "functionalize" a vector, it is necessary to add a complexation cage as in the case of the peptide (DOTATOC) shown in Figure 1.2. After radiolabeling, quality control (QC) must be performed to determine the percentage of radionuclide bonded to the molecule. Failure in complete bonding would result in free radionuclides within the body that compromise the quality of the image or the outcome of the therapy, resulting in a higher dose to healthy tissues.

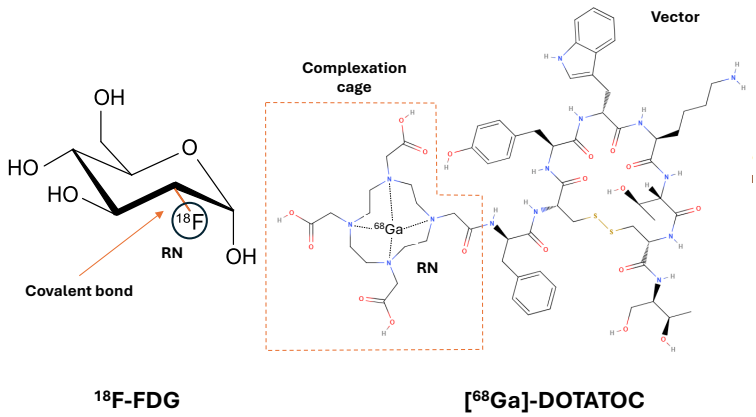

Figure 1.2: Examples of radiolabeling of radiopharmaceuticals exploiting the formation of covalent bonds (left) to realize ^{18}F-FDG or complexation chemistry to link ^{68}Ga to DOTATOC.

The molecular paradigm underlying the functioning of radiopharmaceuticals is based on the idea that diseased or damaged cells differ from their healthy counterparts, exhibiting a unique "phenotype" or signature characterized by altered metabolic state or physiological function. This distinctive pattern would be consistent among cells of similar origin undergoing the same disease process. As a result, molecular targeting can be described as the selective accumulation of a diagnostic tracer or therapeutic agent, achieved through its interaction with a molecular entity (target) that is specifically present or absent in diseased cells or tissues (Britz-Cunningham and Adelstein [2003]).

There are various mechanisms that enable the fixation or accumulation of radiopharmaceuticals in cells or tissues where the target is expressed. A thorough understanding

of the molecular pathology is essential for developing new radiopharmaceuticals. Two examples of these mechanisms are provided below:

- **Receptor–ligand interaction:** In this mechanism, the radiopharmaceutical binds with high affinity to a specific site on the target. This occurs, for instance, with small peptides that bind to overexpressed receptors on cancer cells or with antibodies that selectively bind to specific antigens. An example is the overexpression of somatostatin receptors in many neuroendocrine tumors. Radiopharmaceuticals based on somatostatin analogs (i.e., molecules similar to somatostatin) are available and can be labeled with various radionuclides, including ^{68}Ga for PET imaging or lutetium-177 (^{177}Lu) for therapy (Eychenne et al. [2020]).
- **Transporter–substrate interaction:** Here, the signaling molecule is concentrated within a cell or tissue compartment via a metabolic process. A key example is ^{18}F-FDG, a glucose analog that allows for the monitoring and visualization of cellular glucose metabolism. It indirectly highlights cancerous tissues, as their rapid growth requires a high energy intake from glucose. ^{18}F-FDG enters cells through the GLUT1 transporter present on the cell membrane and undergoes phosphorylation like normal glucose, preventing it from leaving the cell. However, unlike glucose, it is not recognized by the enzymes that degrade glucose, resulting in its accumulation within the cell (Avril [2004]).

1.4 Production of medical radionuclides

As highlighted in Section 1.1, most of the radionuclides used in nuclear medicine must be produced artificially, not being present in nature. The most common production routes involve the use of particle accelerators, mainly cyclotrons, and nuclear reactors, where nuclear reaction processes, discussed in Chapter 2, take place. Also the generator method is often used, but it still requires that the parent of the radionuclide of interest is produced through one of the two aforementioned methods. These three production routes are described in the following paragraphs.

1.4.1 Reactor based production

Nuclear reactors typically provide a high flux of neutrons (ϕ) that can be utilized for producing radionuclides for medical applications. However, this process generally involves only medium-power reactors (6–30 MW power, $\phi = 1\text{–}5 \times 10^{14}$ neutrons·cm^{-2}·s^{-1}) (Qaim [2020]).

The target material is usually in solid form contained in an inert ampule, and it is inserted into the reactor pool via a hydraulic system during normal operations, allowing the irradiation to be considered isotropic. During irradiation, the production rate of a specific nuclide (R) is proportional to the number of target atoms (N_t) and the neutron flux through the cross-section σ, measured in cm^2, which represents the probability of a given reaction (this will be discussed in detail in Section 2.4). When accounting for the decay of the radionuclide, the resulting activity (A, in becquerels [Bq]) is given by:

$$A = N_t \cdot \phi \cdot \sigma \cdot \left(1 - e^{-\lambda t}\right) \tag{1.1}$$

where λ is the decay constant of the radionuclide. The term in parentheses is often referred to as the saturation factor, which limits the utility of irradiation times much longer than the half-life of the radionuclide. The cross-section is, in principle, dependent on the

neutron energy; however, neutrons do not lose a significant amount of energy within the material thickness, so the cross-section remains relatively constant. Nevertheless, if the cross-section is very high, two phenomena can occur: "target burnout", i.e. a significant reduction of the number of target nuclei due to nuclear transformations, and "target self-shielding," a reduction of neutron flux in the central part of a thick target due to absorption in the outer layers. Furthermore, if the product also has a high cross-section for neutron interaction, "product burnout" can occur due to secondary reactions involving the product itself. All these factors reduce production yield and must be considered when optimizing the process.

The primary reactions occurring with thermal neutrons are elastic and inelastic scattering, as well as radiative capture. Elastic scattering is not helpful as it does not change the target into a different product. Inelastic scattering can produce metastable states of a nucleus but is rarely utilized. Radiative capture, which involves neutron capture followed by photon emission, is widely used for radionuclide production. However, this process results in a product that is an isotope of the target nucleus, making them chemically indistinguishable and inseparable, leading to low purity. With the definitions presented in Chapter 5, we would describe this as a low-specific activity product. Some strategies to improve purity include (Qaim [2020]):

- **Precursor/Generator**: A radiative capture process produces a precursor of the desired radionuclide, which is obtained through its decay. After radioactive decay, the product is a different chemical species, allowing for separation and achieving a high-specific activity product. For example, lutetium-177 (^{177}Lu) can be produced directly through the reaction n + ^{176}Lu, yielding low specific activity but high yield, or indirectly via n + ^{176}Yb $\rightarrow$ ^{177}Yb $\rightarrow$ ^{177}Lu. Depending on the application and facility capabilities, both routes are utilized (Radford and Lapi [2019]).

- **Szilard-Chalmer's Process**: Neutron capture followed by gamma emission may break the molecular bonds of the target material, causing some of the product to form a different chemical compound from the target, enabling separation. This process is seldom used today.

Another significant process is neutron-induced fission. For example, ^{99}Mo is produced from the fission of uranium-235 ^{235}U induced by thermal neutrons, which accounts for 6.1 % of the events. ^{99}Mo is not used directly but serves as a generator for ^{99m}Tc, as explained in the next section. ^{131}I and ^{90}Sr are also produced in this way. The purity is very high, but a complex chemical process is required to extract the desired radionuclide from all the fission products.

The (n,p) reaction, in which a neutron is captured followed by proton emission, is used to produce a few important radionuclides including ^{64}Cu from ^{64}Ni and ^{32}P ^{32}S. This reaction requires high-energy neutrons (E $>$ 1 MeV), and the neutron flux at this energy is four to five orders of magnitude lower than for thermal neutrons in reactors. Nonetheless, radionuclides produced this way have high specific activity because they are chemically different from the target.

Radionuclides produced by neutron-induced reactions are generally neutron-rich and undergo β^- decay and are used in radiation therapy or SPECT imaging.

1.4.2 Direct activation using charged particles accelerators

The primary focus of this thesis is the production of radionuclides using nuclear reactions induced by light ions accelerated by cyclotrons. Consequently, the description

of nuclear reactions, production yields, and the purity of the products are thoroughly covered in the next chapters. In this section, the main differences from reactor-based production processes are highlighted, and technical details related to producing large quantities of radionuclides for clinical use are provided.

Globally, there are over 1200 accelerators capable of accelerating protons up to 18–20 MeV that are either partially or entirely dedicated to the production of medical radionuclides (Synowiecki et al. [2018]). Many of these cyclotrons are located directly in hospitals, allowing for on-site production of short- or medium-lived radionuclides for imaging purposes, such as ^{11}C, ^{18}F, and ^{64}Cu (Qaim [2020]). Other significant radionuclides are produced in higher-energy cyclotron facilities ($E \leq 100$ MeV), which may also accelerate deuterons and helium nuclei. An example is the Arronax cyclotron (Haddad et al. [2008]), where all of our experiments were conducted. These radionuclides include alpha emitters like ^{211}At and ^{225}Ac, as well as ^{67}Cu and ^{111}In.

One of the main differences from reactor-based production is that charged particles rapidly lose energy within the target due to Coulomb interactions. This results in a change in the cross-section within a thick target and more complex equations are needed to relate the cross-section to the produced activity, as it will be explained in Chapter 5. Furthermore, the energy lost within the target material is converted into heat, which must be dissipated using efficient cooling systems, making the target stations quite complex.

Targets can be in gas, liquid, or solid states. This thesis focuses only on solid targets; however, there are certain advantages to using gas or liquid targets. The most significant is that they can be easily transported from the target station to the hot cell for processing through a tube system, and they do not require dissolution, which is mandatory for solid targets. However, the choice of materials must be carefully made to avoid interactions with the target or the produced radionuclides, preventing material loss due to binding on the walls or degradation of the sample holder (Radford and Lapi [2019]). An example of a radionuclide produced from the liquid sample is ^{18}F, obtained by irradiation of water targets where natural oxygen is enriched in ^{18}O.

A notable difference between reactor- and cyclotron-produced radionuclides is the maximum achievable activity. In reactors, both high neutron fluxes and cross-sections lead to very high yields. In contrast, the current of the cyclotron beam is limited by the maximum power that can be dissipated by the target, typically up to 1 mA (more commonly in the range of hundreds of µA).

The advantages of using cyclotrons to produce radionuclides include the ability to produce neutron-deficient nuclei that decay by β^+ emission, suitable for PET studies. Additionally, common biological elements (e.g., carbon, nitrogen, oxygen) have very low neutron capture cross-sections, so their radioactive isotopes can only be produced by cyclotrons (Qaim [2020]). Finally, radionuclides produced by cyclotrons generally have a higher charge state than the target material, simplifying chemical separation.

Another accelerator-based production method, not explored in this thesis, involves spallation reactions induced by high-energy protons ($E > 1$ GeV) on heavy targets, such as tantalum. This process is utilized in facilities equipped with such high-energy beams, like CERN MEDICIS in Switzerland (Bernerd et al. [2023]), and is generally combined with an online mass separation system to separate different isotopes of the same element that are co-produced during irradiation (the ISOL technique). It is worth noting that the ISOL technique, where available, can also be applied to targets irradiated with neutrons, lower energy protons, or other light ions.

Several limiting factors prevent the widespread use of this technique, including the limited availability of such specialized equipment in typical laboratories and the rela-

tively low efficiency of radionuclide recovery. However, ongoing research is focused on improving recovery efficiency to make this method more viable.

1.4.3 Generator technique

The generator technique relies on a long-lived radionuclide bound to a matrix, which decays to produce the desired short-lived radionuclide. This radionuclide is then isolated through a separation process, enabling rapid availability in hospitals and ensuring a continuous supply.

The most widely used generator is the ^{99}Mo/^{99m}Tc systems that utilizes column chromatography, in which ^{99}Mo, as molybdate (MoO_4^{2-}), is adsorbed onto an acid alumina (Al_2O_3) column. As ^{99}Mo decays, it forms pertechnetate (TcO_4^-), which, due to its single negative charge, binds less tightly to the alumina. By passing a saline solution through the column containing the immobilized ^{99}Mo, the soluble ^{99m}Tc is eluted, resulting in a saline solution of pertechnetate with sodium as the counterion (Radford and Lapi [2019]).

The equation describing the growth of the activity of the decay product in a generator will be derived in Chapter 2. The result is anticipated here:

$$A_2 \propto A_1^0 \left(e^{-\lambda_1 t} - e^{-\lambda_2 t}\right) \tag{1.2}$$

where A_2 is the activity of the decay product and A_1^0 is the initial activity of the parent radionuclide at the time of the last elution. Given the half-lives of ^{99}Mo (2.75 days) and ^{99m}Tc (6.0 hours), the maximum activity of ^{99m}Tc is reached approximately 24 hours after elution. Consequently, in clinical practice, elution is typically performed once per day, and the generator is used for about one week, after which the activity of ^{99}Mo becomes insufficient.

Other commonly used generators include ^{68}Ge/^{68}Ga, ^{82}Sr/^{82}Rb, and ^{90}Sr/^{90}Y (Qaim [2020]). In the first two cases, the parent radionuclides are produced by irradiation with charged particles, while in the last case, it is produced in reactors.

1.5 Terbium radioisotopes: the "Swiss army knife" of nuclear medicine

Terbium has emerged as a highly versatile element in nuclear medicine due to its multiple radioisotopes, which cover both diagnostic and therapeutic modalities. Its isotopes, ^{149}Tb, ^{152}Tb, ^{155}Tb, and ^{161}Tb, possess complementary decay properties that make them uniquely suitable for radiotheranostics. These distinctive characteristics have led to terbium being renamed the "*Swiss army knife of nuclear medicine*" (Müller and van der Meulen [2024]). In this section, the decay characteristics, specific applications, and the current status of preclinical, proof-of-concept, and clinical studies for each terbium isotope will be described. While this overview is not exhaustive, given the growing number of publications on the subject, it aims to provide a comprehensive summary of the key findings.

1.5.1 Terbium Radionuclides: nuclear properties and possible applications

The four radionuclides of terbium discussed – ^{149}Tb, ^{152}Tb, ^{155}Tb, and ^{161}Tb – span the characteristics necessary for modern nuclear medicine radionuclides, with properties that are useful for both imaging and therapy. Table 1.1 provides a comprehensive summary of their decay properties, including half-lives, emitted particles, and their energy.

Table 1.1: Properties of the four theranostic terbium isotopes. Electron (β^-, Auger and Conversion Electrons) and positron (β^+) energies are averaged on the different possible emission. Data taken from NNDC [2023].

RN	$T_{1/2}$	Decay mode (BR %)	E_α [MeV]	$E_{\beta/AU/CE,\ avg}$ [keV]	E_γ [keV] (I_γ [%])	Application
^{149}Tb	4.12 h	α (16.7) β^+ (7.1) EC (76.2)	6.967	720 (7.1 %)	352.2 (29.4) 165.0 (26.4) 388.6 (18.4) 652.1 (16.2)	TAT PET
^{152}Tb	17.5 h	β^+ (20.3) EC (79.7)	-	1140 (20.3 %)	344.3 (63.5) 271.1 (9.5) 586.3 (9.2) 778.9 (5.5)	PET
^{155}Tb	5.32 d	EC (100)	-	AU/CE 18.9 (203 %)	86.6 (32.0) 105.3 (25.1) 180.1 (7.5) 262.3 (5.3)	Auger-TRT SPECT
^{161}Tb	6.89 d	β^- (100)	-	154 (101 %) AU/CE 18.8 (226 %)	25.6 (23.2) 48.9 (17.0) 74.6 (10.2)	β^- and Auger-TRT

Each terbium isotope has unique potential applications in nuclear medicine, ranging from diagnostic imaging (PET, SPECT) to targeted radionuclide therapy.

^{149}Tb

^{149}Tb is a highly promising radionuclide for targeted α-particle therapy (TAT) due to its α emissions, which provide a high linear energy transfer (LET) leading to efficient tumor cell killing with minimal damage to surrounding tissue. Additionally, the β^+ emissions enable PET imaging, making ^{149}Tb suitable for theranostics (Müller et al. [2018], Laere et al. [2024]).

In preclinical studies, ^{149}Tb has been used with radiolabeled antibodies, such as ^{149}Tb-rituximab for treating Burkitt leukemia in mouse models. These studies demonstrated significant tumor growth inhibition and increased survival time in treated animals compared to controls (Beyer et al. [2004]). Furthermore, ^{149}Tb has also been tested in folate receptor-targeted therapy using ^{149}Tb-labeled DOTA-folate conjugates in tumor-bearing mice, where an improved survival times were observed (Müller et al. [2014b]).

The potential of ^{149}Tb for PET-based biodistribution verification has also been explored. A proof-of-concept study with ^{149}Tb-DOTANOC demonstrated that, due to its positron emission, it could be used for PET imaging of somatostatin receptor-positive tumors in preclinical models (Müller et al. [2017]).

^{152}Tb

^{152}Tb is a positron-emitting radionuclide (β^+) with a relatively long half-life of 17.5 hours, making it ideal for PET imaging, particularly in applications requiring extended imaging times or long-circulating radiopharmaceuticals such as antibodies (Müller and van der Meulen [2024]).

Various targeting vectors have been successfully labeled with ^{152}Tb, such as ^{152}Tb-DOTATOC, which was used in the first in-human study of terbium radionuclides for PET imaging. In this clinical proof-of-concept, a patient with a neuroendocrine tumor was imaged using ^{152}Tb-DOTATOC. The imaging allowed the clear visualization of metastases, including small lesions, and demonstrated excellent tumor-to-background contrast, especially at delayed time points (Baum et al. [2017]). The extended half-life of ^{152}Tb compared to ^{68}Ga makes it especially useful in cases where slow accumulation of a vector occurs and longer imaging windows are needed.

Preclinical studies have also demonstrated that ^{152}Tb can be used for dosimetry prior to therapy. For instance, in somatostatin receptor-positive AR42J rat tumor models, ^{152}Tb-DOTANOC showed biodistribution profiles similar to those of ^{177}Lu-DOTANOC, indicating that ^{152}Tb could be used effectively for pre-therapeutic imaging (Müller et al. [2016]).

^{155}Tb

^{155}Tb, with its electron capture decay and gamma emissions, is an excellent candidate for SPECT imaging. Its half-life of 5.32 days provides flexibility for diagnostic imaging protocols, and its gamma emissions (87 keV, 105 keV) are well-suited for high-quality SPECT images (Müller et al. [2018]). Moreover its intense emission of Auger and conversion electrons make it suitable for therapeutic applications (Duchemin et al. [2016]).

In preclinical studies, ^{155}Tb has been used with various biomolecules, including peptides and antibodies, for SPECT imaging. For example, ^{155}Tb-DOTATATE has been explored for imaging in preclinical models of tumor-bearing mice. The images obtained showed high contrast and good spatial resolution, comparable to ^{111}In-labeled analogs, but with improved characteristics for dosimetry and tumor delineation (Müller et al. [2014b]).

^{155}Tb has also been proposed as a dosimetry tool prior to ^{177}Lu or ^{161}Tb therapy. By using ^{155}Tb for SPECT imaging, clinicians can calculate the absorbed dose to the tumor and surrounding tissues, optimizing the therapeutic regime (Müller et al. [2014b]).

^{161}Tb

^{161}Tb is regarded as one of the most promising isotopes for targeted radionuclide therapy (TRT). Its β^- emissions are similar to those of ^{177}Lu, making it suitable for similar applications. However, ^{161}Tb also emits Auger electrons, which deposit energy over very short distances, leading to enhanced cell killing within the tumor while minimizing damage to surrounding healthy tissues.

In preclinical studies, ^{161}Tb has been used for both imaging and therapy. For instance, ^{161}Tb-labeled somatostatin analogs have shown excellent therapeutic efficacy in tumor models (Müller et al. [2018]). When compared directly to ^{177}Lu, ^{161}Tb demonstrated superior tumor growth inhibition, largely due to the additional contribution of Auger electrons to the radiation dose delivered at the cellular level, while maintaining comparable biodistribution and clearance (Müller et al. [2014a, 2023]).

Moreover, ^{161}Tb has already been used for the firsts in-human applications of ^{161}Tb-PSMA-617 and ^{161}Tb-DOTATOC, obtaining images that enabled the identification of all the lesions highlighted using ^{68}Ga-DOTATOC (Baum et al. [2021], Al-Ibraheem et al. [2023]). A recent review highlighted the potential of ^{161}Tb in overcoming limitations associated with ^{177}Lu, especially in treating micrometastases and single cancer cells that may not respond sufficiently to ^{177}Lu due to its longer radiation path length (Kong et al.

[2024]). Initial clinical trials indicate ^{161}Tb's promising biodistribution and enhanced efficacy in patients who did not respond to ^{177}Lu therapy.

The list of clinical applications for ^{161}Tb continues to grow, as discussed in recent reviews (Müller et al. [2023], Laere et al. [2024]), supporting its development as a viable option in TRT with a potentially improved therapeutic profile.

1.5.2 Production of Terbium Radioisotopes

The clinical use of certain terbium medical radioisotopes is currently limited due to difficulties in their production. Several authors have reviewed the production methods of these radionuclides, including Müller et al. [2018], Qaim et al. [2018], Naskar and Lahiri [2021], Kazakov [2022], Laere et al. [2024], Colombi and Fontana [2024]. Here, some of the key results are summarized.

Production of ^{149}Tb

The production of terbium-149 is challenging, with the most effective method relying on proton-induced spallation of tantalum targets. At facilities such as CERN-ISOLDE, tantalum foils are irradiated with high-energy protons, typically 1.4 GeV, followed by mass separation of the produced radiolanthanides (Duchemin et al. [2021a,b], Favaretto et al. [2024]). The radiolanthanides are ionized, accelerated, and implanted onto thin layers of materials such as aluminum or NaCl. In on-line production, ^{149}Tb is also generated through the decay of short-lived Dy-149, which is co-produced during the irradiation process. However, a significant drawback of this method is that only a few centers can provide such high-energy proton beams; besides MEDICIS at CERN, ISAC at TRIUMF (Canada) is one of the few facilities capable of this (Fiaccabrino et al. [2021]). Moreover the presence of pseudo-isobars such as cerium-133m oxides necessitates of further chemical purification through cation exchange chromatography.

Alternative methods, such as irradiating europium targets with ^{3}He nuclei, have also been explored. The ^{151}Eu(^{3}He,5n)^{149}Tb reaction shows promising yields of up to 230 MBq/µA but also produces a range of terbium isotopes with longer half-lives, such as $^{150, 151, 152}$Tb. Although feasible for preclinical studies, this method is unsuitable for large-scale production due to its inability to produce ^{149}Tb with high purity (Zagryadskii et al. [2017], Moiseeva et al. [2021]). Similarly, the reactions ^{151}Eu(α, 6n)^{149}Tb (Moiseeva et al. [2021]) and ^{152}Gd(p, 4n)^{149}Tb (Steyn et al. [2014]) result in a low-purity product due to the unavoidable co-production of longer-lived contaminants. Additionally, the latter reaction requires expensive highly enriched material as the natural abundance of ^{152}Gd is only 0.20 %.

Production of ^{152}Tb

^{152}Tb is most efficiently produced via high-energy proton-induced spallation of tantalum targets, similar to ^{149}Tb. This method has been optimized at ISOLDE, yielding several hundred MBq of ^{152}Tb (Allen et al. [2001]). However, the limited availability of high-energy accelerators capable of sustaining this process restricts its wider application.

Another approach for producing ^{152}Tb involves proton irradiation of highly enriched ^{152}Gd targets (99.9 %) at 12 MeV, which has shown potential in terms of yield and purity (Vermeulen et al. [2012a], Köster et al. [2020]). However, the low natural abundance of ^{152}Gd makes this method costly and less viable for routine production. Simulations suggest that the production of ^{152}Tb using the ^{155}Gd(p,4n) reaction may result in purity

levels lower than 50 % (Vermeulen et al. [2012a], Steyn et al. [2014]). Additionally, the reactions ^{151}Eu(^{3}He, 2n) and ^{151}Eu(α, 3n) have been studied, yielding approximately 200 MBq/µA and 180 MBq/µA, respectively, for a 17-hour-long irradiation. However, the purity remains below 80 % (Moiseeva et al. [2021, 2022]).

Production of ^{155}Tb

Like the other two radionuclides, ^{155}Tb can be produced via high-energy proton irradiation of heavy targets, followed by mass separation techniques (Webster et al. [2019]).

Alternatively, ^{155}Tb may be produced using various methods, primarily light particle reactions such as proton, deuteron, or alpha-particle bombardment of natural or enriched gadolinium targets (natural: Vermeulen et al. [2012b], Tárkányi et al. [2014b], Gayoso et al. [1996], Ichinkhorloo et al. [2021]; enriched in ^{155}Gd or ^{156}Gd: Dellepiane et al. [2022], Wang et al. [2023]). Using natural targets results in significant co-production of contaminants, particularly ^{156g}Tb, whose half-life of 5.35 days does not allow for its removal by decay to obtain pure ^{155}Tb. Better purity is achieved with enriched targets, though it still does not exceed 93 %, primarily due to less than 100 % enrichment.

Indirect production methods are also possible: first, the precursor ^{155}Dy is produced through nuclear reactions, followed by its decay into ^{155}Tb, which is then extracted and purified from the Dy. This method is discussed extensively in Chapter 5. One of the most promising methods involve using enriched ^{155}Gd targets irradiated with an α beam, allowing the production of 50 MBq/µA of pure ^{155}Tb in 11 hours of irradiation (Moiseeva et al. [2023]). A similar process applies to the reaction ^{159}Tb(p, 5n)^{155}Dy with a maximum yield of 1.6 GBq/µA, as discussed in Colucci et al. [2024] and further elaborated in this thesis.

Using ^{nat}Dy for direct and indirect production of ^{155}Tb is generally disadvantageous due to the low yield and purity of the products (Gayoso et al. [1997], Tárkányi et al. [2014a, 2015], Colucci et al. [2022]).

Production of ^{161}Tb

The production of ^{161}Tb primarily occurs via thermal neutron capture on highly enriched ^{160}Gd targets. In this process, neutron irradiation forms short-lived ^{161}Gd, which decays into ^{161}Tb. This production route is highly efficient in nuclear reactors, particularly in environments with high thermal neutron flux, and generates ^{161}Tb with high radionuclidic purity (Lehenberger et al. [2011]).

Cyclotron production of ^{161}Tb using deuteron-induced reactions on ^{160}Gd targets has also been explored. The reactions ^{160}Gd(d,n)^{161}Tb and ^{160}Gd(d,p)^{161}Gd$\rightarrow$^{161}Tb both yield ^{161}Tb but also produce the undesirable contaminant Tb-160, which has a half-life of 72.3 days. This contamination limits the exploitation of cyclotron-based production when high radionuclidic purity is required for medical applications (Nigron et al. [2023]).

REMIX Project

The experimental work presented in this thesis was primarily funded by the INFN CSN5 through the REMIX project (Research on Emerging Medical Radionuclides from Cross-Sections). This three-year initiative (2021-2023) aimed to identify the most efficient methods for producing various radionuclides, such as ^{47}Sc and ^{149,152,155,161}Tb, via nuclear reactions induced by different light ions (p, d, α) on various targets (Pupillo et al. [2023]).

The project was divided into seven distinct work packages, each focusing on specific aspects such as target production, cross-section measurements, nuclear simulations, radiochemistry, and technological advancements.

Concluding in 2023, the REMIX project successfully achieved all milestones, including the ones relevant to this thesis. The proposed nuclear reactions included: ^{nat}Dy(p,x), ^{nat}Dy(d,x), ^{nat}Eu(α,x), and ^{159}Tb(p,x). In addition to these, I also explored the ^{nat}Gd(α,x) reaction. The primary goals were to study cross-sections not previously explored in the literature (e.g., ^{nat}Eu(α,x)), to better characterize indirect processes, and to investigate discrepancies found in previous studies. A detailed discussion of the experiments and results is provided in Chapters 4 and 5.

APHRODITE-155 Project

Building on the results obtained from this thesis and the REMIX project, a new initiative, the APHRODITE-155 project, has been proposed. This project, part of the PRIN PNRR 2022 call, is funded under the EU's NextGenerationEU program – Mission 4, Component 2, Investment 1.1. The focus of APHRODITE-155 is the production of ^{155}Tb through both the direct route, ^{155}Gd(p,n)^{155}Tb, and the indirect route, ^{159}Tb(p,5n)^{155}Dy $\rightarrow$ ^{155}Tb.

The outcomes of this project will contribute to the development of an optimized protocol for the production and separation of pure ^{155}Tb. Due to the limited duration of the project (two years), large-scale production or application of this radionuclide for pre-clinical purposes is not currently planned. Initial steps in radiochemistry have been taken and are discussed in Chapter 6.

CHAPTER 2

Theoretical background

In this chapter, a set of theoretical tools will be described. Radioactivity, whose discovery has been discussed in Chapter 1, will be mathematically and physically described. The interaction of radiation with matter will be discussed for photons and heavy charged particles (hadrons). A summary of useful information about nuclear reactions will be provided. The equations used to determine the cross-section of a nuclear reaction will be presented.

2.1 Radioactive Decay

Radioactivity is a spontaneous process that occurs within unstable nuclei, leading to the emission of particles or electromagnetic radiation in an attempt to achieve a more stable nuclear configuration. Since the discovery of artificial radioactivity, over 3300 nuclei have been experimentally characterized, of which only 251 are stable. All other nuclei undergo the process of radioactive decay and for this reason we refer to them as *radionuclides* (RNs). These different nuclei can be organized in the so-called Nuclide Chart or Segrè Chart (see Figure 2.1, taken from NNDC [2023]), where the vertical axis represents the atomic number, Z, and the horizontal axis represents the number of neutrons, N. The pair (N, Z) identifies a specific nuclide, whether radioactive or not. Typically, the mass number, A = N + Z, is used, denoted as ${}^{A}_{Z}X$, where sometimes the atomic number is omitted since it can be unequivocally determined by the chemical element X. On the nuclide chart, nuclei with the same Z are called isotopes (e.g., ${}^{12}C$, ${}^{13}C$, and ${}^{14}C$ are different isotopes of carbon), if radioactive, they are called *radioisotopes*.

Different modalities of radioactive decay are possible. Some, like α decay, β decay or spontaneous fission are more common, others (double β^- emission, delayed proton/neutron emission, two proton decay or clusters emission) are referred as rare or exotic decay modes. The main modalities of radioactive decay useful for this thesis are described later in this section. In all these nuclear process a number of physical quantities are always conserved, namely, total energy (mass and kinetic), momentum, total charge and mass number (A). In particular, radioactive decay is an exoergic process, where the excess energy arising from the difference in mass between the parent and daughter nuclei is converted into kinetic energy of the products. We can write the mass conservation law in the center of mass of the system as:

$$E_1 = E_2 \implies m_p c^2 = m_d c^2 + m_x c^2 + K_d + K_x. \tag{2.1}$$

Here, m_p, m_d, and m_x represent the rest masses of the parent nucleus, daughter nucleus, and other products respectively, while K_d and K_x denote the kinetic energies of the daughter nucleus and other products, while c is the speed of light. Here masses

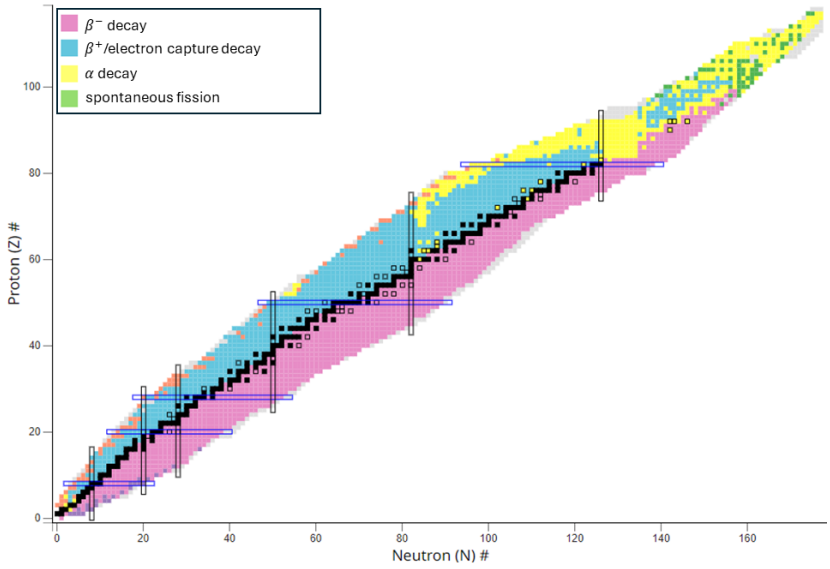

Figure 2.1: Nuclide Chart, or Segrè Chart. The x-axis represents the atomic number, while the y-axis represents the number of neutrons. In this representation, colors indicate the decay mode as reported in the legend (image taken from NNDC [2023].

are expressed in kg, however using the Einstein mass-energy equivalence law, we can express it in Joule, or more commonly in electronVolt (eV) and its multiple (rounded conversion factors: 1 eV = $1.602 \cdot 10^{-19}$ J = $1.783 \cdot 10^{-36}$ kg·c^2) The Q-value of the process, representing the energy released, can be determined as:

$$Q = m_p c^2 - m_d c^2 - m_x c^2 = K_d + K_x > 0, \tag{2.2}$$

which must be positive for the process to occur (necessary but nor sufficient condition).

2.1.1 Kinetics of Radioactive Decay

From a large number of experimental observations, it has been noted that the number of decays, dN_{dec}, in a "short enough" time interval, dt, is proportional to the number N of nuclei of the radionuclide present in the sample and to the time interval. Since $dN_{\text{dec}} = -dN$, as the number of nuclei decreases after decay, we can write:

$$dN = -\lambda \cdot N \cdot dt \tag{2.3}$$

where λ [s^{-1}] is the *decay constant* of the radionuclide. Solving for N, we find the so-called equation of radioactive decay:

$$N(t) = N_0 \cdot e^{-\lambda t} \tag{2.4}$$

where N_0 is the number of nuclei at time $t = 0$. If we rewrite Equation 2.3 as:

$$-\frac{dN}{N} = \lambda \cdot dt = dP(t) \tag{2.5}$$

we could give λdt the statistical meaning of the probability *dP(t)* of occurrence of radioactive decay for a single nucleus in the time *dt*. It follows that the decay constant λ represents the probability of decay per unit of time. This quantity, with very few exceptions[1], is not influenced by physical or chemical properties of the medium.

If more than one decay mode is possible for a certain nuclear species, the decay probability is given by the sum of the probability of occurrence of each process:

$$\lambda dt = \left(\sum_i \lambda_i \right) dt \tag{2.6}$$

Using Equation 2.4, it is possible to define the *half-life* of a radionuclide, namely the time after which the number of nuclei is halved:

$$\frac{N_0}{2} = N_0 \cdot e^{-\lambda t_{1/2}} \implies t_{1/2} = \frac{\ln 2}{\lambda} \tag{2.7}$$

We can also determine the *mean-life* τ of a radioactive species, calculated as the ratio between the sum of the lifetimes of the N_0 nuclei and N_0 itself. The former can be simply determined: considering that $N(t)\lambda dt$ is the number of nuclei that decay in the $[t, t+dt]$ time range, it follows that $t \cdot N(t)\lambda dt$ is the sum of their lifetime. Integrating over t, we obtain the required quantity. Thus:

$$\tau = \frac{\sum_{i=0}^{N_0} T_i}{N_0} = \frac{1}{N_0} \int_0^\infty t \cdot N(t)\lambda dt = \int_0^\infty t \cdot e^{-\lambda t} \lambda dt = \frac{1}{\lambda} \tag{2.8}$$

The *activity A(t)* of a radioactive substance is defined as the product between the decay constant and the number of nuclei of that specie at the time t:

$$A(t) = \lambda N(t) \tag{2.9}$$

The activity is equal to the *disintegration rate* only when the Kinetics of the decay is described by the Equation 2.4:

$$-\frac{dN(t)}{dt} = -\frac{d}{dt}\left(N_0 e^{-\lambda t}\right) = \lambda N(t) = A(t) \tag{2.10}$$

and it is not true for decay chains that will be discussed in Section 2.1.2.

2.1.2 Decay chains

After a radioactive decay the produced nucleus can be stable or unstable, in the latter case a decay chain is formed. The general case is:

$$N_1 \overset{\lambda_1}{\to} N_2 \overset{\lambda_2}{\to} N_3 \overset{\lambda_3}{\to} \ldots \overset{\lambda_{n-1}}{\to} N_n. \tag{2.11}$$

[1]The greatest exception of this rule is represented by the decay via electron capture (See Section 2.1.3). In this case the decay probability depends on the electron density in the surrounding of the nucleus. Factors that can vary the number and the distribution of electrons are the chemical bonds (electronegativity) and the pressure. In general, the relative difference of half-life is less than 1 %. See Kratz and Heinrich [2013] for further details.

In this case the decay equations can be written as:

$$\begin{cases} \dfrac{dN_1(t)}{dt} = -\lambda_1 N_1(t) \\ \qquad\vdots \\ \dfrac{dN_i(t)}{dt} = -\lambda_i N_i(t) + \lambda_{i-1} N_{i-1}(t) \\ \qquad\vdots \\ \dfrac{dN_n(t)}{dt} = \lambda_{n-1} N_{n-1}(t) \end{cases} \tag{2.12}$$

We refer to Equations 2.12 as Bateman Equations after Harry Bateman who first presented the general solution of such equations in 1910 (Bateman [1910]) The solution of a set of differential equations always depends on the boundary conditions.

Case 1: $N_i(0) = 0, \ \forall i \neq 1$**.** In this case the general solution is given by:

$$N_i(t) = N_1(0) \cdot \left(\prod_{j=1}^{i-1} \lambda_j \right) \cdot \sum_{j=1}^{i} \frac{e^{-\lambda_j t}}{\prod_{k=1,k\neq j}^{i} (\lambda_k - \lambda_j)} \tag{2.13}$$

Case 2: $N_i(0) \neq 0$**.** This is a more general case in which terms of production may be included:

$$\begin{cases} N_1(t) = N_1(0) \cdot e^{-\lambda_1 t} \\ \\ N_i(t) = \sum_{l=1}^{i-1} \left[N_l(0) \cdot \left(\prod_{j=1}^{i-k} \lambda_j \right) \cdot \sum_{j=k}^{i} \dfrac{e^{-\lambda_j t}}{\prod_{k=l;j\neq i} (\lambda_k - \lambda_j)} \right] + N_i(0) \cdot e^{-\lambda_i t} \end{cases} \tag{2.14}$$

2.1.3 β decay

The expression β decay includes three modes of radioactive decay namely, β^-, β^+ and Electron Capture (EC). A complete theory for this process was developed by Enrico Fermi in 1934, by expanding the ideas of Wolgang Pauli about the existence of neutrino (Jensen et al. [2000]).

Two of the common features of all these processes are the variation of one unit in the atomic number ($Z_d = Z_p \pm 1$) and the fact that the mass number A remains constant (isobaric transitions). The core modification that occurs in the nucleus is the transformation of one neutron in a proton or vice versa. Being the Q-value of the process positive, the mass of the daughter nuclide is always lower than the one of the parent as it can be seen in Figure 2.2. If the mass number is odd there is one only stable isotope per mass number at the very bottom of the stability parabola that describe the mass as a function of Z. This is not true anymore for even mass number where two stability parabola can be found, as in the example in Figure 2.3. This happens because the (odd, odd) combination of (N,Z) shows a lower binding energy with respect to the (even, even) combination leading to a lower mass for the latter. Is it possible that an even-even nucleus that is not at the very bottom of the stability curve finds itself at an energy lower than the neighbouring odd-odd nucleus and for this reason it is stable for beta decay as it happens for ^{154}Sm,

as a consequences ^{154}Eu has two energetically possible decay routes: β^+/EC ($I_{\beta^+/EC}$ = 0.018 %) or β^- (I_{β^-} = 99.982 %). Note that alpha decay or more exotic processes are still possible as for ^{154}Dy. Odd-odd stable nuclei are very rare, ^{2}H, ^{6}Li, ^{10}B and ^{14}N.

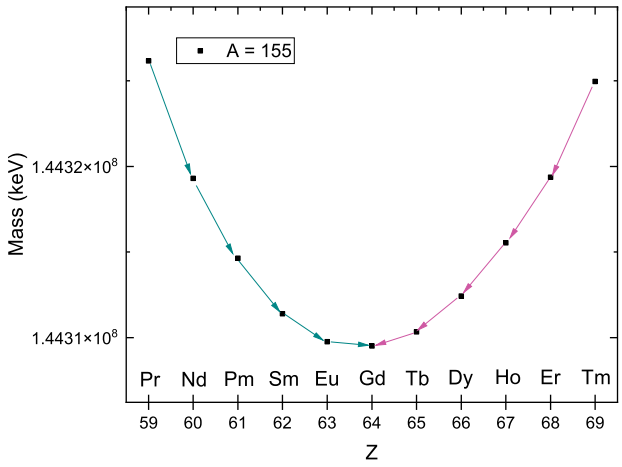

Figure 2.2: Mass dependence on atomic number for odd mass number nuclei. In this particular example the mass number A = 155 is displayed. It can be seen that nuclei have the tendency to decay to the nucleus of minimum mass on an isobaric curve through β^+/EC (pink arrows) or β^- (blue arrows). Data taken from NNDC [2023].

β^- decay

This process addresses an instability due to an excess of neutrons (neutron-rich nuclei). It can be summarized by the following scheme:

$$^{A}_{Z}X \rightarrow ^{A}_{Z+1}X + \beta^- + \bar{\nu}_e \tag{2.15}$$

The β^- particle is identical to the electron but it has nuclear origin, while $\bar{\nu}_e$ is the electron antineutrino. In this process a neutron is transformed in a proton. Actually the neutron itself, when not bonded, decays β^- with a decay time of 10 minutes ($n \rightarrow p + \beta^- + \bar{\nu}_e$) [NNDC [2023]]. Being a 3 particle process the excess of kinetic energy of the products is not fixed. The daughter nucleus is much heavier than the other particles and brings away only a negligible part of the available energy, the remaining part is shared between the β^- particle and the antineutrino on a statistical base. For this reason the energy of the β^- is usually reported as $E^{max}_{\beta^-}$. This also distinguishes β^- from electrons produced with different process that generally have a fixed energy (e.g. conversion electrons, photo-electrons etc.). Typical maximum energy values is of the order of 1 MeV, but ranges from few keV to tens of MeV.

β^- is rarely a transition between the ground states of two nuclei and generally involves one or more excited levels of the daughter nucleus. In fact, the stability curves reported in Figures 2.2-2.3 are more complex than how they appears. Each arrow is, actually, a set of possible decays from the parent nucleus to one of the excited states of the

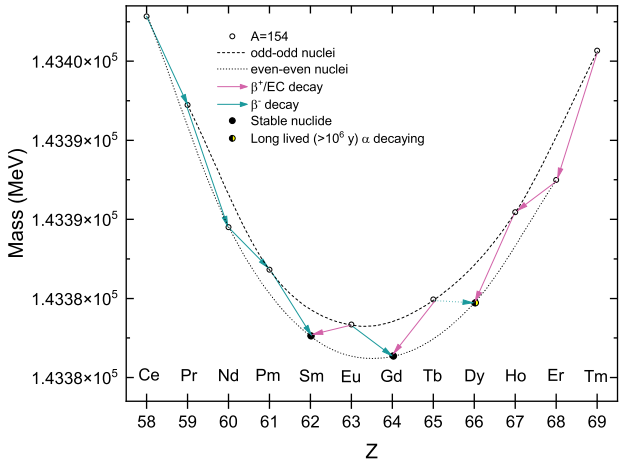

Figure 2.3: Mass dependence on atomic number for even mass number nuclei. In this particular example the mass number A = 154 is displayed. Two stability curves can be drawn, one for odd-odd nuclei (dashed line) one for even-even nuclei (dotted line). Double decay modalities, β^+/EC (pink arrows) or β^- (blue arrows), are possible for odd-odd nuclei when it is in the middle between two even-even nuclei with lower mass (e.g. ^{154}Eu). The β^- for ^{154}Tb is energetically possible but no record of that are present in literature. Data taken from NNDC [2023].

daughter nucleus. Pure β^- emitters exist but their number is limited (e.g. ^{3}H, ^{14}C, ^{90}Sr, ^{99}Tc etc.). De-excitation processes are described later on in this chapter.

A large number of β^- decaying radionuclides find application in nuclear medicine, especially in therapy, such as ^{131}I ($T_{1/2}$ = 8.02 d, $E^{max}_{\beta^-}$ = 607 keV), ^{188}Re ($T_{1/2}$ = 17.0 h, $E^{max}_{\beta^-}$ = 2150 keV) or ^{177}Lu ($T_{1/2}$ = 6.64 d, $E^{max}_{\beta^-}$ = 498 keV). A list of the most common radionuclides used in therapy can be found in Yeong et al. [2014]. As discussed in Chapter 2, ^{161}Tb ($T_{1/2}$ = 6.89 d, $E^{max}_{\beta^-}$ = 522 keV), is the only β^- emitter of the terbium quadruplet.

β^+ Decay

Above the stability valley in the Nuclide Chart, a neutron-deficient region can be found. In β^+ decay, a proton is transformed into a neutron to increase the binding energy and decrease the mass along the stability curve (Figures 2.2-2.3). It's important to note that the proton itself does not decay. The general process of β^+ decay can be described as follows:

$$ {}^{A}_{Z}X \rightarrow {}^{A}_{Z-1}X + \beta^+ + \nu_e \tag{2.16} $$

Here, β^+ represents the positron, the antiparticle of the electron, which has the same mass but opposite charge, while ν_e denotes the electron neutrino.

It must be noted that, from an energetic point of view, β^+ decay is possible only if the mass difference between the two atoms involved is at least $2m_ec^2$ = 1.022 MeV.

An important distinction between the energy spectra of β^+ and β^- emissions can be highlighted: both show a lower emission at low energy, reach a maximum around

$\bar{E}\beta = \frac{1}{3}E\beta^{max}$, and then decrease until they reach the maximum possible energy for the decay. However, the low-energy part of the distribution of emitted β^- particles is enhanced due to Coulomb interaction with the positively charged nuclei (see Figure 2.4); for positrons, the behavior is opposite.

β^+ decay is particularly important in nuclear medicine, especially in diagnostics for PET studies as described in Chapter 1. A number of positron emitters have been studied and are currently used in routine medicine, and many more are subjects of studies at different stages of the process for human application. ^{149}Tb, ^{152}Tb, and ^{155}Tb isotopes of terbium are promising β^+ emitters and are the subject of this thesis as well.

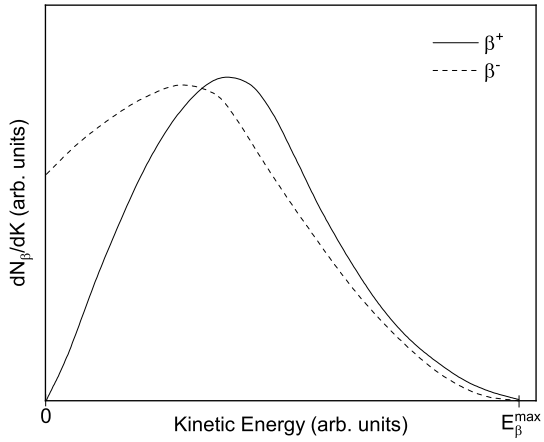

Figure 2.4: Energy distribution for β^+ (dashed line) and β^- (solid line) particles after β decay. The number of β^- emissions at low energy is increased due to the deceleration caused by Coulomb interaction with the nucleus.

Positrons, being made of antimatter, have a short life in ordinary matter: after being slowed down to quasi-zero energy due to Coulomb interaction, they may form a special species with electrons, namely positronium, and then annihilation occurs. The mass energy of the electron-positron pair is converted into two photons with energy equal to the electron's rest mass, i.e., 510.999 keV. Generally, we refer to these photons as annihilation photons at 511 keV. To conserve the total momentum, the emission occurs with an angle of π between the two photons. However, slight deviations from this angle and energy are possible due to the fact that neither the electron nor the positron is completely at rest at the moment of annihilation. This is reflected in the fact that the peak in the gamma spectra related to these photons is generally broader than expected (Doppler effect occurs due to a non-at-rest source). More details about γ-ray spectrometry will be given in Chapter 4.

Electron capture (EC) decay

As pointed out in the previous paragraph, β^+ decay occurs only if the mass difference between the parent and daughter atoms is higher than $2m_ec^2$. For nuclides close to the stability-valley this energy is not always available. These nuclei can capture an electron

from one of the atomic shells and use it to convert the proton in neutron according to the elementary process that follows:

$$ {}^{A}_{Z}X + e^{-} \rightarrow {}^{A}_{Z-1}X + \nu_e \tag{2.17} $$

This process occurs with the energetic condition that the mass of the parent atom is higher than the mass of the daughter atom, so it constitute an alternative to β^+ also when both are possible. In fact, many neutron-deficient nuclei decay both for β^+ and EC (e.g. ^{22}Na decays β^+ (90.3 %) and EC (9.7 %) with $T_{1/2}$ = 2.6 y).

The electron is generally captured form the K shell, being the closest to the nucleus, while the superposition between the wavelength functions of the outer shells electrons with the nucleus is lower and consequently the probability of electron capture from L, M etc. shells is lower.

A vacancy in an inner shells induces instability in the atom whose electrons will be rearranged with consequent release of energy in the form of *characteristic X-rays*. The energy of these photons is fixed and equal to the energy difference between the two levels involved in the transitions.

The atomic de-excitation can also occur by emission of atomic electrons. This process is named *Auger effect*, and the arising electrons are called Auger electrons. These electrons are easily distinguishable form β^- since they are mono-energetic and generally have low energy (few eV) being emitted form outer shells.

In general, the higher Z, the lower is the probability of Auger electrons with respect to X-rays emission.

Auger emitters are important in nuclear medicine with the Auger therapy that exploits the high LET of the low energy Auger electrons to effectively damage tumor cells, while sparing healthy tissues singe the short range of these electrons limit the dose deposit to few micrometers from the decaying nucleus (Buchegger et al. [2006]). Between the radionuclides that are object of this thesis, ^{161}Tb is also an Auger emitters: it emits about 2.24 e^-/decay with a LET of 4-26 keV/μm and a range lower than 1 μm in soft tissues (NNDC [2023])

2.1.4 α decay

A complete theory of the α decay was formulated by George Gamow in 1929 even if this process was the first one to be discovered and studied at the end on the 1890s. The most famous example of α emitter is ^{226}Ra discovered by Marie Skłodowska Curie and his husband Pierre Curie in 1898.

α particles are particles equivalent to $^4He^{2+}$ (2 protons and 2 neutrons) and its emission is the most common decay process for nuclei with $Z > 83$. The process is described by the following equation:

$$ {}^{A}_{Z}X \rightarrow {}^{A-4}_{Z-2}X + \alpha \tag{2.18} $$

In this case the energy excess is divided between only 2 products, so the $alpha$ particle is mono-energetic. The energy of the α particles ranges from 4-9 MeV, while the decay times of α emitting radionuclides varies from 10^{-17} s to 10^{10} y.

Another difference with respect to β decay is that, in the low Z range, the transitions take places directly to the ground state without need for successive de-excitation, with heavier nuclei the involvement of excited states is more likely to occur.

The Gamow's theory of the α decay foresees that there is a certain probability of pre-formation of the α particle within the nucleus but to be emitted it is necessary to overcome a potential barrier due to Coulomb interaction between the two particles and

increased by a factor due to the angular momentum of the alpha particles. Classically it is impossible to overcome this barrier but the quantum tunneling effect introduces a non zero probability of emission of the α particle from the nucleus. The higher the energy the higher the probability of tunneling and the shorter the decay time. The latter statement can be resumed in the empirical law of Geiger-Nuttal that relates the decay time to the energy of the α particle:

$$\log \tau \simeq \frac{A(Z)}{\sqrt{E}} + B(Z) \tag{2.19}$$

This empirical law can be derived from the more complete Gamow's theory whose detailed description may be found in Bertulani [2007].

Targeted Alpha Therapy (TAT) shows great potential in cancer treatment because alpha particles deliver high LET damage to cancer cells while sparing healthy tissue. Their unique properties result in severe DNA damage, particularly difficult for cancer cells to repair, leading to cell death. The α emitters RN for TAT already in use are ^{225}Ac ($T_{1/2}$ = 10 d, E_α = 5.83 MeV), ^{211}At ($T_{1/2}$ = 7,2 h, E_α = 5.87 MeV and 7.45 MeV [2]) and ^{223}Ra ($T_{1/2}$ = 11.4 d, E_α = 5.71 MeV) (See Sollini et al. [2020], Nelson et al. [2021]). In the framework of this thesis the most interesting "in development" radionuclide in this category is ^{149}Tb ($T_{1/2}$ = 4.1 h, E_α = 3.97 MeV) (See Müller et al. [2014b]).

2.1.5 Nuclear de-excitation pathways: γ-ray emission and internal conversion (IC)

Strictly speaking, γ-ray emission is not properly a nuclear decay since no variation of number or type of nucleons occurs in the nucleus. It is, more precisely, a de-excitation process that excited nuclei, formed after a nuclear reaction or a decay, use to loose the excess of energy. Moreover γ-ray emission is not the only process that nuclei can exploit to de-excite: the internal conversion (IC) and the more rare pair production are possible. As the latter is very rare, it will not be discussed here in detail.

γ-ray emission

A quantum system composed of A nucleons forming a nucleus has numerous possible excited states above its ground state. These states can be accessed if sufficient energy is provided to the system. Transitions among these states predominantly occur via emission of γ radiation, which spans the high-energy region of the electromagnetic spectrum, ranging from 50 keV to 10 MeV.

In most radioactive decays, the daughter nucleus is initially in an excited state. However, de-excitation typically occurs almost instantaneously (within 10^{-12} seconds), making it seem as though the emitted γ-rays originate from the parent nucleus. This simplification is somewhat justified because, although γ-rays result from transitions between the nuclear states of the daughter nucleus, their intensities depend on the parent nucleus. For instance, ^{48}Ti (stable) can result from the decay of ^{48}V (via electron capture or β^+ decay, with a half-life of 15.974 days) or ^{48}Sc (via β^- decay, with a half-life of 43.71 hours). In the former case, the emission at 1312.105 keV has an intensity of 98.2 %, whereas, in the latter, the intensity is 100 %.

In some decays, the daughter nucleus does not de-excite immediately but does so after a delay ranging from a few nanoseconds to several hours or longer. Such long-

[2] The α emitter ^{211}At decays in ^{207}Bi emitting an α particle of E_α = 5.87 MeV with a branching ratio of 41.8 % and decays by EC in ^{211}Po with a branching ratio of 58.2 %. The latter decays with a short half-life ($T_{1/2}$ = 0.5 s) to ^{207}Pb emitting an α particle of E_α = 7.45 MeV. In total a single α per decay of ^{211}At is emitted.

lived excited states are termed *metastable states*, and the transitions are known as *isomeric transitions*.

Even though the energy of photons associated with specific transitions can be determined with high precision, it is important to note that the energy of a given state is not infinitely precise. According to the Heisenberg uncertainty principle:

$$\delta E \times \delta t \geq \frac{h}{2\pi} \ (= 6.582 \times 10^{-16} \text{ eV} \cdot \text{s}), \tag{2.20}$$

where δE is the uncertainty in energy and δt is the uncertainty in time, assumed to be the state's lifetime $\tau = 1/\lambda$. Despite this, even for very short-lived states, the energy uncertainty does not exceed 1 meV, which is at least seven orders of magnitude lower than the transition energy itself.

The process may be represented as follows

$$^{A}_{Z}X^{*} \rightarrow ^{A}_{Z}X + \gamma \tag{2.21}$$

where $^{A}_{Z}X^{*}$ stands for an excited state. The decay energy Q is divided between the energy of the photon E_γ and the kinetic energy E_D^K of the nucleus that recoils:

$$Q = E_\gamma + E_D^K \tag{2.22}$$

By applying the conservation of the momentum $p_\gamma = p_D$ it is possible to obtain that

$$E_D^K = \frac{E_\gamma^2}{2M_D c^2} \tag{2.23}$$

where M_D is the mass of the daughter nucleus. The recoil energy is usually less than 0.1 % of the γ-ray energy being negligible in the practice.

Internal Conversion

The process of internal conversion (IC) is a common nuclear de-excitation mechanism where excess energy from the nucleus is transferred to an atomic electron, causing its ejection from the atom. This ejected electron, known as an *IC electron*, is mono-energetic with an energy equal to the difference between the nuclear transition energy and the binding energy of the electron, which depends on the electron's originating shell. IC is often followed by the emission of characteristic X-rays and Auger electrons.

Internal conversion competes with γ-ray emission. Generally, the probability of IC increases with the atomic number Z and decreases with the transition energy. Consequently, in high-Z nuclei, isomeric transitions with small ΔE may be entirely converted to IC electrons.

2.2 Interaction of radiation with matter

Radiation interact with matter in a number of ways depending on the radiation nature, its energy and the properties of the medium. Fast neutrons in water will behave much differently from protons in lead. To provide a full description of the interaction of radiation with matter usually a classification on the radiation type is performed as summarized in Figure 2.5. The main classification concerns the division between ionizing and

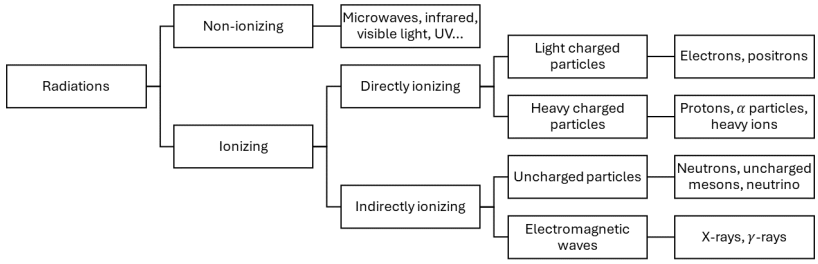

Figure 2.5: Classification of radiations, with particular focus on ionizing radiations.

non-ionizing radiation. The former has enough energy to ionize[3] the matter directly or indirectly.

Directly ionizing radiation consists of charged particles with mass that interact with matter through the Coulomb force, causing ionization directly by transferring sufficient kinetic energy to atomic electrons. These particles include electrons, muons, charged pions, protons, and energetic charged nuclei. In contrast, indirectly ionizing radiation is electrically neutral and does not interact strongly with matter. Instead, its ionization effects primarily result from secondary interactions within the material. These differences vary the mechanisms through which these types of radiation produce ionization in matter. Among the ionizing radiations, in this section the interactions of heavy charged particles and of photons will be described, being important for the understanding of the beam energy losses within our targets and for the γ-ray spectrometry, an experimental technique that will be described in Chapter 4.

2.2.1 Heavy Charged Particle Interaction

Heavy charged particles, like protons, deuterons, and α particles, principally interact with the orbital electrons of atoms in the medium via the Coulomb force. While interactions with nuclei are possible but rare, they don't significantly contribute to energy losses. Within the medium, these charged particles interact with a broad range of electrons, leading to a continuous decrease in particle energy until they come to a halt. Locally, this interaction results in either electron excitation to higher energy levels or atom ionization by electron removal. The maximum energy transferred to an electron per interaction is given by:

$$\Delta E^{max} = \frac{4m_e M}{(m_e + M)^2} E \simeq \frac{4m_e}{M} E \tag{2.24}$$

where m_e and M denote the electron and particle masses respectively, and E represents the particle's energy. For protons, this corresponds to roughly $1/500$ of the particle's energy.

A systematic categorization of interactions, summarized in Figure 2.6, consists of the three groups based on the impact parameter b, defined as the distance between the particle's trajectory and the classical radius a of the atoms in the absorber [Podgorsak [2016]]:

[3]The ionization energy of the most common materials ranges between $\sim$4 eV for alkali elements to 24.6 eV for Helium.

- **Radiation collision** $b \ll a$: Interaction occurs between the charged particle and the nucleus's electric field, unshielded by electronic shells. This can result in elastic or inelastic scattering, accompanied by a significant energy loss and possibly emission of bremsstrahlung photons. This interaction's probability is proportional to $1/M$, thus significant for light particles like electrons and positrons but negligible for heavier charged particles.

- **Hard collision** $b \sim a$: Direct interaction between the particle and electrons leads to substantial energy transfer (up to ΔE^{max}). This interaction, also termed close collision, can ionize other atoms via the departing electron, known as a δ-ray. Though statistically infrequent, these collisions lead to significant energy losses, with about half of the particle's kinetic energy dissipated through this process.

- **Soft collision** $b \gg a$: Here, the particle interacts with entire atoms, resulting in minimal energy transfer to electrons, causing polarization, excitation, or valence electron removal with low kinetic energy post-ionization. However, the large number of distant collisions compensates for the low energy transfer, leading to approximately 50 % of the particle's energy loss.

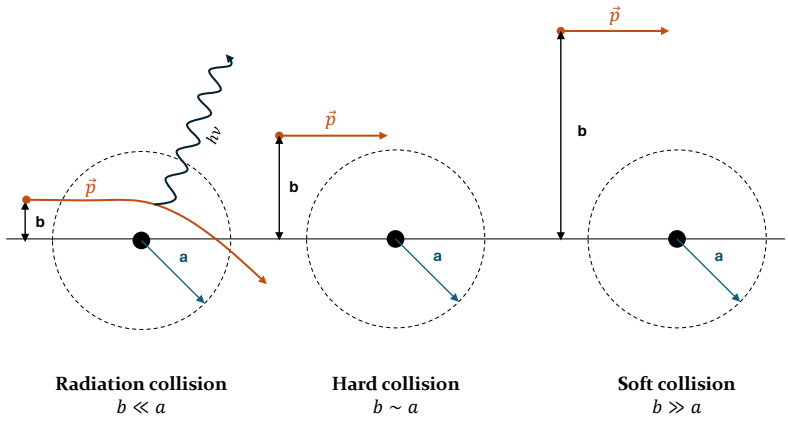

Figure 2.6: Classifications of charged particle interactions with matter based on the impact parameter b compared to the classical radius of the atom a. The interactions can be categorized in: radiative collision ($b \ll a$), hard collision ($b \sim a$) and soft collision ($b \gg a$). In the Figure, $\vec{p}$ is the linear momentum of the incident particle and $h\nu$ represent the photons emitted in the case of radiative collision.

When describing the behavior of a particle beam in a medium a fundamental parameter to account for is the *linear stopping power*, -dE/dx, that describes the energy loss per unit of path length [MeV·cm^{-1}]. A even more used quantity is the *mass stopping power*, S, that is obtained by dividing the linear stopping power by the density of the medium ρ, and it is usually given in units of MeV·cm^2·g^{-1}. All the processes above described contribute to the loss of energy:

$$S = -\frac{1}{\rho}\frac{dE}{dx} = S_{\text{rad}} + S_{\text{col}}^{\text{hard}} + S_{\text{col}}^{\text{soft}} \tag{2.25}$$

where S_{rad} is known as nuclear stopping power, while $S_{col} = S_{col}^{hard} + S_{col}^{soft}$ is referred as electronic stopping power. As previously stated for heavy charged particles $S_{rad} \ll S_{col}$ and for this reason it is usually neglected.

Two different theory were developed to describe the collision interaction of charged particles with matter. One developed by Bohr in 1913 based on classical physics assumptions (Bohr [1913]), and another proposed by Bethe in 1931 exploiting the newborn theories of quantum mechanics and special relativity (Bethe [1932]). Both theorie are based on four fundamental assumptions:

1. The charged particle moves much faster than the orbital electrons so that the interaction is rapid
2. The mass of the charged particle is much higher than the electron mass.
3. Only electromagnetic forces are considered, nuclear reactions are neglected.
4. Only interactions with the atomic electrons are considered, the radiation collisions are neglected.

Successive correction where added to explain theoretical deviations from the experimental data, generally caused by the not-compliance of one or more the initial assumptions of the models with the reality (Salvat [2022]).

All these models, however, may be summarized by a single equation:

$$S_{col} = 4\pi N_A r_e^2 m_e c^2 \frac{z^2}{\beta^2} \frac{Z}{A} B_{col} \tag{2.26}$$

where N_A is the Avogadro number, r_e = 2.818 fm is the classical electron radius, z is the particle charge, Z and A are the atomic and mass numbers of the medium, β = v/c where v is the velocity of the particle and c is the speed of light in the vacuum. B_{col} is the atomic stopping number that is function of β, Z and the mean ionization/excitation energy[4] I. The value of B_{col} depends on the theory used:

- Classical Bohr equation:

$$B_{col} = \frac{1}{2} \ln \frac{2m_e c^2 \beta^2}{I} \tag{2.27}$$

- Relativistic, quantum-mechanical Bethe equation:

$$B_{col} = \ln \frac{2m_e c^2 \beta^2}{I(1-\beta^2)} - \beta^2 \tag{2.28}$$

- Relativistic, quantum-mechanical with shell correction (C/Z) and density effect (δ) correction Bethe-Bloch equation:

$$B_{col} = \ln \frac{2m_e c^2 \beta^2}{I(1-\beta^2)} - \beta^2 - \frac{C(\beta)}{Z} - \delta(\beta) \tag{2.29}$$

More complex but accurate expressions for B_{col} have been reviewed in Salvat [2022]. We limit our discussion to the two correction presented in Equation 2.29:

[4] I is the minimum energy that can be transferred to the electron. Empirical relations are available to describe the dependence of I from Z. The most general is $I = 9.1Z(1 + 1.9Z^{-2/3})$. Here I is expressed in eV. The experimental values can be found in the ICRU report 37 (Brice [1985]).

- **Shell Corrections**: At lower energies, the assumption of slow-moving electrons no longer holds, leading to an overestimation of the average ionization or excitation energy, which consequently underestimates the stopping power. These corrections are contingent upon the electron's velocity, determined by its shell.
- **Density Effect Correction**: in the above mentioned theories the interaction between different atoms are neglected (gas hypothesis). A positively charged projectile attracts electrons and repels nuclei, causing polarization in the medium's atom, resulting in a shielding of the more distant electrons and a reduction of the number of soft collisions that decreases the stopping power. A correction that depends on the velocity of the particle, i.e. $\delta(\beta)$, is then added. This effect is particularly important at relativistic energies.

It is interesting to notice that at a fixed velocity β, the stopping power does not depend on the mass of the particle, but only on its charge and speed, other than the characteristic of the medium. Thus protons and deuterons have the same stopping power at the same velocity (but not at the same energy). A comparison between the stopping power of protons, deuterons and α particles in gadolinium medium is reported in Figure 2.7, here data are taken from NIST database (Berger et al. [2017]) and the energy range of interest for this thesis (5 - 70 MeV) is highlighted.

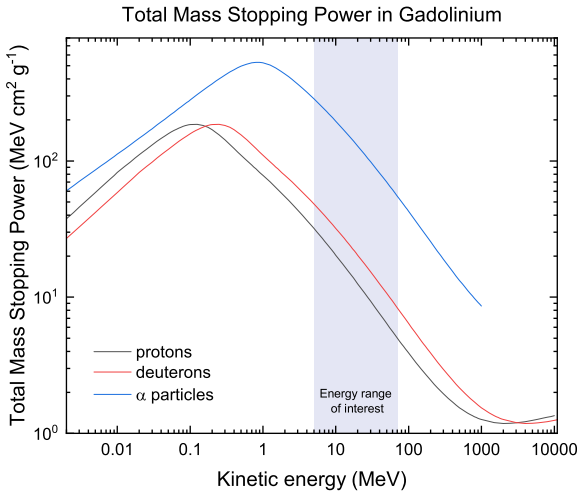

Figure 2.7: Mass stopping power of protons, deuterons and α particles in gadolinium medium as a function of the kinetic energy. The energy region of interest for this thesis is highlighted in light blue. Data are taken from NIST (Berger et al. [2017]). No data are available for alpha particle with kinetic energy higher than 1 GeV.

Definitions of range and straggling

From an experimental perspective, the range of a particle with a given energy in a certain material is the maximum thickness that the particle can penetrate. To measure it, one can incrementally increases the thickness of the absorber by adding layers until no particles are detected by the sensor positioned at the absorber's exit.

Theoretical determination of a particle's range in a given medium can be derived from its stopping power under the Continuous Slowing Down Approximation (CSDA), using the relation:

$$R(E) = \int_0^E \left(-\frac{dE'}{dx}\right)^{-1} dE'. \tag{2.30}$$

However, this quantity represents the path length of the particle, that can be different from the penetration length of the same particle in the medium. In fact, this relation is based on the assumption of a linear trajectory. It fails to account for the stochastic nature of particle interactions, where different particles in the beam experience varying numbers of collisions with electrons. Additionally, it overlooks the fact that trajectories are not perfectly straight due to possible elastic scattering with nuclei, which can deviate the particle from the linear path, resulting in a spread of penetration depths within the target, known as *range straggling*. While this effect is more pronounced for lighter particles such as electrons, even protons, deuterons and α particles exhibit straggling of a few percent, and it increase by deepening into the target due to the increasing of number of scattering interaction with the nuclei of the medium.

The average penetration depth of a particle beam in a medium is called *projected range* and it can be either measured as described above or simulated using Monte Carlo based radiation transport software. In Figure 2.8, a simulation conducted using SRIM software (Ziegler et al. [2010]) illustrates the trajectories of a 67.4 MeV alpha particle beam within a 3 mm thick aluminum absorber.

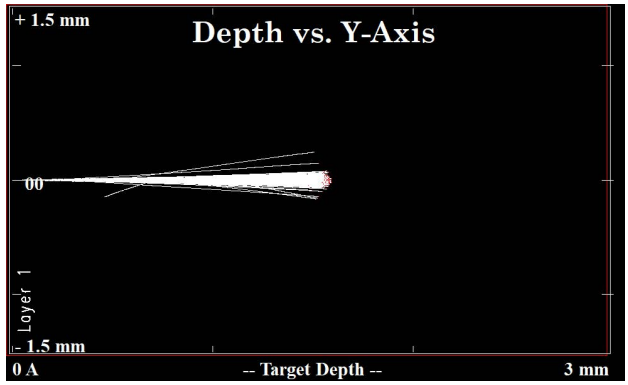

Figure 2.8: Simulation depicting the interaction of a 67.4 MeV α particle beam within a 3 mm thick aluminum target. Notably, deviations from the linear trajectory are observable. However, with few exceptions, the projected ranges closely align with the linear approximation.

From the same simulation, it is possible to extract information about the mean projected range and the extent of straggling, which are approximately 1.562 mm and 0.049 mm (2σ), respectively, constituting about 4 % of the total range (see Figure 2.9).

Energy losses in thin and thick absorbers

To describe the energy loss within a target, we can rely on the following equation:

$$\Delta E = \left(-\frac{dE}{dx}\right)\Big|_{avg} \Delta x \tag{2.31}$$

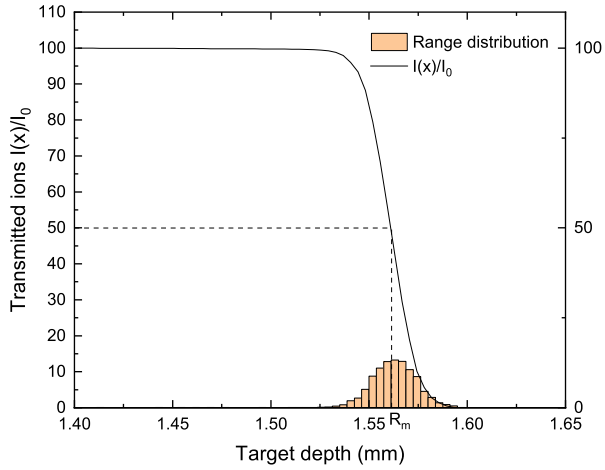

Figure 2.9: Projected range distribution of a 67.4 MeV α beam within a thick aluminum target (depicted by orange columns). The black line represents the ratio of transmitted ions (I/I_0) after a given depth within the target (x). The mean projected range is highlighted as R_m.

where Δx represents the target thickness, and $(-dE/dx)_{avg}$ denotes the average stopping power within the target.

Since the stopping power is highly nonlinear, determining the average can be challenging. However, for thin targets where the energy loss δE is much smaller than the initial energy E, the approximation holds:

$$\left(-\frac{dE}{dx}\right)\Big|_{E} \approx \left(-\frac{dE}{dx}\right)\Big|_{E-\delta E} \approx \left(-\frac{dE}{dx}\right)\Big|_{avg} \tag{2.32}$$

For thicker targets, a practical approach to calculate the energy lost by particles consists into making use of range-energy tables or graphs, such as those provided by the SRIM software (SRIM). This method is illustrated in Figure 2.10 and summarized here. Let R_0 be the range in the material for an incident particle with energy E_0. Subtracting the physical thickness of the target Δx yields R_1, which represents the range of particles emerging from the other side of the target. Determining the energy E_1 corresponding to range R_1 allows us to find the energy of the transmitted beam. The energy loss is then calculated as $\Delta E = E_0 - E_1$. This method remains valid as long as energy straggling is not excessive.

In the energy range pertinent to this thesis (5-70 MeV), an analytical expression that provides a good approximation for the relation between energy and range can be found:

$$R = a + b \cdot E^c \tag{2.33}$$

This expression is partly justified by considering that in an intermediate energy range (as highlighted in Figure 2.7), the dominant term in the stopping power equation is:

$$-\frac{dE}{dx} \propto \frac{z^2}{\beta^2} \ln \frac{2m_e c^2 \beta^2 \gamma^2}{I} \tag{2.34}$$

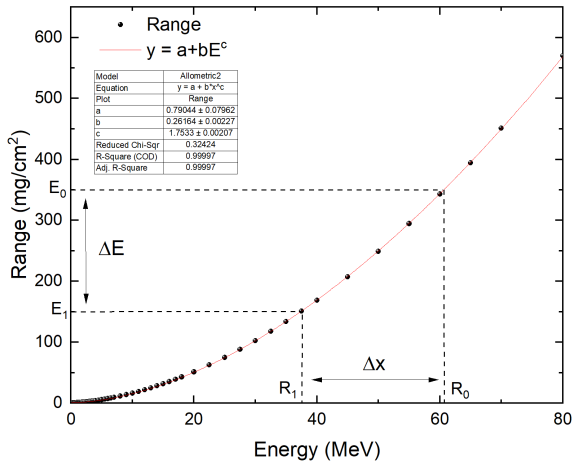

Figure 2.10: Representation of the range-energy method to determine te energy loss in a thick target. In this particular example the data for α particles in aluminum are reported. The Equation 2.33 fits the experimental data.

where only parameters dependent on the particle are considered. By appropriately multiplying by the ion mass $m_i \simeq A_i \cdot m_p$ both inside and outside the logarithm, we find:

$$-\frac{dE}{dx} \propto \frac{z^2}{E} \ln \frac{2m_e E\gamma^2}{I m_p A_i} \tag{2.35}$$

When the energy per nucleon $E/A_i < 100$, the logarithm doesn't change significantly, resulting in the stopping power being proportional to E^{-1}. Using Equation 2.31, we deduce that R is proportional to E^2. In reality, the power c in Equation 2.33 isn't exactly 2 but varies from 1.70 to 1.80 for the most common materials and incident particles.

2.2.2 Photons

In this section, we delve into the interactions of photons within the [20 - 2000 keV] energy range, crucial for understanding γ-ray spectrometry. This technique relies on detecting the energy of nuclear γ-rays and atomic X-rays, which predominantly fall within this energy range.

When photons penetrate an absorbing medium, they undergo various interactions, either with the nuclei (e.g., pair production) or with orbital electrons (e.g., Compton scattering or the photoelectric effect). Unlike charged particles, which lose energy gradually, a single interaction abruptly alters the photon's trajectory, either through absorption or scattering at significant angles, possibly with different energies.

A key quantity characterizing photon-medium interactions is the *linear attenuation coefficient*, μ, dependent on photon energy $E_\gamma = h\nu$, where ν is frequency and h is the Planck constant ($4.136 \cdot 10^{-18}$ keV·s).

Consider a collimated monoenergetic photon beam of intensity I_0 passing through a thin adsorber layer. The number of interactions, and hence beam attenuation (-dI), is

proportional to beam intensity and material thickness (dx), governed by μ:

$$-dI = I(x)\mu dx \implies I(x) = I_0 e^{-\mu x}. \tag{2.36}$$

Thus, the attenuation follows a decreasing exponential function. It's important to distinguish between attenuation and absorption: the former refers to beam intensity reduction, while the latter relates to energy deposited within the medium. Since not all interactions lead to complete absorption, the absorption curve typically lies below the attenuation curve.

Within a given path length (dx), different interaction processes have a non-zero probability of occurrence. Therefore, the total linear attenuation coefficient is the sum of coefficients for each possible interaction:

$$\mu = \sum_i \mu_i. \tag{2.37}$$

The attenuation coefficient also varies with medium properties. Another commonly used measure is the mass attenuation constant μ/ρ, independent of medium density and dependent only on atomic and mass numbers. The mass attenuation coefficient for a popular material in gamma-ray spectrometry, i.e. germanium, is reported in Figure 2.11 (data taken from NIST database [Hubbell and Seltzer [1995]]), where the contribute of the different process to the total attenuation are highlighted.

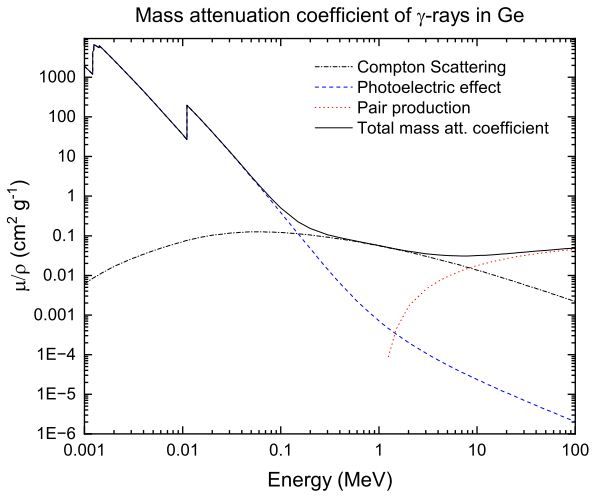

Figure 2.11: Mass attenuation coefficient in a germanium detector as a function of the energy of the photon. The contributes of the different processes are highlighted. Data are taken from NIST database [Hubbell and Seltzer [1995]].

Photoelectric effect

For photons with energy between the ionization energy for the material and E∼100 keV the dominant interaction is photoelectric effect, in which the photon is completely absorbed and an electron is ejected. The interaction happens between a photon and an

orbital electron which is still bound to the atom[5]. The complete reaction for the photoelectric effect is: $\gamma + A \longrightarrow A^+ + e^-$. The kinetic energy of the electron K_e is related to the energy of the photon E_γ through the relation:

$$K_e = E_\gamma - E_B \tag{2.38}$$

where E_B is the binding energy of the electron.

If the interaction of the photon occurs with an electron from an inner atomic shell (e.g. K-shell) the vacancy will be filled by electrons from higher shells and the transition energy will be emitted as characteristic X-rays or as an Auger electron as discussed in Section 2.1.3 for the EC decay.

The determination of the attenuation coefficient for this process is complex because it requires the complete atomic wavefunction to be written. However the relation with the energy of the photon and the properties of the material may be resumed as:

$$\frac{\mu_{ph}}{\rho} \propto \frac{Z^n}{E^{3.5}} \tag{2.39}$$

where n varies in the range between 4-5 depending on the photon energy (See Knoll [2010]). By plotting the photoelectric absorption coefficient (see Figure 2.11), one can observe discontinuities corresponding to the binding energies of various electron shells (K, L, M, etc.). When the incident photon energy exceeds the binding energy of a specific shell, the photoelectric effect involving electrons from that shell becomes possible. Just below this energy threshold, the interaction becomes abruptly impossible, causing a sudden drop in the mass attenuation coefficient.

Compton Effect

The Compton effect[6] is an inelastic scattering process between photons and electrons in a medium. It is the most common interaction process at the energies of γ-rays emitted after radioactive decay, as illustrated in Figure 2.11.

In this process, only part of the photon's energy, $h\nu$, is transferred to an electron, which then departs with momentum p_e at an angle ϕ relative to the incoming photon. Simultaneously, the photon is scattered at an angle θ with a reduced energy, $h\nu'$. The kinematics of the Compton effect is shown in Figure 2.12.

By applying the conservation of relativistic momentum, it is possible to determine the energy of the scattered photon as a function of the angle and the initial energy:

$$h\nu' = \frac{h\nu}{1 + \frac{h\nu}{m_e c^2}(1 - \cos\theta)}. \tag{2.40}$$

[5]A similar interaction between a free electron and a photon can not happen due to the conservation of energy and momentum. In fact, before the interaction the four-momentum of the system is $(E_\gamma + m_e, \vec{p_\gamma})$, after the interaction the four-momentum is $(E_e, \vec{p_e})$. So:

$$(E_\gamma + m_e, \vec{p_\gamma})^2 = (E_e, \vec{p_e})^2 \implies E_\gamma^2 + m_e^2 + 2E_\gamma m_e - p_\gamma^2 = m_e^2 \implies 2E_\gamma m_e = 0$$

that is impossible. In these relations we considered c = 1, and we used the fact that the Minkowski norm of the four momentum of a particle is equal to the square of the rest mass ($E^2 - p^2 = m^2$). For references see (Feynman et al. [2010]) or any other introductory book about special relativity.

[6]Also known as *incoherent scattering*, but more commonly referred to as the Compton effect in honor of Arthur Compton, who first measured photon-free electron scattering in 1922 [Compton [1923]].

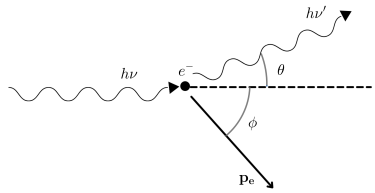

Figure 2.12: Sketch of the Compton effect.

For small scattering angles, only a small amount of energy is transferred to the electron. In the extreme case where $\theta = \pi$, part of the energy is retained by the photon, given by $h\nu'_{min}/h\nu = 1/(1 + 2h\nu/(m_e c^2))$. This behavior is clearer by plotting Equation 2.40 as a function of the angle for different energies, as done in Figure 2.13.

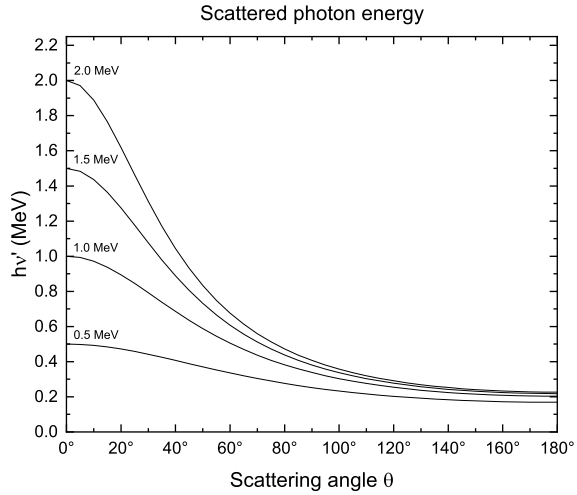

Figure 2.13: Energy of the photon emitted after Compton Scattering as a function of the scattering angle. It is interesting to note that for small angles almost all the energy is retained by the photon, and that even for wide scattering angles a small part of the energy is still hold by the photon.

The differential cross-section for Compton scattering between a photon and a free electron per unit solid angle, $d\sigma_C/d\Omega$, was determined by Oskar Klein and Yoshio Nishina in 1928 (Klein and Nishina [1929]):

$$\frac{d\sigma_C}{d\Omega} = \frac{r_e^2}{2}\left(\frac{\nu'}{\nu}\right)\left(\frac{\nu'}{\nu} + \frac{\nu}{\nu'} - \sin^2\theta\right) \tag{2.41}$$

where ν' depends on θ as given in Equation 2.40. The dependence of the differential cross-section on the incident beam energy is shown in Figure 2.14. It can be observed

that at high energies, forward scattering becomes more likely. At low energies ($\nu \to 0$ implying $\nu \approx \nu'$), the Klein-Nishina formula reduces to the well-known Thomson coherent scattering differential cross-section:

$$\frac{d\sigma_C}{d\Omega} = \frac{r_e^2}{2}(1 + \cos^2\theta). \tag{2.42}$$

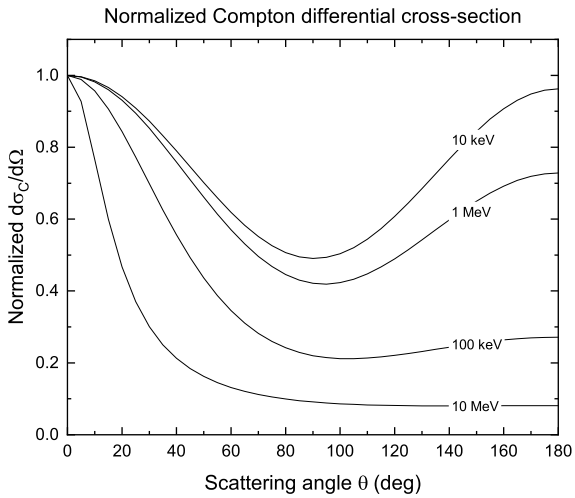

Figure 2.14: Normalized differential cross-section for the Compton effect as a function of the scattering angle at different incident photon energies.

Of particular interest for the gamma spectrometry is the energy distribution of the recoil electrons $d\sigma_C/dE_K$. As will be underlined in Chapter 4, the signal in γ-ray detectors is actually produced by electrons that are put in motion by the photons within the active volume of the detector itself and whose energy is interpreted as energy of the incident photon. Since this energy transfer, $E_K = h\nu - h\nu'$, is only partial, the Compton signal contributes as noise to the γ-ray spectrum. The shape and relative intensity of this noise can be derived from the Klein-Nishina formula (Equation 2.41):

$$d\sigma_C/dE_K = \frac{d\sigma_C}{d\Omega}\frac{d\Omega}{d\theta}\frac{d\theta}{dE_K} = \frac{\pi r_e^2}{\varepsilon h\nu}\left(2 - \frac{2E_K}{\varepsilon(h\nu - E_K)} + \frac{E_K^2}{\varepsilon^2(h\nu - E_K)^2} + \frac{E_K^2}{h\nu(h\nu - E_K)}\right) \tag{2.43}$$

where $\varepsilon = h\nu/m_e c^2$, $d\sigma_C/d\Omega$ is given by Equation 2.41, the factor $d\Omega/d\theta = 2\pi\sin\theta$ and $d\theta/dE_K = (d\theta/dE_K)^{-1}$ and can be derived from Equation 2.40. This equation is graphically presented in Figure 2.15. The shape of the recoil energy distribution is commonly called *Compton Edge* and is a feature present in every gamma spectrum. It is interesting to notice that increasing the energy of the incident photon, the maximum electron recoil energy approaches the limit value of $E_K^{max} = h\nu - m_e c^2/2$.

The Compton mass attenuation coefficient, proportional to the total cross-section, can be determined by integrating the Klein-Nishina equation over all the solid angles (Podgorsak [2016]):

$$\frac{\mu_C}{\rho} \propto \sigma_C \simeq \pi r_e^2 \frac{2\ln\varepsilon + 1}{2\varepsilon} \tag{2.44}$$

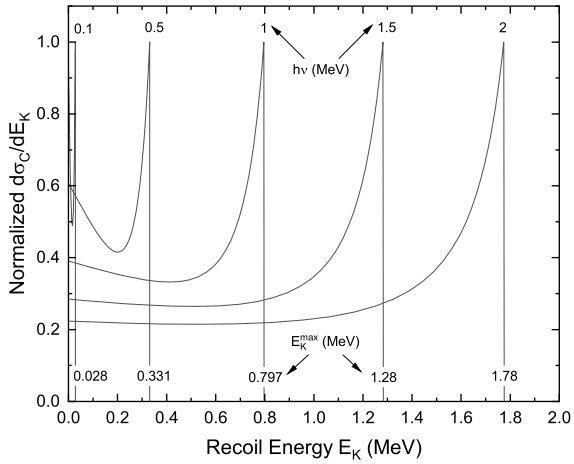

Figure 2.15: Normalized differential Compton cross-section per unit of kinetic energy of the recoiled electrons for different incident photon energies reported in the top part of the right-down part of each curve.

and its behavior as a function of the energy is reported in Figure 2.11.

Electron-positron pair production

A photon whose energy exceeds the limit value of $2m_ec^2$ = 1.022 MeV may undergo the physical process of pair production: the photon is completely absorbed by an atom with the subsequent emission of an electron-positron pair. The presence of the absorber atom is not important for the conservation of energy and total charge, but it is necessary for momentum conservation. Note that the absorber may be either the Coulomb field of the nucleus or the electrons[7]. For the latter process to happen, the threshold energy is $h\nu^{min} = 4m_ec^2$; however, its probability is negligible compared to the interaction with the nuclear field (Podgorsak [2016]).

The excess energy $\Delta E = h\nu - 2m_ec^2$ is available as kinetic energy for the two particles that leave the interaction point, and each combination of energy distribution among them is almost equally probable, with the exception of the extreme case where one particle takes all the energy, which is very unlikely to happen.

The mass attenuation coefficient of this process is

$$\frac{\mu_{PP}}{\rho} \propto Z^2 f(Z, h\nu) \tag{2.45}$$

where $f(Z, h\nu)$ is a complex function of the photon energy and the atomic number of the material. It should be noted that pair production is the predominant process at high energy, as shown in Figure 2.11.

[7]When the interaction occurs with the electric field of an electron, the process is referred to as *triplet production* since the atomic electron may also leave the atom after the collision.

As with positrons emitted after β^+ decay, the positron produced through the pair production process undergoes annihilation with an electron of the medium, resulting in the emission of two annihilation photons at 511 keV.

2.3 Elements of nuclear reaction theory

In the previous section we described the interaction of radiations with matter, and we always considered negligible the contribute of the interaction of a charged particle with the nucleus in terms of energy losses. However the impact of nuclear reactions on the properties of nuclei that compose the target material is not negligible at all.

Generally speaking, a nuclear reaction is the interaction between two nuclei, a nucleus and an elementary particle, or a nucleus and a photon. However for this thesis are of interests the reactions induced by "light" charged projectiles as protons, deuterons and α particles in the energy range of 5 MeV - 70 MeV. In this kind of reactions no mesons can be produced and there is not sufficient energy to transmute a proton in a neutron and vice-versa. Moreover, we will consider a reaction geometry in which there is a target at rest and the light charged particle is accelerated and impact on the target. We can summarize this process with the following formalism:

$$\mathrm{T\ (p,\ x)\ R} \tag{2.46}$$

where p in the accelerated particle that impact on the target nuclei T producing the species x and R. Usually R will be a heavy products that stops in the target[8] and x is a light particle that could eventually be measured. Is it also possible that more than one light particle (x_i) is emitted. As an example, the reaction induced by protons on ^{159}Tb that produces ^{155}Dy and five neutrons can be written as ^{159}Tb(p,5n)^{155}Dy.

Nuclear reactions can be categorized as follows [Krane [1988]]:

- *Scattering reactions*: T and R are identical nuclei, and the incoming projectile is the same as the outgoing light particle. Scattering can be further classified as *elastic* if the product remains in the ground state, or *inelastic* if the product is in an excited state (R^*). Example: ^{159}Tb(p,p)^{159}Tb*
- *Knock-out reactions*: Here, p is the same particle as x, but the reaction also results in the emission of additional particles. Example: ^{159}Tb(p,p 2n)^{157}Tb
- *Transfer reactions*: One or more nucleons are transferred between the projectile and the nucleus[9]. Example: ^{153}Eu(α,2n)^{154}Tb.

Another classification is possible based on the reaction mechanism:

- *Direct reactions*: In these reactions, only a few nucleons are involved. Transfer reactions are a significant subgroup of this category.
- *Compound nucleus*: The incoming particle temporarily merges with the target nucleus (for about 10^{-22} seconds), allowing complete energy sharing before an outgoing nucleon is emitted, involving all nucleons in the reaction.

[8] The recoil of these heavy products is possible in the most external layer of a target and is of particular relevance for thin targets as it will be discussed in Chapter 4, in the section dedicated to the description of the Stacked-foils technique.

[9] The first observed nuclear reaction was a transfer process between an α particle emitted after the decay of ^{214}Po, and a ^{14}N target. The reaction, observed by Rutherford in 1919, was ^{14}N(α, p)^{17}O.

- *Resonance reactions*: These are intermediate between direct and compound nucleus reactions. The incoming particle forms a "quasibound" state before a particle is emitted.

As for many others physical processes, some *conservation laws* apply to the nuclear reactions. The most classical are the conservation of the energy and of the linear momentum that will be discussed in the next paragraph. The total number of nucleons is also conserved, in particular, in the energy range here considered, the number of protons and neutrons are conserved separately. Other conservation laws must be considered, as the conservation of the angular momentum and of the parity (for reference see Krane [1988]).

Energetic aspects of nuclear reactions

The conservation of total energy and total linear momentum apply in nuclear reactions. Let's consider the reaction in Equation 2.46, we can write the conservation of the total energy as:

$$m_p c^2 + T_p + m_T c^2 = m_x c^2 + T_x + m_R c^2 + T_R \tag{2.47}$$

where $m_i c^2$ is the rest mass energy of the i-th particle, and T_i is the kinetic energy of the i-th particle. We assumed $T_T = 0$ since in our experiments the target is at rest so can be considered its nuclei T being the thermal energy negligible compared to the projectile's energy T_P. Moreover, in the case of $\beta \ll 1$, the non-relativistic definition of the kinetic energy is sufficient: $T_i = p_i^2/(2m_i)$, with p_i linear momentum of the i-th particle. As for decaying nuclei, it is possible to define the Q-value of a nuclear reaction as the difference between the masses at rest of the reactants and of the products:

$$Q = m_p c^2 + m_T c^2 - m_x c^2 - m_R c^2 = -T_p + T_x + T_R \tag{2.48}$$

where the second equivalence follows Equation 2.47. Based on the Q-value we can classify a nuclear reaction as Krane [1988]:

- *Exoergic (or Exothermic)* if $Q > 0$ and then $m_{\text{reactants}} > m_{\text{products}}$. In this case part of the nuclear mass is released as kinetic energy of the products
- *Endoergic (or Endothermic)* if $Q < 0$ and then $m_{\text{reactants}} < m_{\text{products}}$. The kinetic energy of the reactants is converted in mass energy of the products.

We can rewrite Equation 2.48 as:

$$Q + T_p = T_x + T_R \leq 0 \tag{2.49}$$

being the kinetic energy a positive quantity. This pose an important condition for a reaction to take place that, however, is a necessary but not sufficient condition. In fact the limit case $Q + T_p = 0$, the two products found themselves at rest after the reaction, therefore the linear momentum $\vec{p}$ is not conserved ($\vec{p}_{\text{reactants}} \neq \vec{p}_{\text{products}} = 0$).

To determine the minimum energy that allows a reaction to occur we must therefore consider the conservation of the linear momentum. Let's define the reaction plane as the plane individuated by the vectors of the products momenta $\vec{p}_R$ and $\vec{p}_x$ as represented in Figure 2.16, being θ and ϕ the angle between the projectile momentum $\vec{p}_p$ and the products momenta x and R, respectively.

We can write the conservation of the linear momentum in the direction of the incoming projectile and the perpendicular one as follow:

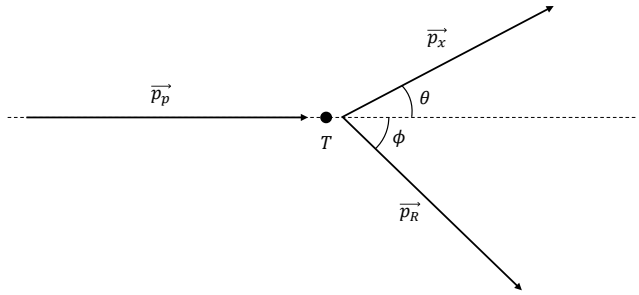

Figure 2.16: Schematic representation of a nuclear reaction. The target nucleus is assumed to be at rest in the laboratory system.

$$\begin{cases} p_p = p_x \cos\theta + p_R \cos\phi \\ 0 = p_x \sin\theta - p_R \sin\phi \end{cases} \tag{2.50}$$

Equations 2.50 and 2.47 constitute a set of three equations in four unknown (θ, ϕ, T_x and T_R) since the mass are well-known and the velocity of the projectile is a variable set by the experiment. We can use these equations to determine a relation between the energy of the produced light particle x and the angle θ. These two quantities are of particular interest in nuclear physics experiment because are easier to measure with respect to T_R and ϕ, since the heavier nucleus will hardly exit from the target.

Let's substitute $p_i = \sqrt{2m_iT_i}$:

$$\begin{cases} \sqrt{2m_pT_p} - \sqrt{2m_xT_x}\cos\theta = \sqrt{2m_RT_R}\cos\phi \\ \sqrt{2m_xT_x}\sin\theta = \sqrt{2m_RT_R}\sin\phi \end{cases} \tag{2.51}$$

Squaring the two terms of each equation:

$$\begin{cases} m_pT_p + m_xT_x\cos^2\theta - 2\sqrt{m_xT_pT_x}\cos\theta = m_RT_R\cos^2\phi \\ 2m_xT_x\sin^2\theta = 2m_RT_R\sin^2\phi \end{cases} \tag{2.52}$$

Summing the two equations and rearranging the terms we obtain:

$$m_pT_p + m_xT_x - m_RT_R - 2\sqrt{m_xT_pT_x}\cos\theta = 0 \tag{2.53}$$

To eliminate the dependence on T_R we can use Equation 2.48:

$$m_pT_p + m_xT_x - m_R(Q - T_x + T_p) - 2\sqrt{m_xT_pT_x}\cos\theta = 0 \tag{2.54}$$

and so:

$$(m_x + m_R)T_x - (2\sqrt{m_xm_pT_p}\cos\theta)\sqrt{T_x} - [(m_R - m_p)T_p + m_RQ] = 0 \tag{2.55}$$

that is a quadratic equation in $\sqrt{T_x}$ and that we can solve as:

$$\sqrt{T_x} = \frac{\sqrt{m_xm_pT_p} \pm \sqrt{\Delta/4}}{m_x + m_R} \tag{2.56}$$

where:

$$\frac{\Delta}{4} = m_x m_p T_p \cos^2\theta + (m_x + m_R)[(m_R - m_p)T_p + m_R Q] \tag{2.57}$$

From the latter two equations it is possible to derive three important features:

1. Equation 2.56 only has solution if $\Delta/4 > 0$, that is:

$$T_p > (-Q)\frac{(m_x + m_R)m_R}{m_x m_p \cos^2\theta - (m_x + m_R)(m_p - m_R)} \tag{2.58}$$

whose minimum value is found when $\theta = 0$:

$$T_p^{min} = (-Q)\frac{m_R + m_x}{m_R + m_x - m_p} = E_{Th} \tag{2.59}$$

Therefore, there is a minimum energy after which the reaction is possible from an energetic point of view, namely $T_p = E_{Th}$, and this value is called *Threshold Energy*. This only applies to endoergic reactions for which $Q < 0$. It should also be noted that this result has been obtained in the non relativistic approximation, if we release this hypothesis (see Bertulani [2007]) it is possible to obtain the condition:

$$T_p > E_{Th} = (-Q)\frac{m_p + m_T + m_x + m_R}{2m_T}. \tag{2.60}$$

2. Equation 2.56 has two possible solution for each angle θ, however the condition $\sqrt{T_x} \geq 0$ must be verified. We obtain that the two solutions are possible only if:

$$T_p < (-Q)\frac{m_R}{m_R - m_p} = T_p' \tag{2.61}$$

Nevertheless, this phenomenon is not very important in most of the cases discussed in this thesis for which $m_R >> m_p, m_x$. In fact, we can determine the energy range for which T_x can assume a double value:

$$T_p' - E_{Th} = E_{Th}\frac{m_p m_x}{m_R(m_R - m_p)}\left(\frac{1}{1 + m_x/m_R}\right) \simeq E_{Th}\frac{m_p m_x}{m_R(m_R - m_p)}\left(1 - \frac{m_x}{m_R}\right) \tag{2.62}$$

that is negligible if $m_R >> m_p, m_x$.

3. Exoergic reactions do not show any of the behaviors discussed above.

Coulomb barrier

The Coulomb barrier is the energy threshold that charged particles must overcome to approach closely enough for a nuclear reaction to occur. The Coulomb barrier energy E_{cb} can be mathematically described as:

$$E_{\text{cb}} = \frac{1}{4\pi\epsilon_0}\frac{Z_p Z_T e^2}{r_c} \tag{2.63}$$

where Z_P and Z_T are the atomic numbers of the projectile and target nuclei respectively, e is the elementary charge, ϵ_0 is the permittivity of free space ($\epsilon_0 \approx 8.854 \times 10^{-12}$ F$\cdot$ m^{-1}), and r_c is the distance of closest approach. This quantity r_c is the distance for which

the attractive nuclear force equals the repulsive electrostatic force. Assuming spherical symmetry we can represent the potential energy as a function of the distance from the center of the nucleus, as represented in Figure 2.17. The distance of closest approach can be approximated by the sum of the nuclear radii of the two interacting particles:

$$r_c \approx r_0(A_p^{1/3} + A_T^{1/3}) \tag{2.64}$$

where $r_0 \approx 1.2\,\text{fm}$ but it varies depending on the nuclear model, and A_p and A_T are the mass numbers of the projectile and target nuclei, respectively.

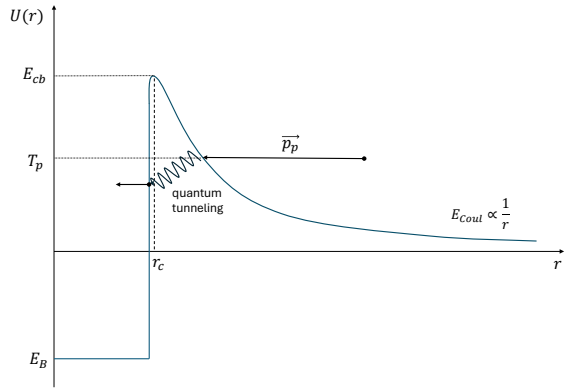

Figure 2.17: Schematic representation of the Coulomb barrier. The particle p has the possibility to cross it due to quantum tunneling effect even if $T_p < E^{cb}$. The graph is not in scale being the depth of the nuclear potential E_B much higher than the Coulomb barrier.

The kinetic energy T_p of the incident particle p must at least equal the Coulomb barrier E_{cb} to overcome the repulsive electrostatic force and allow the nuclear reaction to proceed:

$$T_p \geq E_{\text{cb}} \tag{2.65}$$

However, due to quantum tunneling, particles with kinetic energy less than the Coulomb barrier may still penetrate ("tunnel") this barrier. The probability of tunneling through the Coulomb barrier is given by the Gamow factor, which exponentially decreases with increasing of the difference between T_p and E_{cb} (See Bertulani [2007]). This effect is crucial in enabling nuclear reactions at energies that would otherwise be insufficient to overcome the barrier classically.

2.4 Cross-section determination

To describe the likelihood of interaction between incident particles and nuclei, it is crucial to introduce a formalism involving cross-sections. The cross-section, denoted by σ and typically measured in barns (b) or $10^{-24}\ cm^2$, represents the probability of a specific reaction occurring under well-defined conditions. The cross-section depends not only on the target, projectile, and their relative velocity but also on the particular physical phenomenon being investigated.

Consider a stream of incident particles moving uniformly towards a stationary target. The particle flux Φ, defined as the rate of particles passing through a unit area perpendicular to the motion, is given by $\Phi = n_p v$, where n_p is the particle density $[m^{-3}]$. The

reaction rate k [s^{-1}] for a nuclear reaction T(p,x)R is proportional to the incident flux Φ and the number of target nuclei N:

$$k = \sigma \Phi N \tag{2.66}$$

Here, σ is the event rate per target nucleus per unit incident flux. In the case of a unidirectional beam, Equation 2.66 can be reformulated as:

$$k = \sigma I \frac{N}{S} = \sigma I n_t x \tag{2.67}$$

where $I = \Phi S$ [s^{-1}] is the beam intensity, S is the cross-sectional area of the beam, and n_t is the number of target nuclei per unit volume (nuclei density).

For particle accelerators, the charged beam intensity I can be expressed as:

$$I = \frac{i}{q} = \frac{Q}{t_{irr} z e} \tag{2.68}$$

where i is the beam current [A], q is the particle charge [C], z is the atomic number of the projectile, e is the electron's charge, and $Q = i \cdot t_{irr}$ is the total charge impinging on the target. The beam intensity is typically considered constant throughout the target, being the target thickness lower than the projected range, and the beam assumed to be not divergent.

Considering a target with atomic mass M, the target nuclei density n_t is given by $n_t = \frac{\rho N_A}{M}$. Substituting this and Equation 2.68 into Equation 2.67 yields:

$$k = \frac{\rho x N_A Q}{M t_{irr} z e} \cdot \sigma \tag{2.69}$$

Here, ρx is the mass thickness, defined as $\rho x = \frac{m}{S_{target}}$, measured in g/cm^2.

2.4.1 Production of a Radionuclide by Irradiation

The production of a radionuclide R_1 through irradiation of a target nucleus T in a particle accelerator with projectile p, and its following decay in R_2, can be expressed as:

$$T(p,x)R_1 \rightarrow R_2 \tag{2.70}$$

The rate of production k is governed by Equation 2.69. The subsequent decay of R_1 to R_2, assumed stable in this section, is characterized by the decay constant λ. The net rate of R_1 production, dN_1/dt, considers both the production rate k and the decay rate:

$$\frac{dN_1}{dt} = k - \lambda N_1 \tag{2.71}$$

Integration of this equation with initial conditions $N_1(t=0) = 0$ and $N_1(t = t_{irr}) = N_1^{EOB}$ results in:

$$N_1^{EOB} = \frac{k}{\lambda}\left(1 - e^{-\lambda t_{irr}}\right) \tag{2.72}$$

After irradiation, the produced radionuclide continues to decay at a rate λ. At the beginning of a measurement at the time t_{cool} the number of nuclei of the R_1 species still present in the target are:

$$N_1(t_{cool}) = \frac{k}{\lambda}\left(1 - e^{-\lambda t_{irr}}\right) e^{-\lambda t_{cool}} \tag{2.73}$$

At the end of the measure of lenght RT [10] [s] the residual nuclei are:

$$N_1(t_{cool} + RT) = \frac{k}{\lambda}\left(1 - e^{-\lambda t_{irr}}\right) e^{-\lambda t_{cool}} e^{-\lambda \cdot RT} \tag{2.74}$$

The number of R_1 radionuclides that decayed during the measurement (ΔN_1) is given by:

$$\Delta N_1 = \frac{k}{\lambda}\left(1 - e^{-\lambda t_{irr}}\right) e^{-\lambda t_{cool}} \left(1 - e^{-\lambda RT}\right) \tag{2.75}$$

The activity A, defined as the number of nuclei decayed per unit time[11]:

$$A = -\frac{\Delta N}{\Delta t} = -\frac{\Delta N}{RT} \tag{2.76}$$

By substituting Equation 2.75 and Equation 2.69 into this relationship it is possible to obtain:

$$A = \frac{\sigma \rho x N_A Q}{Mze}\left(\frac{1 - e^{-\lambda t_{irr}}}{\lambda t_{irr}}\right)\left(\frac{1 - e^{-\lambda RT}}{RT}\right) \tag{2.77}$$

For symmetry of the terms in the brackets we multiply and divide by λ obtaining:

$$A = \frac{\sigma \rho x N_A Q \lambda}{Mze}\left(\frac{1 - e^{-\lambda t_{irr}}}{\lambda t_{irr}}\right)\left(\frac{1 - e^{-\lambda RT}}{\lambda RT}\right) \tag{2.78}$$

Thus, the nuclear cross-section σ for a specific reaction can be estimated experimentally:

$$\sigma = \frac{AMze}{\rho x N_A Q \lambda} G(t_{irr}) D(RT) e^{\lambda t_{cool}} \tag{2.79}$$

Here, G and D are adimensional correction factors compensating for decay during irradiation and measurement, respectively:

$$G(t_{irr}) = \frac{\lambda t_{irr}}{1 - e^{-\lambda t_{irr}}} \tag{2.80}$$

$$D(RT) = \frac{\lambda \cdot RT}{1 - e^{-\lambda \cdot RT}} \tag{2.81}$$

[10] RT refers to Real Time of the measurement, intended as the difference in seconds between the beginning of the measurement and the end of it. RT corresponds to the sum of the Live Time (LT) of the measurement in which the detector is active and the Dead Time (DT) when the detector is busy ($RT = LT + DT$). In this case RT must be used because R_1 decays also during the DT. Detailed description of these parameters is provided in Chapter 4.

[11] By calculating the activity in this way we take into account the exponential decay during the measurement. If one use the relation $A = \lambda N$ it is like considering the activity constant during RT. However the correction is small in the majority of the cases (i.e. when $RT \ll T_{1/2}$).

From an experimental point of view the activity can be calculated from the net counts ($Counts$) of a photo-peak as:

$$A = \frac{Counts}{LT \cdot I_\gamma \cdot \varepsilon} \tag{2.82}$$

where LT is the live time of the measurement[12], I_γ is the intensity of the emission and ε is the efficiency of the detector at that energy and geometry. Thus, to conclude the cross-section can be calculated as:

$$\sigma = \frac{Counts}{LT \cdot I_\gamma \cdot \varepsilon} \cdot \frac{Mze}{\rho x N_A Q \lambda} G(t_{irr}) D(RT) e^{\lambda t_{cool}} \cdot 10^{27} \tag{2.83}$$

where the factor 10^{27} is used to express σ in mb.

2.5 Production of cascade decaying nuclei

Here it is shown, in the case of $T(p,x)R_1 \rightarrow R_2 \rightarrow R_3$, how the cumulative cross-section of production of the radioactive specie R_2 depends on the irradiation time. To keep the discussion simple the decay during the measurement has been neglected, considering $LT << T_{1/2}$.

2.5.1 General solution of Bateman Equations with $N_i(0) \neq 0$

The Bateman equation for cascading decays has been presented earlier in this chapter (Equation 2.12), whose solution in the most general case, which includes production terms ($N_i(0) \neq 0$ for $i \neq 1$) given by Equation 2.14.

In the particular case of $n = 2$ we obtain:

$$\begin{cases} N_1(t) = N_1(0) \cdot e^{-\lambda_1 t} \\ \\ N_2(t) = N_1(0) \cdot \lambda_1 \cdot \left(\dfrac{e^{-\lambda_1 t}}{\lambda_2 - \lambda_1} + \dfrac{e^{-\lambda_2 t}}{\lambda_1 - \lambda_2} \right) + N_2(0) \cdot e^{-\lambda_2 t} \end{cases} \tag{2.84}$$

We can rewrite the second of Equation 2.84 as

$$N_2(t) = N_1(0) \frac{\lambda_1}{\lambda_2 - \lambda_1} \left(e^{-\lambda_1 t} - e^{-\lambda_2 t} \right) + N_2(0) \cdot e^{-\lambda_2 t}. \tag{2.85}$$

2.5.2 Production

The equations related to the production of RN with cascading decay are :

$$\begin{cases} \dfrac{dN_1}{dt} = k_1 - \lambda_1 N_1 \\ \\ \dfrac{dN_2}{dt} = k_2 - \lambda_2 N_2 + \lambda_1 N_1 \end{cases} \tag{2.86}$$

[12] In this case the Live Time (LT) must be used because the photons are detected only during this time. Using the Real Time (RT) lead to a underestimation of the activity because the same Counts are associated to a time that is longer that the time during which the detector is ready to measure.

Where k_i is the production rate of nucleus i.

$$k_j = \frac{\rho dx \cdot N_A \cdot i}{M} \cdot \sigma_j = \frac{\rho dx \cdot N_A \cdot Q}{M \cdot t_{irr} \cdot Ze} \cdot \sigma_j \tag{2.87}$$

From the first equation in Equation 2.86, we obtain:

$$N_1(t_{irr}) = \frac{k_1}{\lambda_1}\left(1 - e^{-\lambda_1 t_{irr}}\right) \tag{2.88}$$

Inserting this into the second equation in Equation 2.86, we find:

$$\frac{dN_2}{dt} + \lambda_2 N_2 = k_2 + k_1 \cdot \left(1 - e^{-\lambda_1 t}\right) \tag{2.89}$$

We then solve this first order differential equation with the condition $N_2(0) = 0$ as there are no nuclei of N_2 before irradiation:

$$N_2(t_{irr}) = e^{-\lambda_2 t_{irr}} \cdot \int_0^{t_{irr}} \left[k_1 \cdot \left(1 - e^{-\lambda_1 s}\right) + k_2\right] \cdot e^{\lambda_2 s} \cdot ds \tag{2.90}$$

Integrating, we get:

$$N_2(t_{irr}) = \frac{k_1}{\lambda_2}\left(1 - e^{-\lambda_2 t_{irr}}\right) + \frac{k_2}{\lambda_2}\left(1 - e^{-\lambda_2 t_{irr}}\right) - \frac{k_1}{\lambda_2 - \lambda_1}\left(e^{-\lambda_1 t_{irr}} - e^{-\lambda_2 t_{irr}}\right) \tag{2.91}$$

Gathering terms related to the production of the two RN, we obtain:

$$N_2(t_{irr}) = \frac{k_2}{\lambda_2}\left(1 - e^{-\lambda_2 t_{irr}}\right) + k_1 \cdot \left[\frac{1}{\lambda_2} - \frac{e^{-\lambda_2 t_{irr}}}{\lambda_2} - \frac{e^{-\lambda_1 t_{irr}}}{\lambda_2 - \lambda_1} + \frac{e^{-\lambda_2 t_{irr}}}{\lambda_2 - \lambda_1}\right] \tag{2.92}$$

Considering only the term multiplying k_1:

$$\frac{\lambda_2 - \lambda_1 + (-\lambda_2 + \lambda_1 + \lambda_2)\, e^{-\lambda_2 t_{irr}} - \lambda_2 e^{-\lambda_1 t_{irr}}}{\lambda_2 \cdot (\lambda_2 - \lambda_1)} = \tag{2.93}$$

$$\frac{1}{\lambda_2 - \lambda_1}\left[\left(1 - e^{-\lambda_1 t_{irr}}\right) - \frac{\lambda_1}{\lambda_2}\left(1 - e^{-\lambda_2 t_{irr}}\right)\right] \tag{2.94}$$

By renaming $H_i = \left(1 - e^{-\lambda_i t_{irr}}\right)$ and substituting into Equation 2.92 it is possible to obtain the equation describing the behavior of N_2 during irradiation:

$$N_2(t_{irr}) = \frac{k_2}{\lambda_2} H_2 + \frac{k_1}{\lambda_2 - \lambda_1}\left(H_1 - \frac{\lambda_1}{\lambda_2} H_2\right). \tag{2.95}$$

By substituting $t = t_{\text{irr}}$ into Equation 2.95, we obtain N_2^{EOB}, representing the count of species 2 nuclei produced after an irradiation of duration t_{irr}. Similarly, Equation 2.88 yields N_1^{EOB}, denoting the quantity of species 1 nuclei generated during the identical irradiation period.

To determine the cross-section of the specie R_2 we isolate k_2:

$$k_2 = \frac{\lambda_2 N_2^{EOB}}{H_2} + \frac{k_1}{\lambda 2 - \lambda_1}\left(\lambda_1 - \lambda_2 \frac{H_1}{H_2}\right). \tag{2.96}$$

where $\lambda_2 N_2^{EOB} = A_2^{EOB}$ Thus, the direct cross-section is:

$$\sigma_2 = \frac{M t_{irr} z e}{\rho x N_A Q} \frac{A_2^{EOB}}{H_2} + \frac{\sigma_1}{\lambda_2 - \lambda_1}\left(\lambda_1 - \lambda_2 \frac{H_1}{H_2}\right). \tag{2.97}$$

2.5.3 Cooling

Using the solutions Bateman equations (Eqs. 2.84 and 2.85) in the case of $n = 2$, it is possible to write:

$$A_2(t_c) = A_2^{EOB} e^{-\lambda_2 t_c} + \frac{\lambda_2 A_1^{EOB}}{\lambda_2 - \lambda_1} \left(e^{-\lambda_1 t_c} - e^{-\lambda_2 t_c} \right) \tag{2.98}$$

where t_c is the cooling time. If we calculate A_2^{EOB} we obtain:

$$A_2^{EOB} = A_2(t_c) e^{\lambda_2 t_c} - \frac{\lambda_2 A_1(t_c)}{\lambda_2 - \lambda_1} \left(e^{\lambda_2 t_c} - e^{\lambda_1 t_c} \right). \tag{2.99}$$

The latter equation may be substituted in Equation 2.97 to determine the direct production cross-section when the activity A_1^{EOB} can be experimentally determined.

2.5.4 Cumulative cross-section

Cumulative cross-section is generally used when parent-daugher species are produced during an irradiation and for some reason it is not possible to measure the cross-section of the parent radionuclide. It may be useful for deducing independent cross-section for the formation of the longer-lived daughter, if you may measure formation cross-section of the parent and cumulative of the daughter as it will be shown in this paragraph. Additionally it may be used for estimating available yield of the daughter after the total decay of the parent.

To describe the behavior of N_1 and N_2 in the period between the End of Bombardment (EOB) and the start of the measurement (t_c), we can use the expression in Equation 2.84, but this time replacing $N_1(0)$ and $N_2(0)$ with the expressions in Equation 2.88 and Equation 2.95, respectively. We obtain:

$$\begin{cases} N_1(t_c) = \dfrac{k_1}{\lambda_1} H_1 e^{-\lambda_1 t_c} \\ \\ N_2(t_c) = \dfrac{k_1}{\lambda_1} H_1 \dfrac{\lambda_1}{\lambda_2 - \lambda_1} \left(e^{-\lambda_1 t_c} - e^{-\lambda_2 t_c} \right) + \dfrac{k_2}{\lambda_2} H_2 \cdot e^{-\lambda_2 t_c} + \dfrac{k_1}{\lambda_2 - \lambda_1} \left(H_1 - \dfrac{\lambda_1}{\lambda_2} H_2 \right) \cdot e^{-\lambda_2 t_c} \end{cases} \tag{2.100}$$

Working on the second equation and collecting terms in k_1:

$$N_2(t_c) = \frac{k_1}{\lambda_2 - \lambda_1} \left[H_1 \cdot e^{-\lambda_1 t_c} - H_1 \cdot e^{-\lambda_2 t_c} + H_1 \cdot e^{-\lambda_2 t_c} - \frac{\lambda_1}{\lambda_2} H_2 \cdot e^{-\lambda_2 t_c} \right] + \frac{k_2}{\lambda_2} H_2 \cdot e^{-\lambda_2 t_c} \tag{2.101}$$

Simplifying, we get the desired expression for N_2:

$$N_2(t_c) = \frac{\lambda_1}{\lambda_2 - \lambda_1} k_1 \cdot \left[\frac{H_1}{\lambda_1} \cdot e^{-\lambda_1 t_c} - \frac{H_2}{\lambda_2} \cdot e^{-\lambda_2 t_c} \right] + \frac{k_2}{\lambda_2} H_2 \cdot e^{-\lambda_2 t_c} \tag{2.102}$$

From this expression, we can obtain the activity as:

$$A_2(t_c) = \lambda_2 N_2(t_c) = \frac{k_1}{\lambda_2 - \lambda_1} \cdot \left[\lambda_2 H_1 \cdot e^{-\lambda_1 t_c} - \lambda_1 H_2 \cdot e^{-\lambda_2 t_c} \right] + k_2 H_2 \cdot e^{-\lambda_2 t_c} \tag{2.103}$$

At this point, what usually is done to calculate the cumulative cross-section is to shift this measurement at the EOB simply multiplying the Equation 2.103 by the exponential factor: $e^{\lambda_2 t}$. Doing so, what we actually obtain is:

$$A_2 \cdot e^{\lambda_2 t} = \frac{k_1}{\lambda_2 - \lambda_1} \cdot \left[\lambda_2 H_1 \cdot e^{(\lambda_2 - \lambda_1)t_c} - \lambda_1 H_2\right] + k_2 H_2 \tag{2.104}$$

Explicitly expressing k, and collecting the factor H_2 we obtain:

$$A_2 \cdot e^{\lambda_2 t} = \frac{N_A \cdot I \cdot \rho dx}{M \cdot Ze} \cdot H_2 \left[\sigma_2 + \frac{\lambda_1}{\lambda_2 - \lambda_1}\sigma_1 \cdot \left(\frac{\lambda_2 H_1}{\lambda_1 H_2} e^{(\lambda_2 - \lambda_1)t_c} - 1\right)\right] \tag{2.105}$$

Expressing $I = Q/t_{irr}$, $H_2 = 1 - e^{-\lambda_2 t_{irr}}$, and multiplying and dividing by λ_2 we obtain:

$$A_2 \cdot e^{\lambda_2 t} = \frac{N_A \cdot Q \cdot \rho dx \cdot \lambda_2}{M \cdot Ze} \cdot \left(\frac{1 - e^{-\lambda_2 t_{irr}}}{\lambda_2 t_{irr}}\right) \cdot \left[\sigma_2 + \frac{\lambda_1}{\lambda_2 - \lambda_1}\sigma_1 \cdot \left(\frac{\lambda_2 H_1}{\lambda_1 H_2} e^{(\lambda_2 - \lambda_1)t_c} - 1\right)\right] \tag{2.106}$$

By comparing this with Equation 2.79 in the case in which $D(RT) \simeq 1$ (i.e. when $RT \ll T_{1/2}$), we can state that what we determine as cumulative cross-section is:

$$\sigma_2^{cum} = \sigma_2 + \frac{\lambda_1}{\lambda_2 - \lambda_1}\sigma_1 \cdot \left(\frac{G_2}{G_1} e^{(\lambda_2 - \lambda_1)t_c} - 1\right) \tag{2.107}$$

which depends on t_{irr} through the factors G_i, and on the cooling time.

With some effort it is also possible to take into account the decay during the measurement, renouncing to the hypothesis of $D(RT) \simeq 1$ as done by Adam et al. [2002]. The result is an incredibly simple and symmetric equation:

$$\sigma_2^{cum} = \sigma_2 + \frac{\lambda_1}{\lambda_2 - \lambda_1}\sigma_1 \cdot \left(\frac{G_2 \cdot D_2}{G_1 \cdot D_1} e^{(\lambda_2 - \lambda_1)t_c} - 1\right) \tag{2.108}$$

which depends on t_{irr} through the factors G_i, on RT through D_i and on the cooling time t_c. These dependencies may be eliminated in some cases. For example: if $\lambda_1 \gg \lambda_2$ the exponential term goes to zero, eliminating the dependency on t_{irr} for sufficiently long t_c and

$$\sigma_2^{cum} = \sigma_2 + \frac{\lambda_1}{\lambda_1 - \lambda_2}\sigma_1. \tag{2.109}$$

This hypothesis is verified in the case of very short half-lives parent radionuclides that are no longer measurable at the time of the beginning of the counting session.

CHAPTER 3

Experimental techniques and facilities

For the determination of the nuclear cross-sections, the characterization of the materials and the chemical analysis in the radiochemistry studies, different experimental techniques have been employed. Some of these techniques will be here described with a certain grade of details being of great relevance for the outcome of the work. These include the γ-ray spectrometry, the stacked foils technique, and the inductively coupled plasma optical emission spectroscopy (ICP-OES). Some other complementary techniques will be presented shortly, comprising the alpha spectrometry and the autoradiograph with phosphorimaging systems. The facilities in which the experiments have been performed will be described here as well. The irradiations, the chemical studies and part of the nuclear measurements were performed at GIP ARRONAX (Saint-Herblain, France), the stack preparation and the majority of the γ-ray spectrometry measurements have been performed at LASA Laboratory (Segrate, Italy).

3.1 Radiation measurement techniques

Radiations, in order to be revealed, must undergo to one of the interactions processes described in Chapter 2 and release their energy to the electrons (and to the positrons in the case of pair production) of the the detector. In active detectors, this energy is converted in an analogical and, subsequently, in a digital signal to be analyzed. Each detector is characterized by some parameters, as efficiency, energy resolution, optimal detection range and by a specific response function to the interaction with the radiation. These characteristics are described in some detail for γ-ray spectrometry and shortly for alpha spectrometry.

3.1.1 γ-ray spectrometry

γ-ray spectrometry is a quantitative technique that permits to determine the nature and the intensity of a source emitting γ rays. This technique includes a number of subtechniques and correspondent detectors, that differ from each other in the working principle, i.e. the way in which the photon energy is transformed in a useful signal. These include scintillation detectors and semiconductor-based detectors. In this work only the latter kind of detectors have been used, but anyway the description of the technique will be kept as general as possible with the exception of the description of the experimental apparatus that is specific of the detectors employed.

Interactions of γ rays with the detector: building of the response function

In Chapter 2, we described the interactions of γ rays with matter. In this section, we will apply that knowledge to understand the main features of a spectrum, specifically the histogram that shows the distribution of energy deposited by photons within the detector.

Ideally, the spectrum of a single γ ray emitting source should consist of a single peak corresponding to the photon's energy. However, in practice, the spectrum is much more complex, as shown in Figure 3.1. This complexity arises from two principal phenomena: incomplete absorption of the photon within the detector and interactions with the shielding. To fully explain the features of the ^{40}K (E_γ=1460.82 keV) source spectrum depicted in Figure 3.1, we must consider all possible interactions with the detector and the shielding, as illustrated in Figure 3.2. Seven different interaction histories have been considered: scenarios 1-4 relate to interactions with the detector, while the remaining scenarios pertain to interactions with the shielding. Let's discuss them in details:

1. The photon labeled as γ_1 interacts within the detector via the photoelectric effect (PE), transferring its entire energy to an electron in the medium (indicated by the blue arrow) and eventually to low-energy X-rays that are absorbed within the medium. This kind of interactions result in a photo-peak corresponding to the energy of γ_1.

2. In the case of Compton Scattering (CS) interaction, as with γ_2, a second photon is produced. This photon may release its whole energy inside the detector via the PE effect, undergo subsequent non-PE interactions, or escape from the detector. If the photon escapes, the energy released within the detector, i.e., the energy transferred to the electron, depends on the scattering angle. The distribution of the electron's energy is known as the Compton Edge (or Compton Continuum), described by Equation 2.43 and depicted in Figure 2.15. As stated in Section 2.2.2, there is a non-zero minimum energy retained by the photon undergoing CS, corresponding to the scattering angle $\theta = 180°$ (see Equation 2.40). Therefore, the maximum energy for the electron is:

$$E_K^{max} = h\nu - h\nu'_{min} = \frac{h\nu}{1 + \dfrac{m_e c^2}{2h\nu}} \overset{h\nu \gg 1}{\longrightarrow} h\nu - \frac{m_e c^2}{2} \tag{3.1}$$

   The Compton continuum constitutes an unavoidable background, although some Compton suppression strategies are possible (Gilmore [2008]). If the second photon is completely absorbed by the detector, there would be no difference between this scenario and a single PE event, as the time resolution is not high enough to separate the two contributions. This results in an additional count in the full energy peak. The probability of complete absorption depends on the detector's size, with larger detectors exhibiting a reduced Compton Edge.

3. Counts between the upper limit of the Compton edge and the photo-peak are due to multiple CS events. The photon γ_3 follows a more complex path: after an initial CS, the produced photon undergoes a second CS. If the third interaction is a PE, there would be no difference between the effects of γ_1 and γ_3, and the registered energy would be the energy of the incoming photon. However, if the photon produced in the second interaction exits the detector, the energy released will be lower than the energy of γ_3, but not limited by the constraint of Equation 3.1. The contribution of multiple CS is clearly visible in the spectrum shown in Figure 3.1.

4. If the energy of the photon is higher than $2m_ec^2$, the photon γ_4 may interact via pair production (PP), generating an electron-positron pair (e^-/e^+). The positron (green arrow) releases its energy in the medium and then annihilates, producing two backscattered photons of fixed energy equal to m_ec^2 (green waves, labeled γ_{511} in Figure 3.2). If both photons are absorbed in the detector, a new count will be added to the photo-peak. Otherwise, the escape of one or both annihilation photons will produce two additional peaks at energies ($h\nu - 511$ keV) - the *single escape peak* - or ($h\nu - 1022$ keV) - the *double escape peak*. These spurious signals increase the probability of overlapping with photons genuinely emitted by the sample, complicating the analysis. It is common practice, when identifying an unknown peak, to check if it corresponds to the single or double escape of a higher energy peak. In Figure 3.3 it is possible to notice that the emission of ^{137}Cs at 661.7 keV does not produce any escape peak, since its energy is lower than the threshold energy of PP.

5. The photon γ_5 emitted by the source S interacts with the lead shielding used to reduce the contribution of natural radiation background to the signal. In this case it interacts by PE. As said in Section 2.2.2, following the PE interaction Auger electrons or characteristic X-rays may be emitted as a consequence of the reconfiguration of the atomic electrons. If the interaction with the shielding happens in the outer layer it is possible that these photons reach the detector producing some peaks in the energy range of 70-90 keV. This may be a problem in the case in which low energy γ rays has to be used to determine the activity of a radionuclide. To reduce the contribute of the X-rays it is possible to use a Graded Shielding composed of a thick layer of Pb to shield from the background, followed by a layer of Cd or Sn to adsorb the higher energy X-rays, followed by a thin layer of Cu to adsorb the low energy X-rays (around 30 keV) produced in the previous layer. In addition to remove the 7-8 keV X-rays of Cu and to provide a simple-to-clean layer in case of contamination a removable plastic layer may be added.

6. In the spectrum in Figure 3.1 a peak around 511 keV is visible. If the source does not decay via β^+ and the energy of the emitted photons is higher than $2m_ec^2$, this peak is mainly due to PP within the shielding, with one of this photon reaching the detector. Note that for lower energy γ rays this contribution is absent as it is obvious from Figure 3.3.

7. Lastly, the photon γ_7 undergoes CS with the shielding. In order to reach the detector the resulting photon should be backscattered (scattering angle $\theta \simeq 180°$). If we graph the energy of the scattered photon as a function of the angle (see Figure 2.13) we notice that the energy is in the 200-300 keV range for higher energy photons and in the 150-250 keV range for lower energy photons. The backscattering broad peak is clearly visible in the example spectra in Figure 3.1 and 3.3.

Some additional effects, not represented in Figure 3.2, are present:

- A β emitting source may produce a Bremsstrahlung signal due to the interaction of the electrons with the source itself. This represent an additional background that makes more complex the analysis of the low energy peaks.

- Natural radionuclides (^{40}K, the members of the primordial natural decay-chains and cosmogenic radionuclides) may interact with the detector even if a proper shielding is provided. The higher energy photons also contribute to the background due to their Compton Edge (see Figure 3.3).

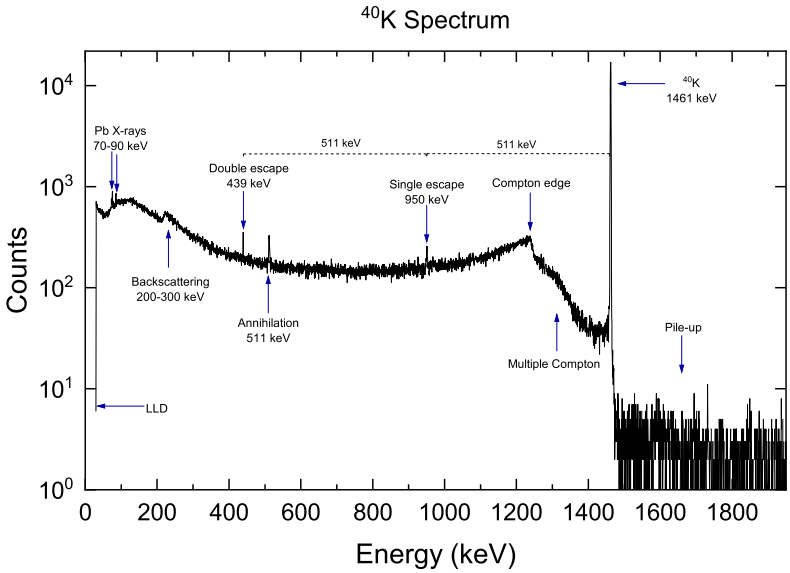

Figure 3.1: Single γ ray emitting source spectrum, in particular of ^{40}K (E_γ=1460.82 keV). The effects discussed in the text are here highlighted. Vertical axis is in log-scale.

- The pile-up signal is generated when more than one photon interact with the detector "simultaneously", i.e. at distance shorter than the time resolution of the detector. In this case, they will be considered as a single signal at energy equal to the sum of the two photons, producing a background signal at energy higher than the photo-peak.

In the example provided source emitting only one intense photon is discussed. The spectra may achieve very high complexity when hundreds of γ rays are emitted by tens of radionuclides present in the sample. Each photo-peak is surrounded by a background to be eliminated in order to determine the activity of the radionuclide. In the most simple and common case, when no inteference of multiple peaks are present, the background is obtained as average of 3-5 channel at the left and at the right of the peak and subtracted by the Gross Area to obtain the Net Area (Net Counts). In more complex spectra, a fitting of the background may be required. As an example, a stepped function may be required to subtract the background of the ^{40}K peak at 1461 keV in Figure 3.1 due to the high difference in background level caused by the strong impact of multiple CS on the left side. To do that the OriginPro data analysis software (OriginLab Corporation [2022]) has been used, through the function Peak-fit, that permitts to estimate the background and the net area of the peak. At the same time, if necessary it permits to deconvolve complex spectra with multiple peak superposition. An example is reported in Figure 3.4.

HPGe detectors

Semiconductor detectors are fundamental in γ-ray spectrometry due to their ability to convert γ ray energy into an electrical signal. The essential characteristic of a semiconductor is its ability to have its electrical conductivity modulated by the introduction of

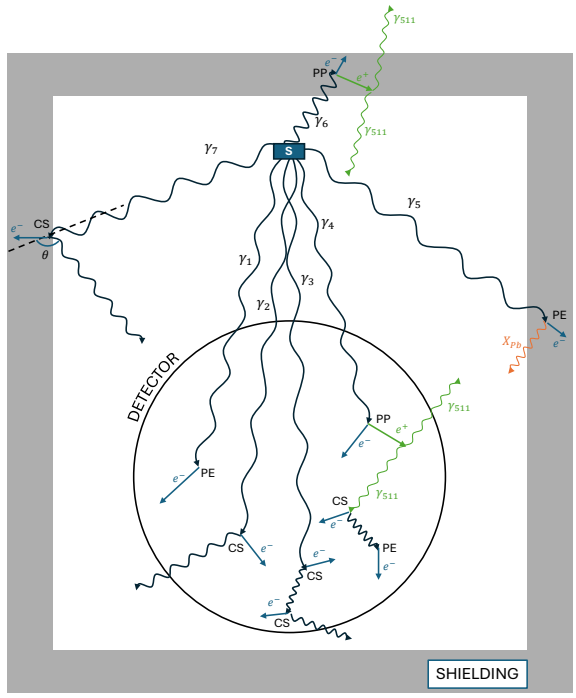

Figure 3.2: Example of 7 possible interaction histories of γ rays in a real-sized detector and effects of the interactions with the shielding. Each interaction is labeled as PE (photoelectric), CS (Compton Scattering) or PP (Pair Production). All photons are represented as blue waves, with exception of the X-rays emitted by the shielding in orange and the annihilation photons (here labeled γ_{511}) in green. Electrons are represented by a blue arrow and positrons by a green arrow. The photons produced by the interaction of γ rays with the shielding do not reach the detector in the picture to avoid confusion between the histories.

impurities, known as doping. The primary materials used in semiconductor detectors include germanium and silicon, with high-purity germanium (HPGe) being the preferred choice for γ-ray spectrometry due to its superior resolution capabilities compared to other materials.

The crystalline structure of a material broadens the energy levels of the atomic electrons into bands separated by forbidden regions. When the electron is in one of these bands, it is bonded to the atom. The behavior of a material mainly depends on the electrons that occupy upper band, namely the *valence band*. To migrate, i.e. to produce electrical current, electrons must be promoted to a non fully bonded energy level, namely the *conduction band*. When this happens, a electron-hole (e-h) pair is created. It must be noted that also holes, i.e. positively charged ions, have a certain grade of mobility and contribute to the current.

Depending on the material, the band gap (E_g) between the valence and conduction bands varies: in conductor the two bands are partially overlapped therefore no additional energy is required, in insulator the energy gap is of the order of 10 eV. Semiconductor are somehow in the middle, with an energy gap of the order of 1 eV (E_g = 0.67 eV for Ge) allowing for controlled conductivity, especially under the influence of external factors like temperature or doping. In a pure germanium crystal at room tem-

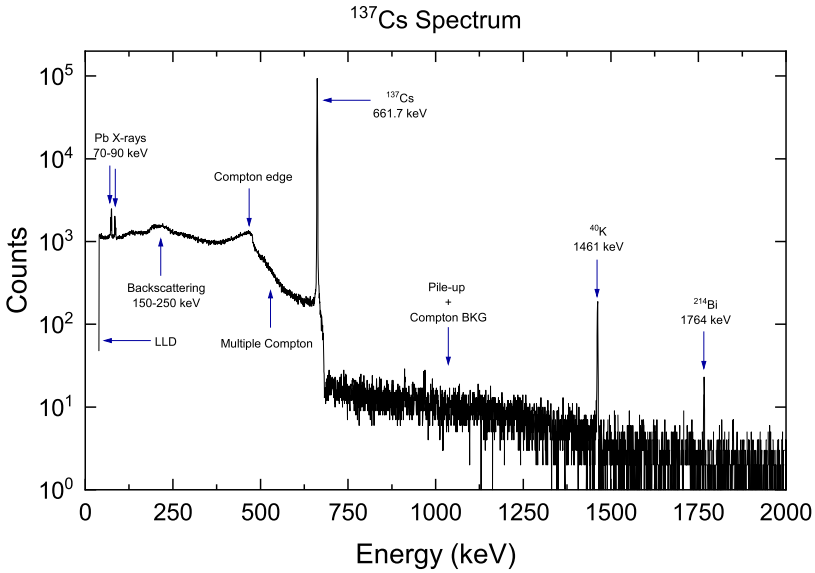

Figure 3.3: Single γ ray emitting source spectrum, in particular of ^{137}Cs (E_γ=661.7 keV). The natural background radiation (^{214}Bi - family of ^{238}U - and ^{40}K) is clearly visible. The effects discussed in the text are here highlighted. Vertical axis is in log-scale.

perature, thermal excitation is able to produce e-h pairs, producing leakage current that is detrimental when using Ge as detectors. The probability of thermal promotion to the conduction band strongly depends on the temperature (T) according to the Boltzmann equation:

$$p(T) \propto T^{3/2} e^{-\frac{-E_g}{2kT}} \tag{3.2}$$

where k is the Boltzmann constant. HPGe detectors are always employed at low temperatures to reduce this probability and the thermal noise, usually using liquid nitrogen at the temperature of 77 K. Key components of the cooling system include:

- Dewar Flask: A vacuum-insulated container that holds liquid nitrogen. The Dewar flask is insulated to minimize heat transfer, keeping the nitrogen liquid for extended periods.

- Cold Finger: A thermally conductive rod that connects the detector to the liquid nitrogen reservoir, ensuring efficient heat transfer.

A simplified schematic representation of this system is depicted in Figure 3.5. Modern cooling systems include electrical cooling devices that offer an alternative method for maintaining low temperatures without the need for liquid nitrogen, or electrical reliquefaction based systems that allows to recover evaporated nitrogen reducing the need for periodic refilling of the Dewar flask.

The intrinsic conductivity of a semiconductor is determined by the thermal excitation of electrons from the valence band to the conduction band. This intrinsic conductivity can be significantly modified by introducing impurities through a process called doping.

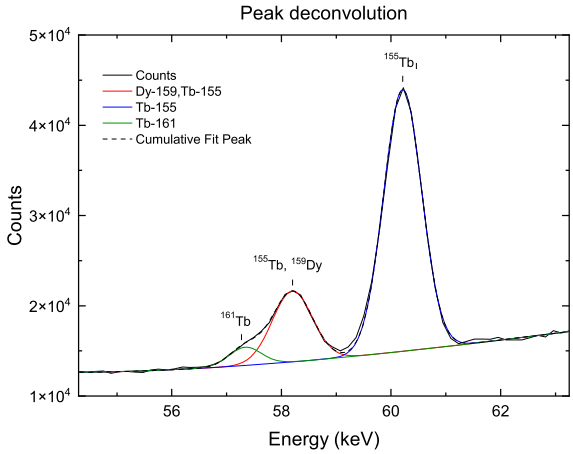

Figure 3.4: Example of complex spectra deconvolution abd background subtraction using OriginPro Peak fit function (OriginLab Corporation [2022]). In particular three peaks in the energy range between 56 and 62 keV have been deconvoluted. The name of the radionuclide emitting the γ rays is reported on the peak itself.

Depending on the type of impurity added, the semiconductor can become either n-type or p-type[1].

- N-type Semiconductors are created by doping the semiconductor with donor atoms that have more valence electrons than the semiconductor material. For germanium, typical donor atoms are arsenic or phosphorus. These additional electrons are loosely bound and can easily move to the conduction band, increasing the material's conductivity.
- P-type Semiconductors are formed by doping the semiconductor with acceptor atoms that have fewer valence electrons than the semiconductor material. For germanium, typical acceptor atoms are boron or gallium. The absence of an electron creates a "hole" in the valence band, which can move through the material as nearby electrons fill the vacancy, effectively creating positive charge carriers.

A p-n junction is formed when p-type and n-type semiconductors are joined together. At the junction, electrons from the n-type region fill holes from the p-type region, creating a depletion region devoid of free charge carriers. This depletion region acts as an insulating barrier preventing current flow under equilibrium conditions. Applying a bias voltage across the p-n junction modifies its properties. In HPGe detectors, reverse bias is applied: a positive terminal is connected to the n-type and the negative terminal to the p-type. In this way, the depletion region widens, preventing charge carriers from crossing the junction and thus inhibiting thermal current flow. The voltage is set to ensure that the entire volume of the detector is active for γ ray detection, being the dimension of the depletion region proportional to the bias voltage. The depletion region dimension also inversely depends on the concentration of impurities, for this reason high purity material are employed (Knoll [2010]).

[1]These concepts are here extremely simplified for the sake of conciseness, a complete discussion may be found in Gilmore [2008] or in Lutz [2007].

HPGe detectors can be constructed using either p-type or n-type germanium. The choice between p-type and n-type affects the detector's performance characteristics and its resistance to radiation damage.

- *N-type HPGe detectors* are manufactured using high-purity n-type germanium, where lithium or other donor impurities are diffused into the material to create an n- contact on one side, while a thin p+ contact is created on the other side through ion implantation. N-type detectors are more resistant to radiation damage because electrons, which are less susceptible to trapping than holes, are the majority carriers. The structure of an n-type HPGe detector allows for excellent resolution and efficiency, especially at low γ ray energies.

- *P-type HPGe detectors*, on the other hand, are made from high-purity p-type germanium. A thick p+ contact is created on the outer surface, while a thin n- contact is created on the inner surface. This configuration is generally less resistant to neutron damage, while the primary advantage of p-type detectors is their ability to handle higher γ ray energies efficiently.

In this work both type of detectors have been employed.

HPGe detectors come in various geometries tailored to specific applications, with coaxial detectors being one of the most common forms due to their large active volumes and high efficiency, and also being the only one employed in this work. These detectors have a cylindrical shape with a central cavity (coaxial geometry). They can be either closed-end or open-end coaxial detectors. The central cavity serves as the anode (for p-type) or the cathode (for n-type), with the outer surface forming the opposite electrode. This design allows for a large volume of active material, making it highly efficient for detecting gamma rays. Other geometries include planar and well detectors (See Gilmore [2008] for further details).

Electronics for γ-ray spectrometry with HPGe

The electronic system in γ-ray spectrometry is designed to collect, process, and analyze the electrical signals generated by the semiconductor detector. The key components include high voltage (HV) supplies, preamplifiers, amplifiers, Analog-to-Digital Converters (ADC), and Multi-Channel Analyzers (MCA). A scheme of the detector and its electronics is reported in Figure 3.5.

The electronic chain is composed of a series of modules conform to the *Nuclear Instrumentation Module* (NIM) standard. It was developed to ensure compatibility and interoperability between different modules used in nuclear and particle physics experiments. NIM units, or modules, are designed to fit into a standard NIM-bin, which provides the necessary power supplies and physical housing. Each module performs a specific function, and can be combined in various configurations to build a complete spectrometry system. The modularity of NIM allows for flexibility in system design and easy replacement or upgrading of individual components.

The charge collection process in HPGe detectors involves the movement of electron-hole pairs created by γ ray interactions within the germanium crystal. When a γ ray photon interacts with the detector, it creates a primary electron with sufficient energy to generate multiple secondary electron-hole pairs. An applied electric field across the detector sweeps these charge carriers toward their respective electrodes: electrons move toward the positive electrode, and holes move toward the negative electrode. The efficiency of this process depends on the mobility of the charge carriers and the presence

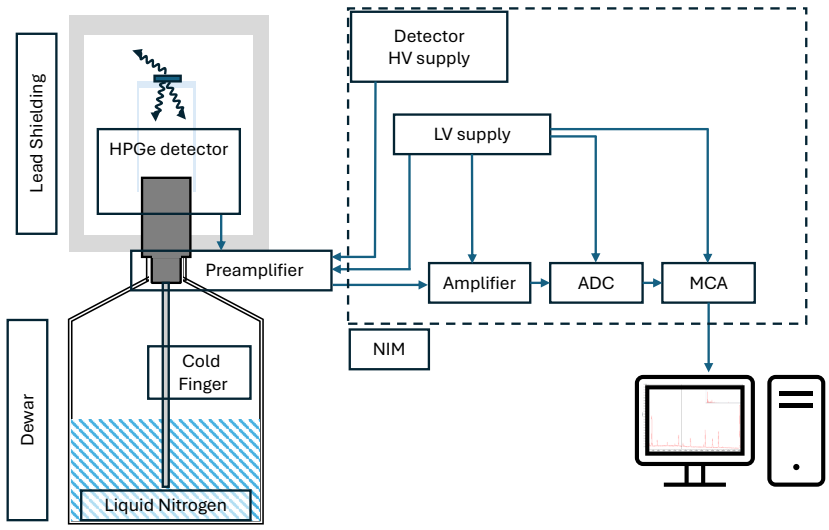

Figure 3.5: Schematic representation of the electronic chain of a HPGe detector.

of any traps or defects in the crystal lattice. In an ideal detector, all charge carriers would reach the electrodes, generating a signal proportional to the energy of the incident gamma ray. However, imperfections and traps in the crystal can capture carriers, leading to incomplete charge collection and degraded resolution.

The detector bias supply is therefore crucial. Typically, HPGe detectors require bias voltages of 3000V up to 5000V that are provided by HV units through the preamplifier: depending on the detector type the bias will be positive (p-type) or negative (n-type). The stability of the bias supply is essential but not critically demanding, as long as it remains above the depletion voltage. Modern bias supplies include features like automatic shutdown to prevent damage when detectors warm up and to protect current-limiting circuits against excessive leakage currents. The remaining electronics bias supply is provided by a Low Voltage unit that usually works in the 0-10 V range.

The *preamplifier* serves as the interface between the detector and the amplifier. Its primary function is not to amplify the pulse but to collect the charge generated by the detector and convert it into a voltage pulse. Charge-sensitive preamplifiers are preferred in high-resolution γ-ray spectrometry due to their noise performance and gain independence from detector capacitance. They integrate the charge over time using a feedback capacitor (C) and resistor (R), producing a step-change in voltage with a fast rise time and a long decay time τ = R·C. The amplitude of the signal is directly proportional to the collected charge. The preamplifier is closely connected to the detector in the cooling system to prevent thermal noise to be successively amplified.

The *amplifier*'s role extends beyond mere amplification of the signal; it includes pulse shaping, pole-zero cancellation, and baseline restoration. Amplifiers process the sharp pulses from the preamplifier to produce a pulse shape suitable for peak height measurement, crucial for determining the γ ray energy. *Pulse shaping* involves using filters to modify the pulse shape, optimizing it for accurate peak height measurement. The filters used can be high-pass (differentiators) or low-pass (integrators), with combinations like CR-nRC (circuits Resistor-Capacitor) filters being common. A good shaping reduces noise and improves resolution by producing pulses with a gradual rise and fall, mini-

mizing the effects of pulse pile-up. *Pole-zero cancellation* corrects the baseline shift caused by the exponential decay of the preamplifier output pulse. By matching the decay time constant of the preamplifier with the time constant of the amplifier's pole-zero network, the baseline shift is neutralized, ensuring accurate pulse height measurement which is directly proportional to the γ ray energy. Under-compensated or over-compensated signals lead to peaks with left or right tails respectively. Other functions of the amplifier include: the *pile-up rejections* that is a system to prevent random summing of two consequent events, and the actual *amplification of the signal* to be transferred to the ADC.

The *ADC* converts the analog pulse height information into a digital format for further processing by the MCA. Two main types of ADCs used in γ-ray spectrometry are the Wilkinson ADC and the Successive Approximation ADC. Wilkinson ADC measures the pulse height by charging a capacitor to the pulse's peak voltage and then linearly discharging it. The discharge time, proportional to the pulse height, is counted using a high-frequency clock, converting the analog signal into a digital number. With this system high energy signals require more time to be processed. Successive Approximation ADC compares the input pulse height against a series of reference voltages, refining the comparison in successive steps to achieve a precise digital representation of the pulse height. In this way the time to process all the signals is approximately the same.

The *MCA* sorts the digitized pulses by their height in different channels from 0 to 2^{n-1} (with n = 7-8 used in this work), corresponding to the γ ray energy, and counts the number of pulses within each energy interval. The result of this operation is a histogram, i.e. the *spectrum*.

Digital Pulse Processing (DPP) systems represent a significant advancement in the field of γ-ray spectrometry, performing functions traditionally handled by analog systems, but with enhanced precision and flexibility. Unlike conventional systems that rely on analog circuits for pulse shaping, amplification, and conversion, DPP systems digitize the preamplifier pulses using high-speed Analog-to-Digital Converters (ADCs), allowing subsequent digital manipulation of the signal. A typical DPP system includes the following components:

- A preamplifier to collect charge carriers from the detector.
- A high-speed ADC, often of the flash type, capable of digitizing the preamplifier output at rates up to 10 MHz, providing resolutions of up to 14 bits.
- Digital signal processing units to perform various functions such as pulse shaping, pole-zero cancellation, baseline restoration, pile-up rejection, and ballistic deficit correction.

One of the key advantages of DPP systems is the ability to employ digital filters that can emulate or surpass the performance of their analog counterparts. For example, while the best analog pulse filter is semi-Gaussian, digital filters can achieve more optimal shapes like triangular or true Gaussian, improving the signal-to-noise ratio and resolution. Digital processing allows for greater flexibility and precision in handling the signals. Adjustable parameters like rise time, fall time, and flat-top width of the digital filters can be precisely tuned to match the specific characteristics of the detector and preamplifier system. Overall, while analog system still hold relevance, the advance of digital systems in term of temperature stability and resolution, make them an increasingly attractive option for γ-ray spectrometry.

In this work, both analogical and digital electronics were employed. In both cases, a fundamental parameter is the linearity of the whole chain that must be verified, since it

is the property that ensures that the amplitude of the final signal is proportional to the amount of energy released by the photons within the detector.

The time required to process the signal is also important because when an event is detected, the system generates a "busy" signal that closes the input gate to prevent additional pulses from entering the ADC until the current pulse is fully processed. The time during which the system is unable to process new signal is referred to as dead time (DT). MCA employs live time clocks to measure the actual time the system is available to detect events, i.e. the Live Time (LT), allowing for accurate correction of the recorded data. The total length of the measurement is the Real Time, RT = LT + DT. The DT must be kept low otherwise the correction introduced by the MCA may not be sufficient and mathematical correction factors should be included (Knoll [2010]). From an electronic point of view, the reduction of the DT can be accomplished by reducing the number of spurious signals as electronic noise and other very low energy signals, that may be rejected setting the low level discriminator (LLD) in the ADC. Other than this, the shielding reduce the time required to process an high background and selecting the appropriate distance sample-detector permits to reduce the solid angle and thus the number of photons to be processed.

At the end of the whole process, the spectra can be analyzed through computer software that permits to perform energy and efficiency calibration, to determine the net area of each peak, but also to obtain a complete report analysis of the acquired spectra for routine analysis of samples whose composition is known. In this work the GammaVision software from ORTEC company was used.

Energy calibration

Within the MCA, the signal is stored in different channels according to the pulse height, which is, in principle, proportional to the energy of the incident photon. In practice, slight deviations from linearity may be possible, especially at the extremes of the energetic range. In any case, an energy calibration is required to associate an energy to each channel. Calibration sources are used, as the energy of their emission is well-known. In my work, ^{60}Co, ^{241}Am, ^{133}Ba, and ^{152}Eu radioactive sources have been employed. The nuclear properties of these radionuclides are listed in Table 3.1.

When calibrating a detector for the very first time, a gross calibration is performed using a ^{60}Co source by modifying the fine gain of the amplifier. In particular, the positions of the two main emissions of this radionuclide are positioned approximately in correspondence with channels 2352 and 2664 in order to have a ratio of keV/channel of 0.5 and to cover a range of 2 MeV with 4096 channels. A fine calibration is performed using the GammaVision software through the function:

$$E(keV) = a + b \cdot Chn + c \cdot Chn^2 \tag{3.3}$$

where Chn is the channel number. However, for all the detectors used, the quadratic term c is negligible and a linear relation is obtained over the entire range. No significant differences are present between the energy calibration of p-type and n-type HPGe detectors. For this reason, only the calibration of one of the p-type detectors of the LASA laboratory is reported in Figure 3.6.

Energy resolution

The energy resolution is directly linked to the measurement of the peak widths: narrower peak widths indicate a higher ability of the system to resolve two peaks that are

Table 3.1: Nuclear properties of the calibration sources employed in this work (data from NNDC [2023]). The uncertainties on the half-lives, the energy, and the intensity of each emission are reported in italics and refer to the last digits. Next to the decay mode is the branching ratio of each decay pathway.

Nuclide	**Decay mode**	**Half-life** [d]	$\mathbf{E}_\gamma$ [keV]	$\mathbf{I}_\gamma$ [%]
^{60}Co	β^- (100 %)	1925.23 *27*	1173.228 *3*	99.85 *3*
			1332.492 *4*	99.9826 *6*
^{133}Ba	EC (100 %)	3848.7 *12*	53.1622 *6*	2.14 *3*
			79.6142 *12*	2.65 *5*
			80.9979 *11*	32.9 *3*
			160.612 *16*	0.638 *5*
			276.3989 *12*	7.16 *5*
			302.8508 *5*	18.34 *13*
			356.0129 *7*	62.05 *19*
			383.8485 *12*	9.94 *6*
^{152}Eu	EC/β^+ (72.08 %)	4941 *7*	121.7817 *3*	28.53 *16*
	β^- (27.92 %)		244.6974 *8*	7.55 *4*
			344.2785 *12*	26.59 *20*
			411.1165 *12*	2.237 *13*
			443.9606 *16*	2.827 *14*
			778.9045 *24*	12.93 *8*
			867.380 *3*	4.23 *3*
			964.057 *5*	14.51 *7*
			1085.837 *10*	10.11 *5*
			1089.737 *5*	1.734 *11*
			1112.076 *3*	13.67 *8*
			1212.948 *11*	1.415 *8*
			1299.142 *8*	1.633 *11*
			1408.013 *3*	20.87 *9*
^{241}Am	α (100 %)	$1.5785\ 23 \cdot 10^5$	26.3446 *2*	2.27 *12*
			59.5409 *1*	35.9 *4*

close in energy. Ideally, the spectrum for a monoenergetic gamma emission would have all counts collected in a single channel. However, this is not the case in reality. Each detector has a specific response function $f(E, E')$, which is the spectrum measured by a detector for monoenergetic radiation. The response function is described by the integral:

$$S(E) = \int s(E')f(E, E')\,dE' \tag{3.4}$$

Here, $s(E')$ represents the true spectrum, and $S(E)$ is the measured spectrum. If the response function is a Dirac delta function $\delta(E-E')$, then the measured spectrum matches the true spectrum, resulting in the best possible energy resolution for the detector. In practice, the response function for a photopeak is not a Dirac delta function but rather a distribution centered at E_0, the energy of the monoenergetic radiation, with finite dispersion due to uncertainties during the detection and measurement processes. As an example, the response function of a detector to the γ-emission of ^{40}K is the spectrum in Figure 3.1.

The measure for the width of the peak used in γ-ray spectrometry is the Full Width at

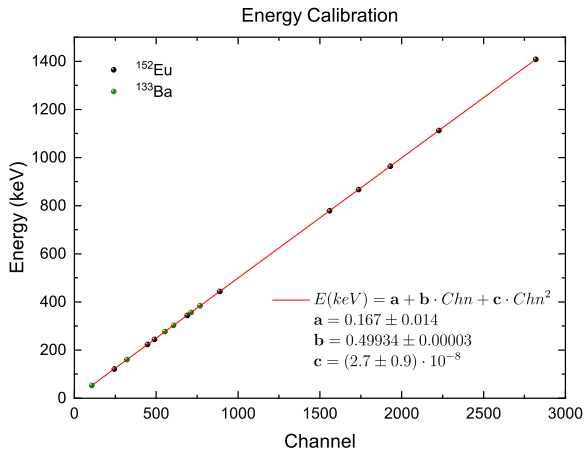

Figure 3.6: Energy Calibration of an HPGe detector using ^{133}Ba (green points) and ^{152}Eu (black points) calibration sources. The fit functions show that each channel corresponds to approximately 0.5 keV and that the contribution of the quadratic term is negligible: the energy-channel relation is linear.

Half Maximum (FWHM, here ω). Different factors contribute to the degradation of the energy resolution. Considering them independent, we have that the overall uncertainty ω is given by:

$$\omega^2 = \omega_P^2 + \omega_C^2 + \omega_E^2 \tag{3.5}$$

where ω_P is the uncertainty in the *electron-hole pairs* numbers created in the detector, ω_C is the uncertainty in the *charge collection* process, and ω_E is the uncertainty that arises due to the *electronic noise*. In principle, the physical width of the peak due to the Heisenberg uncertainty principle should also be considered, but as demonstrated in the Section 2.1.5 dedicated to γ ray emission, it is in any case lower than 1 meV. This has to be compared to the typical values of FWHM for HPGe spectrometers, which are of the order of units of keV for the 50-2000 keV energy range.

The average energy required to create a hole-electron pair in a germanium detector is $\varepsilon = 2.96$ eV. However, the energy level of the specific electron influences the energy required to promote it to the conduction band. We can assume that the process follows a quasi-Poisson statistics[2] so that the FWHM associated with the photopeak of a γ ray of energy E_γ can be estimated as:

$$\omega_P = 2.355 \cdot \sqrt{F \cdot E_\gamma \cdot \varepsilon} = 0.128 \cdot \sqrt{F \cdot E_\gamma} \tag{3.6}$$

where the factor 2.335 converts the standard deviation to the FWHM value. F is the Fano factor that accounts for the fact that the distribution is quasi-Poisson; it can range between 0.057 and 0.12 depending on the material and the charge collection process.

[2]The ionization process is not completely described by Poisson statistics since the events are not independent: locally, the ionization causes a modification of the local distribution of the electrons, influencing the probability of creation of a second electron-hole pair in the same area. Moreover, the energy shells are characterized by discrete energies, limiting the fluctuations and, consequently, the energy resolution (Leo [1994], Gilmore [2008]).

Considering $F = 0.58$, the FWHM of the photopeak at 661.67 keV due to the electron-hole pairs production is about 0.794 keV with a germanium detector. This component of the FWHM is unavoidable and impossible to reduce since it is an intrinsic property of the detector.

The charge collection process also influences the energy resolution. In particular, incomplete charge collection leads to a low-energy tail, reducing the energy resolution and making the peak not Gaussian. Several factors influence the charge collection in the preamplifier, including the presence of deep traps in the detector, insufficient shaping-time of the amplifier, or the presence of radiation damage induced by fast neutrons (Frenkel defects) that act as efficient traps in the detector. Experimental evidence suggests that the mathematical dependence of ω_C on the photon energy is linear.

Electrical noise, instead, is independent of the energy of the γ ray and may be estimated by using a pulse generator for which no charge collection and pair production is necessary. Two main sources influence the electrical noise: thermal noise due to the thermal random vibrations of electrons and shot noise caused by oscillations of the DC current due to the statistical nature of the current generation processes.

Summing up these contributions as in Equation 3.5, we obtain:

$$\omega = \sqrt{a + bE + cE^2} \tag{3.7}$$

where we recognize the constant, square root, and linear dependence on the energy of the three processes previously described. This relation may be used to fit the FWHM as a function of the energy and used in deconvolution processes to determine the expected FWHM at a given energy. An example of FHWM calibration is reported in Figure 3.7, for the same spectra used for the energy calibration of Figure 3.6.

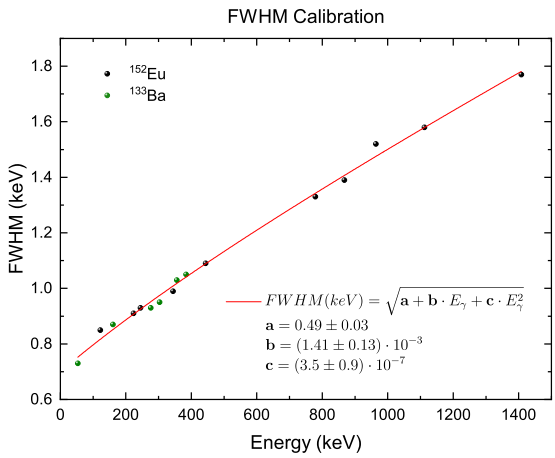

Figure 3.7: FWHM Calibration of an HPGe detector using ^{133}Ba (green points) and ^{152}Eu (black points) calibration sources. The fit parameters a, b and c are the contribute to the width of the peak of the electronic noise, the e-h pairs formation and the charge collection processes respectively.

Efficiency calibration and activity determination

The efficiency of a detector may be defined in different ways according to its intended use. Our goal is to determine the activity of an unknown source, with a specific geometry and at a fixed distance, based on the counts of photo-peaks associated with the γ ray emission of the radionuclides in the sample. In this case, the *full energy peak efficiency* ε (hereafter simply referred to as *efficiency*) must be used. This quantity relates the number of γ rays emitted by the source at a given energy to the net area of the peak at the same energy. It depends on both the energy and the geometry. For these reasons, a calibration curve as a function of energy is necessary, using mathematical functions to fit the experimental data for a known calibration source. Moreover, a new calibration is required every time the geometry changes. The efficiency is defined as:

$$\varepsilon(E_\gamma) = \frac{\text{detected photons}}{\text{emitted photons}} = \frac{\text{Net counts}}{LT \cdot A \cdot I_\gamma} \tag{3.8}$$

where Net counts is the net area of the photo-peak, LT is the live time of measurement, A is the activity of the calibration source, and I_γ is the intensity of emission of the γ ray at energy E_γ.

The mathematical relationship between energy and efficiency is empirical; there is no physical basis behind it. It generally depends on the calibration energy range, the detector type, and is at the discretion of the laboratory. In this work, two mathematical functions have been used for n-type (ε_n) and p-type (ε_p) detectors:

$$\varepsilon_n = \frac{1}{E} \sum_{i=0}^{5} a_i \cdot (\ln E)^{i-1} \tag{3.9}$$

$$\varepsilon_p = \exp\left(\sum_{i=0}^{5} a_i \cdot E^{i-1} \right) \tag{3.10}$$

Using the software OriginLab-2022b (OriginLab Corporation [2022]) the 95 % confidence band of the fit has been determined, corresponding to the 2σ uncertainty value. In this work, the $\max\left[\sigma;\ 0.03 \cdot \varepsilon\right]$ has been used as uncertainty on the efficiency.

Various phenomena related to the efficiency measurement introduce systematic errors in the activity measurements. These phenomena include differences in geometry between calibration and measurement, varying densities of the calibration source and sample, and the True Coincidence Summing (TCS) effect:

- In all studies related to this thesis, point-like calibration sources with a diameter of approximately 5 mm at distances greater than 10 cm have been employed. The geometry is conserved since our foils are irradiated with a beam of diameter less than 10 mm, and no significant error is associated with small movement of the source in the plane orthogonal to the detector distance. Additionally, when determining the cross-section, corrections for differences in source geometry are automatically performed since the charge in Equation 2.97 is obtained as the ratio between a measured cross-section and a reference cross-section.

- Due to the finite thickness of the sample, there is a non-zero probability of interaction between the emitted photons and the sample itself, reducing the number of photons reaching the detector. This probability depends on the density and composition of the sample, i.e., the mass attenuation coefficient μ/ρ. If this coefficient

is known, the activity measured A_m in a sample of mass thickness ρx can be corrected to obtain the true activity A_0 using the following relation (from Alfassi et al. [2009]):

$$A_0 = A_m \cdot \frac{t}{1 - e^{-t}} = A_m \cdot f_{att}, \quad \text{where } t = \frac{\mu}{\rho} \cdot \rho x. \tag{3.11}$$

The typical correction factors are in the range of 1.001-1.030 in the energy range between 70 keV and 1400 keV. Only in few cases of thicker targets the correction is higher than 20 %.

- True Coincidence Summing (TCS) occurs when two γ rays are emitted in sequence from a nucleus with energy levels lifetimes shorter than the resolving time of the spectrometer. The probability that both photons release their energy within the detector depends on the source-detector distance. In this scenario, the detector sees a single photon with energy equal to the sum of the two photons emitted by the source, resulting in a "sum-peak" not associated with any single gamma emission from the source. More importantly, there is a reduction in the count rates of the two real peaks, leading to an underestimation of the activity or efficiency if the source is used for detector calibration. It is well-known that some peaks of ^{152}Eu are affected by TCS (E_γ= 244.6974 keV, 344.2785 keV, 443.9606 keV), which is why they are sometimes excluded, especially if the source-detector distance is short. This effect is illustrated in Figure 3.9. Mathematical corrections based on Monte Carlo N-Particle (MCNP) Transport Code (see Agarwal et al. [2011]) or based on experimentally determined correction factors (see Debertin and Schötzig [1979]) are available if necessary, but they have not been employed in this work since γ rays not affected by TCS were used.

The nuclear data of the calibration sources are reported in Table 3.1, the activity of each source is reported in Table 3.2. All sources are provided by CercaLEA (France).

Table 3.2: Calibration sources used and their activities. All sources are provided by CercaLEA (France).

Source	**Laboratory**	**Activity** [kBq]	**Certification date**
^{152}Eu	LASA	41.1 *8*	15 October 1993
^{133}Ba	LASA	37.7 *8*	13 April 2004
^{152}Eu	GIP ARRONAX	3.44 *7*	26 November 2008
^{241}Am	GIP ARRONAX	42.8 *8*	9 December 2021

Two examples of calibration in the range between 50-1408 keV for n-type and p-type detectors are presented in Figure 3.8 and Figure 3.9. Notable differences in the shapes of the efficiency curves are observed: both curves exhibit a knee and a linear behavior in the log-log scale at high energies, but at lower energies, the n-type detector shows a plateau, whereas the efficiency of the p-type detector rapidly decreases. Note that for the calibration of the n-type detector, the peaks that present the TCS phenomenon have not been excluded, as the distance is sufficient to reduce the probability of detecting two photons simultaneously.

Neither of the functions in Equations 3.9 and 3.10 can accurately describe the efficiency data down to the 26.3 keV γ ray of ^{241}Am. However, as will be explained later, there is only one emission of ^{161}Tb at an energy lower than 50 keV, specifically at E_γ = 25.7 keV with I_γ = 23.2 %, for which no fitting is necessary as it is very close to the low

energy emission of ^{241}Am. For an n-type detector, no significant variation in efficiency is expected.

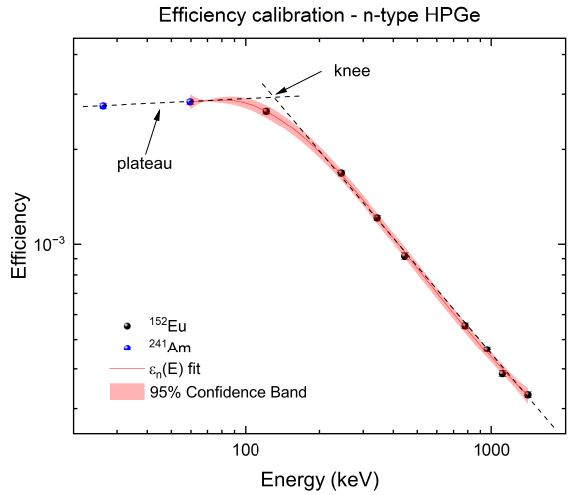

Figure 3.8: Efficiency Calibration of a n-type HPGe detector using ^{241}Am (blue points) and ^{152}Eu (black points) calibration sources at 19 cm distance from the detector. The dashed lines highlight the behavior of the efficiency curve for this type of HPGe detector: a knee around 120 keV separates the linear decrease of the efficiency in log-log scale at high energy and the plateau region at lower energy. The red line is the fit curve obtained using Equation 3.9, while the pink band is the confidence band of the fit.

Once the efficiency is known, it is possible to relate the net counts of the photo-peak to the activity of the radionuclide by inverting Equation 3.8:

$$A = \frac{\text{Net Counts}}{LT \cdot \varepsilon \cdot I_\gamma} \cdot f_{att} \tag{3.12}$$

Note that the factor D(RT), defined in Equation 2.81 to account for the decay of the radionuclide during the measurement, always has to be multiplied, especially if the condition of RT $\ll$ $T_{1/2}$ is not verified.

3.1.2 Alpha Spectrometry

Alpha spectrometry is a nuclear detection technique employed for identifying and quantifying alpha-emitting isotopes by measuring their alpha spectra. This method primarily uses semiconductor detectors, especially silicon-based ones.

Alpha particles emitted by decaying nuclei have energies ranging from 4 to 9 MeV (see Section 2.1.4), and are efficiently absorbed by thin layers of solid materials like silicon. This ensures high detection efficiency due to the very low escape probability, compared to photons, with limitations primarily due to geometric factors (solid angle).

The interaction of ionizing radiation with silicon detectors generates a high number of electron-hole pairs per unit energy (ε = 3.62 eV/pair), resulting in small statistical fluctuations and thus excellent energy resolution—typically a few tens of keV, which is suitable for the energy range of alpha particles.

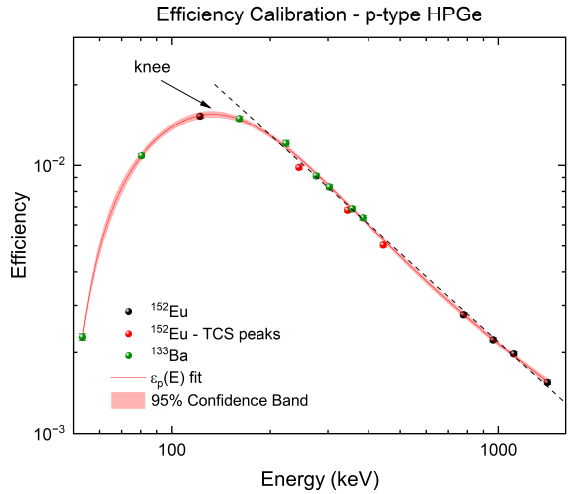

Figure 3.9: Efficiency Calibration of a p-type HPGe detector using ^{133}Ba (green points) and ^{152}Eu (black points) calibration sources at 10 cm distance from the detector. The dashed line highlights the typical behavior of the efficiency curve for a p-type HPGe detector: a knee separates the linear decrease of the efficiency in log-log scale at high energy and a drastic decrease of the efficiency at lower energy. The red line is the fit curve obtained using Equation 3.10, while the pink band is the confidence band of the fit. Red points of the ^{152}Eu are excluded from the fitting of the efficiency as they are affected by the TCS phenomenon.

Operating Principle and Experimental Setup

The silicon charged-particle detector functions as a large semiconductor diode with a thin entrance window to minimize energy loss. A reverse bias is applied to the diode to create a depletion region free of charge carriers, which is crucial for detecting incoming alpha particles with minimal noise (Knoll [2010]). No cooling is necessary when using silicon due to its higher energy gap between the conduction and valence bands (E_g = 1.106 eV at room temperature (Gilmore [2008])). When an alpha particle enters the detector, it ionizes the silicon atoms, creating electron-hole pairs proportional to the particle's energy. These charges are collected by electrodes and converted into an electrical pulse by the preamplifier.

The experimental setup for alpha spectrometry, illustrated in Figure 3.10, is similar to the HPGe γ-detection system, both being semiconductor-based. The components include:

- **Detector and Preamplifier**: A silicon charged-particle detector connected to a preamplifier to process the initial signal.
- **Amplifier**: The signal from the preamplifier is further amplified to improve the signal-to-noise ratio.
- **Multichannel Analyzer (MCA)**: The amplified signal is fed into an MCA, which sorts the pulses into a histogram based on their heights, representing the alpha spectrum.

- **Vacuum System**: A vacuum chamber is used to minimize interactions between alpha particles and air molecules, which could lead to energy loss and broadening of spectral lines.

Energy and efficiency calibration using certified sources is required. However, the efficiency of a silicon detector for alpha spectrometry is independent on the energy in the 4-9 MeV range and depends only on the voltage and the distance of the source from the detectors.

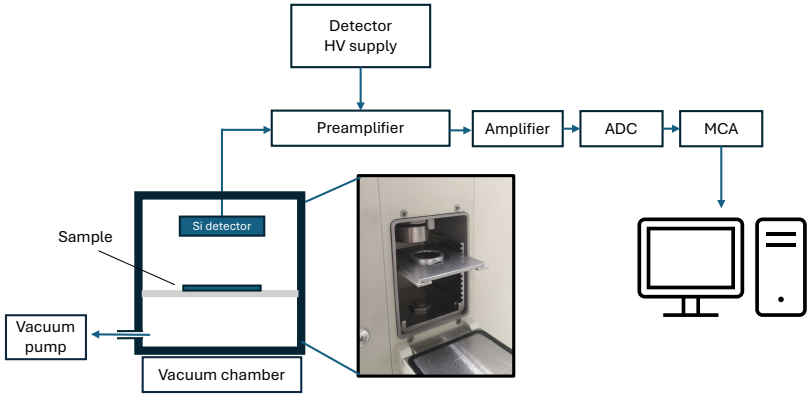

Figure 3.10: Experimental setup of a Si-based solid state alpha spectrometer. The actual vacuum chamber with the detector and the sample are depicted.

The calibration of the detector used at GIP ARRONAX is shown in Figure 3.11. An example of a ^{241}Am alpha spectrum is illustrated in Figure 3.12.

It is essential that the sample is very thin to avoid attenuation and straggling of the alpha particles emitted by the source. Often, radiochemical processing of the sample is required.

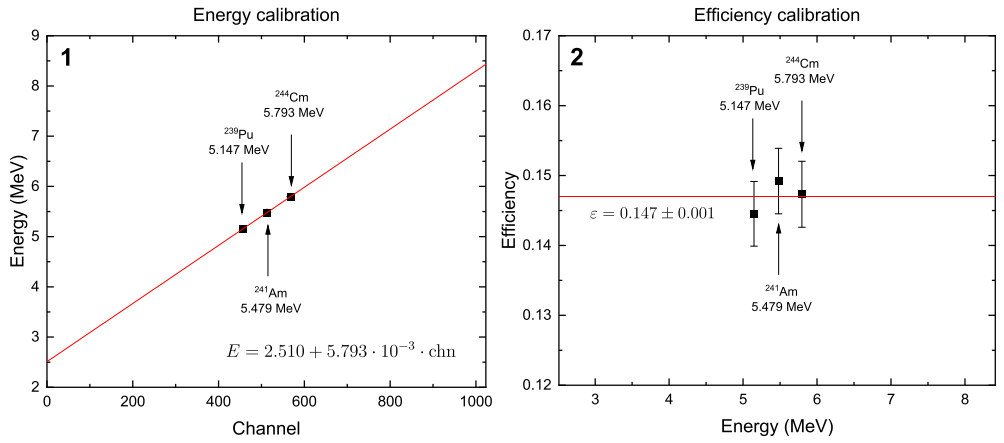

Figure 3.11: Energy (left) and efficiency (right) calibration of a Si-based solid state alpha spectrometer. (**1**) A linear fit (red line) determines the energy channel relation. (**2**) A constant fit (red line) determines the average efficiency. The alpha sources used are indicated. In the case of ^{241}Am, the average energy of the alpha particles emitted is reported.

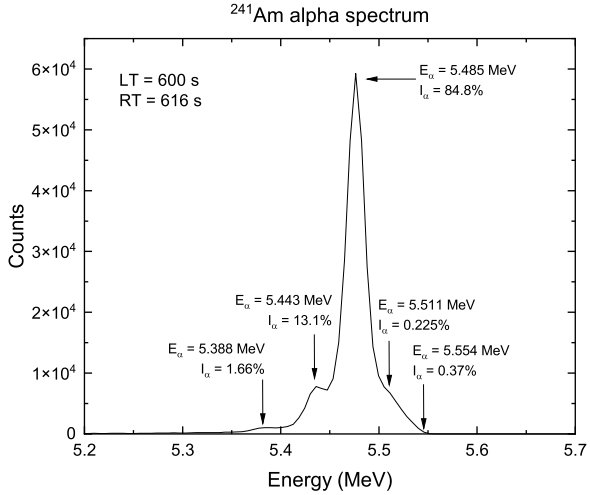

Figure 3.12: Example of ^{241}Am alpha spectrum.

3.2 Stacked Foils Technique

From a physics perspective, the goal of this work is to determine the excitation functions, i.e., the cross-sections as a function of the beam energy, for various nuclear reactions leading to the production of theranostic radioisotopes of terbium. Ideally, measuring the XS would require performing numerous irradiations at different energies using different thin targets, and determining the activity of each radionuclide produced to be used in Equation 2.79. This approach, however, is both expensive and time-consuming.

A more efficient approach is the *stacked foils technique*. In a single irradiation, a stack of different thin foils is irradiated simultaneously. The energy of the particles impinging on each foil is reduced due to the energy degradation caused by the preceding foils, as described in Section 2.2.1. The stack is not composed solely of the target of interest, which would be both costly and inefficient. Instead, different types of foils, each serving a specific function, are included:

- *Target foils*: These are the foils of interest for the reaction (e.g., gadolinium foils for the nuclear reaction ^{nat}Gd(α,x)). Essential qualities of the target foils include high purity (greater than 99 %) and appropriate thickness. They should be thin enough to limit the beam energy loss to within 5 %, ensuring that the cross-section can be approximated as a constant value within the foil due to minimal energy variation.

- *Catcher foils*: When a nuclear reaction occurs, the excess energy is shared as kinetic energy between the reaction products. The residual energy for the remaining nucleus is generally low since it has a much higher mass than the emitted particles, as discussed in Section 2.3. However, a significant number of nuclei may recoil from the outer layer of the target. This recoil can be up to 20 % for very thin and light target nuclei irradiated with high-energy alpha particles. It is crucial to collect these recoiling nuclei on a second foil, referred to as *catcher*. The catcher must be chemically distinct from the target to differentiate the radionuclides produced on the target from those produced on the catcher. Additionally, the catcher should have a low activation probability, especially for radionuclides with medium/long half-lives and high-energy emissions, to reduce the Compton background and avoid increased dead time during measurement. For the same reason, the catcher should not be too thick.

- *Degrader foils*: To achieve the desired energy for measuring the cross-section on the foils within the stack, degrader foils (typically aluminum) are added. The thickness of these foils is selected based on the method explained in Section 2.2.1.

- *Monitor foils*: These foils verify the correctness of the beam energy calculation and determine the integrated charge by comparing the results of specific "monitor" nuclear reactions with those recommended by the IAEA. This aspect will be discussed in more detail in the section on charge determination. Common monitor foil materials include Al, Ti, and Cu. If an Al monitor is used, a different catcher (e.g., Ti) is employed.

Once the stack is designed to achieve the desired energy on each target, it is physically assembled by stacking the foils in a specially designed sample holder. This holder is designed to accommodate square foils with dimensions of (2.5×2.5) cm^2 and to be positioned in the target station of the GIP ARRONAX cyclotron (see Section 3.4.2). Figure 3.13 provides an example stack from an experiment measuring the nuclear cross-section

of the ^{nat}Gd(α,x) reactions. The specific stack design for each experiment will be detailed in the corresponding section.

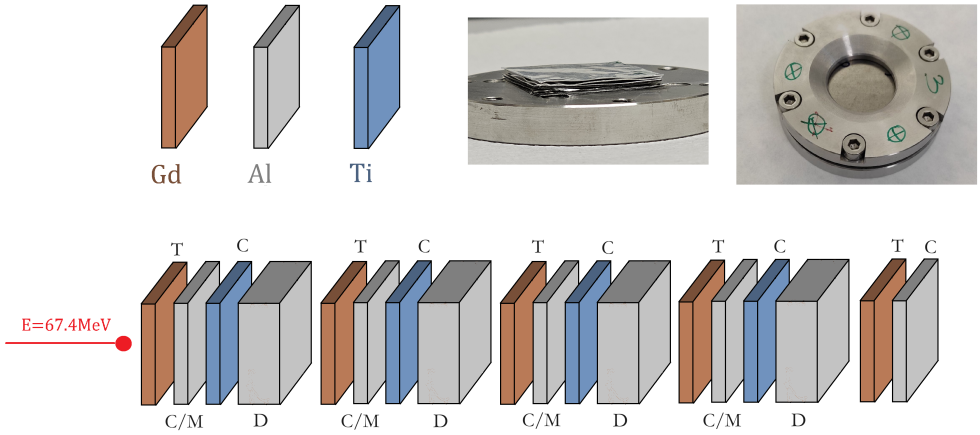

Figure 3.13: Example of stack design and realization. The color refer to the element, brown for Gd, gray for Al and blue for Ti. The letter on the foils follow the legend: T for target, C for catcher, M for monitor and D for degrader. In this particular case Al served both as monitor and for catcher of the Gd foils. The two pictures show the stack in the holder open and closed.

In each experiment, 4 to 5 targets are irradiated. While there is no inherent limit to the number of foils that can be irradiated, there are advantages to limiting their number:

- If the cyclotron beam exit energy is adjustable, it is preferable to conduct the measurement in multiple sessions. This approach reduces the uncertainty due to energy straggling by selecting a different energy for each session, thereby fully covering the desired energy range in 4-5 experiments.
- Even with a fixed beam energy (e.g., the α beam energy of the GIP ARRONAX is set at 67.4 MeV), performing multiple experiments is beneficial. With a limited number of detectors, fewer samples allow more time for measuring each foil. Additionally, if an issue arises during irradiation, the loss of material is minimized.

Special attention is given to the energy distribution of the targets: to ensure continuity and consistency between different stacks, the first foil of a new stack is irradiated at an energy midpoint between the last two targets of the previous stack.

3.2.1 Foils characterization

In almost all cases, metal thin foils were used to determine the cross-sections of interest. The only exception is the europium foils, which were produced in collaboration with the Politecnico di Milano from Eu_2O_3 nanopowder. The production process and characterization of these foils will be described in the section on the ^{nat}Eu(α, x) reactions. All other foils were purchased from GoodFellow Corporation (Huntingdon, UK) with a purity greater than 99 %.

Characterizing the foils involves determining the mass thickness $\rho x = \frac{m}{S}$, which requires measuring the mass (m) and area (S) of the foil, and verifying the thickness

uniformity. Typically, the foils are purchased in large sizes (10×10 cm^2 or (5×5) cm^2), and the following procedure is performed:

1. The uniformity of the foil is verified using an analogical thickness gauge with a sensitivity of 0.1 µm (Figure 3.14). A thickness map is created, as shown in Figure 3.15. If the foil is uniform, the next steps are performed; otherwise, the foil is cut into smaller pieces that meet the uniformity condition before proceeding.

Figure 3.14: Analogical thickness gauge.

2. The area of the foils can be determined in two ways. The first method involves assuming that the foil is a rectangle. To find the area, the lengths of the opposite sides are measured three times each using a caliper with a precision of 10^{-5} m. The average length of each pair of opposite sides is then calculated and used to determine the area. The second method involves scanning the foils using a 1200 dpi scanner and determining the area using a MATLAB script that counts the number of pixels in the image and converts it into an area. The code is as follows:

```
% read in the image
img = imread(['image_path']);

% convert to binary image
bw_img = im2bw(img);

% define the dimensions of the picture
[height, width, channels] = size(img);

% number of pixels
black_area = height*width - bwarea(bw_img);

% conversion factor (cm^2/pixel)
```

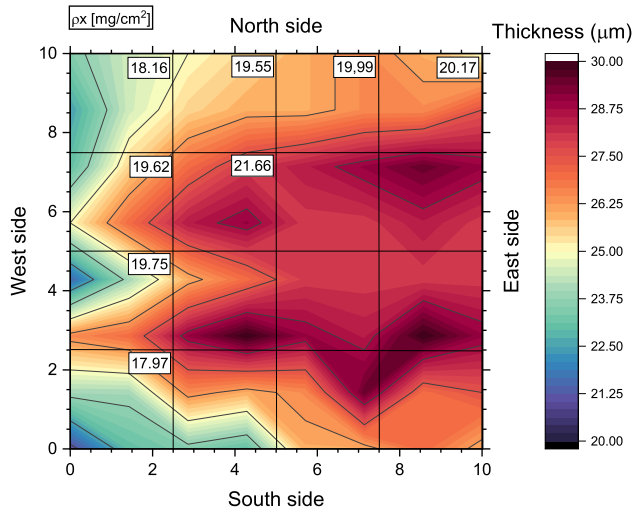

Figure 3.15: Example thickness uniformity verification. The Gd foil analyzed here showed a lack of uniformity and a gradient due to the fabrication process is clearly visible. To reduce thickness variability, the foil was cut into 16 smaller squares with acceptable homogeneity (less than 5 % in the central region). For some smaller foils represented in this picture, the mass thickness was determined as explained in the text: the results correspond to the measurements performed with the gauge (color), with thicker regions having higher mass thickness (label).

```
calib_factor = (2.54/1200)^2;

% physical area
phys_area = black_area * calib_factor;

% print area
disp(phys_area);
```

The uncertainty for both methods is set to 2 % to account for potential systematic errors in using the caliper or distortions in the scanned image.

3. The foils are washed with ethanol to remove impurities and dust, with water to remove ethanol, and with acetone to remove organic residues and accelerate water evaporation.

4. The mass is measured using a scale with a sensitivity of 10^{-5} g, three times, to evaluate the measurement fluctuations.

5. The foils are cut into (2.5 $\times$ 2.5) cm^2 pieces, re-washed, and labeled with a unique code to distinguish each component of the stack.

A precise determination of the thickness is paramount to determine correctly the loss of energy of the beam within the stack.

3.2.2 Charge determination

To measure the total charge impinging on the stack different methods are available, with two of them being more diffused. The fist one is the Faraday cup that operate by capturing the beam with a metal electrode (the collector). The rate of charge accumulation on the electrode is then measured using a sensitive ammeter. However, the emission of secondary charges from the electrode may cause erroneous readings of the beam current. To mitigate this issue, the collector is typically designed as a deep, cup-shaped electrode with a high length-to-aperture ratio. Additionally, electric and sometimes magnetic fields are applied to minimize the escape of secondary charges (Strehl [2006]). The second one consists into perform an indirect measure of the charge obtained as ratio between a measured cross-section and a reference value, i.e. the *recommended monitor reactions*. This technique, employed in this work, is particularly useful because it permits to simultaneously determine the charge and verify the correctness of the beam energy. Accurate knowledge of these parameters is critical in experiments of reaction cross-sections measurement, especially for the production of medical isotopes, even small deviations in beam characteristics can lead to significant errors in the quantity and purity of the produced radionuclides.

A work-group of the International Atomic Energy Agency (IAEA) selected a number of reactions induced by protons, deuterons ^{3}He and α particles on common and cheap materials such as Al, Ti, Ni or Cu whose cross-section have been measured multiple time by different laboratories (Hermanne et al. [2018]). Each measurement has been evaluated and only the most reliable have been selected. The key techniques used in the evaluation of this data is the Padé approximation. It is a mathematical method that represents a function as the ratio of two polynomials. This approach is particularly effective in fitting nuclear reaction data because it can accurately model the complex, non-linear behaviors often observed in these reactions. The process involves iteratively adjusting the parameters of the polynomials to minimize the differences between the experimental data and the fitted function, typically quantified using the chi-squared (χ^2) statistic. A well-fitted Padé approximation provides a smooth and continuous representation of the cross-section data, which can be used for interpolation of the cross-sections (Hermanne et al. [2018]). The database is continuously verified and extended (Tárkányi et al. [2024]) to enlarge the range of usability of the technique and to provide always more accurate results. The list of monitor reactions used in this work are reported in Table 3.3.

Practically the charge is determined as follows. A number of monitor foils are inserted within the stack. The activity produced on each foil is determined using the γ emissions listed in Table 3.3. A fictitious cross-section σ^* is then determined by using Equation 2.79 and by setting Q^* = 1 C as charge. The ratio between $\sigma^*(E)$ and the recommended value of cross-section $\sigma^{IAEA}(E)$ provide the numerical value of the charge in Coulomb:

$$Q(C) = \frac{\sigma^*(E)}{\sigma^{IAEA}(E)} \tag{3.13}$$

Note that Q should not depend on the monitor reaction selected and the energy of the beam. If different values are obtained, and all the trivial errors are excluded, it may suggest deviation in the nominal value of the energy of the beam or a beam divergence that cause loss of charge if the beam is larger than the foil. The latter problem may be verified by performing measurements of autoradiography of the foils as described in the next paragraph. In case of energy shift, the advantage of using monitor reactions over the use of Faraday cups, is that it is possible to adjust the initial energy value (by a reasonable quantity) until good agreement is obtained for all the monitor foils.

Table 3.3: Table of monitor reactions recommended by IAEA (from Hermanne et al. [2018]) and nuclear properties of the produced radionuclide (from NNDC [2023]). The uncertainties on the half-lives, the energy, and the intensity of each emission are reported in italics and refer to the last digits.

Reaction	$T_{1/2}$	E_γ [keV]	I_γ [%]	Useful Range [MeV]
^{27}Al (p, x) ^{24}Na	14.956 *3* h	1368.625 *5*	99.994 *2*	30 - 100
^{nat}Ti (p, xn) ^{48}V	15.974 *3* d	983.525 *4*	99.98 *4*	5 - 100
		1312.105 *6*	98.2 *3*	
^{nat}Ti (p, x) ^{46}Sc	83.79 *4* d	889.277 *3*	99.984 *1*	20 - 80
		1120.545 *4*	99.987 *1*	
^{27}Al (d, x) ^{24}Na	14.956 *3* h	1368.625 *5*	99.994 *2*	15 - 90
^{nat}Ti (d, xn) ^{48}V	15.974 *3* d	983.525 *4*	99.98 *4*	5 - 50
		1312.105 *6*	98.2 *3*	
^{nat}Ti (d, x) ^{46}Sc	83.79 *4* d	889.277 *3*	99.984 *1*	5 - 75
		1120.545 *4*	99.987 *1*	
^{27}Al (α, x) ^{24}Na	14.956 *3* h	1368.625 *5*	99.994 *2*	40 - 160
^{nat}Ti (α, x) ^{51}Cr	27.704 *3* d	320.0824 *4*	9.91 *1*	8 - 45
^{nat}Cu (α, x) ^{66}Ga	9.49 *3* h	833.532 *2*	5.9 *3*	10 - 60
		1039.220 *3*	37 *2*	
^{nat}Cu (α, x) ^{67}Ga	3.2617 *5* d	184.576 *10*	21.41 *1*	10 - 45
		300.217 *10*	16.64 *12*	
^{nat}Cu (α, x) ^{65}Zn	243.93 *9* d	1115.539 *2*	50.04 *10*	10 - 45

The main disadvantage of using monitor reactions is that there is no indication about the stability of the beam current during the irradiation. To overcome this problem, a beam dump may be positioned after the stack, properly connected to a charge integrator to measure the current of the beam and verify its stability. A beam dump cannot be used to determine the precise value of the charge since losses are possible.

3.2.3 Autoradiography: the Beam Profile

When the beam is set and optimized by the cyclotron operators, the shape of the beam can be observed in real-time via a webcam. This webcam captures the radioluminescence emitted by an alumina (aluminum oxide) disc positioned between the beam exit and the beam dump. However, during the irradiation of the stack, this information is lost, and any potential divergence of the beam cannot be diagnosed online.

Autoradiography is a radiation detection technique that allows for the reconstruction of the 2D distribution of radioactivity on a sample. It can be used to indirectly reconstruct the "integrated" beam shape, as the concentration of activity is proportional to the intensity of the beam.

The Cyclone®Plus storage phosphor system (by PerkinElmer) has been used for this purpose (see Figure 3.16). It is composed of a passive detector and a readout system:

- The detector is a reusable phosphor screen that has on one side a photostimulable phosphor plate (PSP) made of a thin layer of BaFBr:Eu^{2+} crystals. These crystals have the ability to store and subsequently release energy as light upon stimulation. The presence of the Eu dopant in the BaFBr crystal is crucial as it substitutes Br in the crystal lattice, producing "F-centers" (also known as color centers) that act as efficient traps for electrons, allowing the information on the spatial ionization

distribution to be stored for a long time (up to weeks). Furthermore, Eu^{2+} acts as a luminescent center; its interaction with ionizing radiation reduces it to Eu^{3+}, promoting its electron to the conduction band where it is eventually trapped in the F-centers (Rowlands [2002], Bushberg et al. [2012]).

- The readout system consists of a rotating carousel drum around which the screen is wrapped, and a laser scanner that moves linearly while the drum rotates to scan the entire screen. The electrons in the F-centers are de-trapped by a well-focused red laser beam (λ = 633 nm) with a diameter of 50 µm, which provides very good spatial resolution. The recombination of the electrons and holes at the luminescent centers results in the emission of visible light. The wavelength of this emitted light is characteristic of the Eu^{2+} ion and is typically in the blue region of the spectrum ($\lambda \simeq 390$ nm). This signal is converted and amplified by a photomultiplier tube (PMT) and analyzed to reconstruct the image using the PerkinElmer OptiQuant™software.

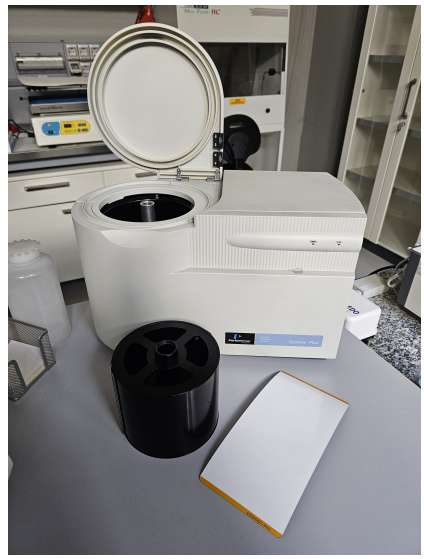

Figure 3.16: Cyclone®Plus storage phosphor system. The phosphor screen with th white PSP layes is shown, alongside with the carousel drum.

The PSP can be erased and reused by exposing it to white light to empty almost all the F-centers. It is important that the light is equipped with a UV filter to avoid extra charging of the foils.

As an example, the beam profile of the four gadolinium targets irradiated with alpha particles is shown in Figure 3.17. The results of the acquisition are displayed, and a graphical analysis is carried out in Figure 3.18. The transversal dimensions of the beam do not change significantly with depth within the stack. The non-uniformity in the x-y dimensions is not relevant for the scope of this work, where the important objective is to collect the entire beam within the dimensions of the target and to have almost the same dimension of the source when performing the γ-ray spectrometry measurements.

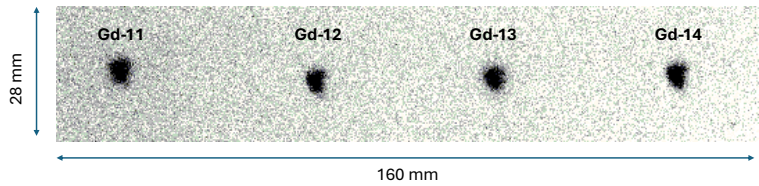

Figure 3.17: Example of image acquired with Cyclone®Plus storage phosphor system. Four Gd targets from the same stacks were positioned on the PSP for 3 minutes. The image has been acquired with a resolution of 300dpi.

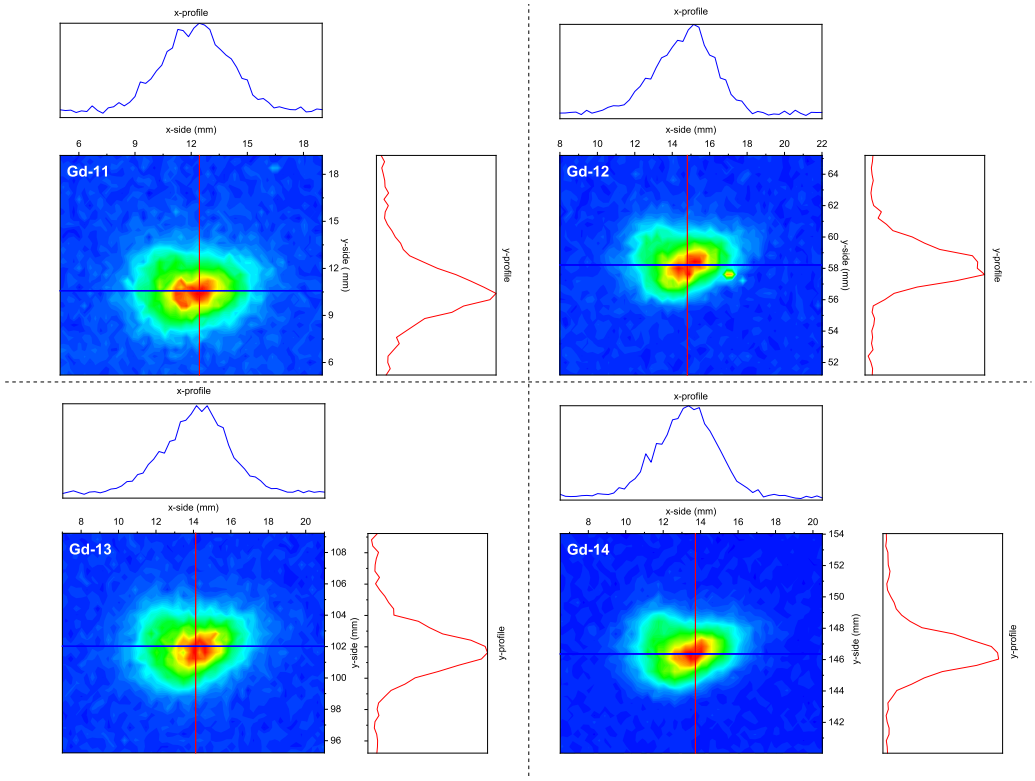

Figure 3.18: Example of graphical elaboration of an image acquired with Cyclone®Plus storage phosphor system. The signal from Figure 3.17 has been integrated in bigger square pixel of bout 24 mm^2 area and plotted as contour plot with the two transversal profile graphed on the upper and right side. The higher area of Gd-11 is probably due to the higher amount of activity.

3.3 ICP-OES

Inductively Coupled Plasma - Optical Emission Spectroscopy (ICP-OES) is a highly effective analytical technique that allows the simultaneous identification and quantification of numerous elements in liquid acid solutions, achieving detection limits down to a few parts per billion (ppb) and covering a broad linear detection range of 4 to 6 orders of magnitude, depending on the instrument (Hou et al. [2016]). The detection in ICP-OES is based on analyzing the optical emissions characteristic of elements when excited by an inductively coupled plasma (Khan et al. [2022]).

A schematic representation of an ICP-OES system is shown in Figure 3.19, while the ICP-OES (Thermo Scientific iCAP 6000 Series) of GIP ARRONAX is shown in Figure 3.20. In this setup, the aqueous sample is collected using a peristaltic pump, nebulized in a spray chamber, and injected into the ICP torch where an argon plasma is generated by a radiofrequency (RF) field. The emitted light is collected, resolved into its component wavelengths, and detected by a charge-coupled device (CCD). The emission spectrum is then analyzed using specialized software. The components of this system are detailed below.

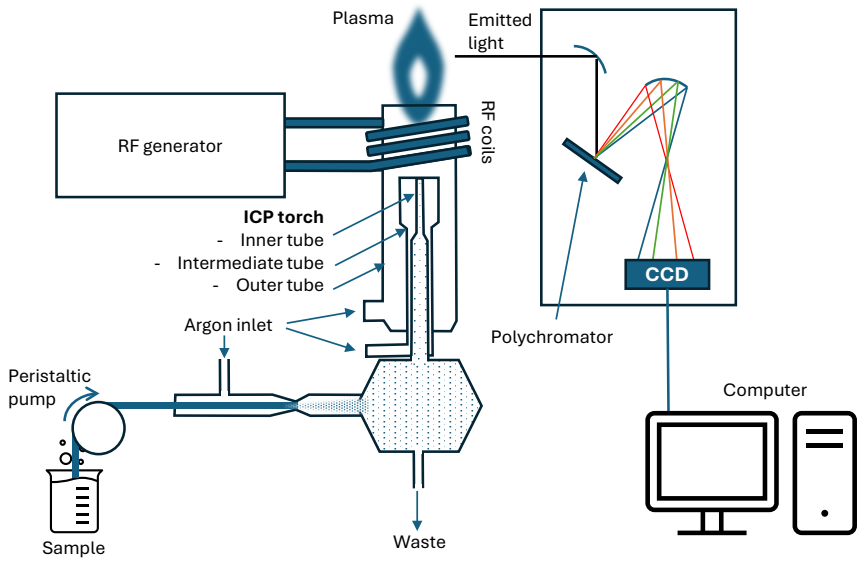

Figure 3.19: Schematic representation of an ICP-OES instrument (not in scale).

Two types of *nebulizers* are commonly used: pneumatic nebulizers, which utilize a high-speed argon flow to create a low-pressure region at the sample capillary for vaporization, and ultrasonic nebulizers, which generate an aerosol using an oscillating piezoelectric transducer. The pneumatic nebulizer, utilized in this work, is preferred for its stability, convenience, and simplicity, despite its low efficiency, as more than 95 % of the sample is typically discarded as waste.

The *spray chamber* connects the nebulizer to the plasma torch. Made of quartz to resist corrosion, the spray chamber serves two main purposes: it ensures a continuous aerosol flow, smoothing out the pulsations from the peristaltic pump, and it allows only droplets of a few micrometers in diameter to pass through, with the remainder drained as waste.

The *ICP torch* consists of three concentric silica tubes: the outer tube, the intermediate tube, and the inner tube, through which argon gas flows at different rates. The outer tube supplies the plasma gas and prevents the torch from melting. The optional intermediate tube provides auxiliary gas to dilute the sample, and the inner tube delivers the nebulizer gas along with the sample aerosol. The RF generator supplies power to the copper *RF coil* wrapped around the top of the outer tube, typically cooled by water. A Tesla coil initiates the ionization events within the torch, creating electrons and ions that interact with the oscillating magnetic field induced by the RF coils and cause cascade ionization, sustaining the plasma at temperatures up to 10^4 K .

Upon interaction with the plasma, the aerosol undergoes desolvation (solvent evaporation), vaporization (decomposition into gaseous molecules), and atomization (breakdown into atoms). These atoms are then excited/ionized, and their subsequent relaxation produces the optical signals to be analyzed. The most common configuration for the torch is vertical, with emitted light observed from the side (radial configuration) to minimize the path length through the plasma and reduce spectral interferences. Other configurations are available depending on the application (Hou et al. [2016]).

The emitted light from the plasma is collected using lenses or mirrors and focused onto the entrance slit of a monochromator or polychromator. The monochromator isolates specific wavelengths for sequential analysis, while the polychromator allows simultaneous multi-element detection.

Photomultiplier tubes (PMTs) are sometimes used for high-sensitivity, single-wavelength detection. However, array detectors, such as charge-coupled devices (CCDs), are more common because they enable simultaneous detection of multiple wavelengths, enhancing throughput and efficiency. Indeed, ICP-OES systems with array detectors can detect up to 70 elements simultaneously.

An automatic sampling system can be integrated into the ICP-OES setup to facilitate the analysis of multiple samples without continuous supervision.

Unlike γ-ray spectrometry, ICP-OES requires calibration for each element and each selected wavelength to be measured. Calibration must be repeated every time the plasma is turned off. Certified calibration standards and solutions at different concentrations of all elements to be measured are prepared to cover the desired measurement range. Attention must be given to potential wavelength overlaps of different elements in the sample. Analyzing more than one wavelength per element is recommended to increase result confidence and check for possible inteference.

Practical considerations for using ICP-OES to analyze rare earth elements (Dy, Gd, Tb) are discussed in Chapter 6.

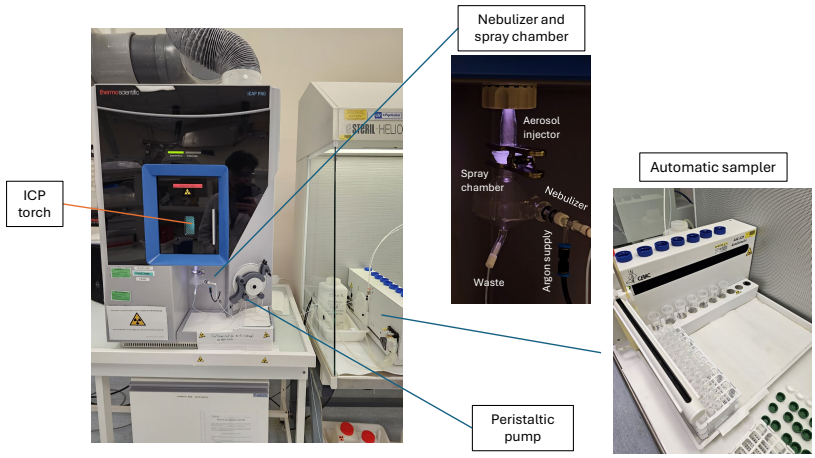

Figure 3.20: ICP-OES instrument of GIP ARRONAX. Details of the automatic sampler and of the nebulizer are shown.

3.4 Description of the facilities

3.4.1 LASA laboratory

Located in Segrate, near Milan, the LASA (Laboratory for Accelerators and Applied Superconductivity) is a laboratory of the University of Milan and shared with the Section of Milan of Italian National Institute of Nuclear Physics (INFN). It has been a center of international excellence in advanced particle accelerator technologies for nearly thirty years.

As its name suggests, the LASA laboratory focuses on studying and developing innovative acceleration schemes and advanced superconductivity applications for accelerators and other physics sectors. Founded on the vision of Prof. Francesco Resmini (1938-1984), LASA developed the first superconducting cyclotron in Europe and the third in the world. Since 1994, this cyclotron has been active at INFN's Laboratori Nazionali del Sud, contributing to research and significant medical applications.

By developing advanced technologies for superconductivity, cryogenics, and high-intensity static and radiofrequency electromagnetic fields, LASA has cultivated unique expertise that supports innovative technologies for major international particle physics projects. Activities since the early 1990s in accelerator physics and applied cryogenics for both magnets and RF cavities have established LASA's unique expertise, which INFN supports in major international particle physics projects.

Since the beginning of the 1970s, a large range of high specific activity radionuclides have been produced at the former Cyclotron Laboratory of the UNIMI. Several nuclear data for radionuclide production, measured at LASA Laboratory, are presently recommended by the Nuclear Data Section of IAEA). Nuclear activations have been carried out at the cyclotron of JRC-Ispra of EC (Scanditronix MC40, Uppsala, Sweden), as well as at the TRIGA MARK II (General Atomic, USA) nuclear reactor of Pavia, and more recently at GIP ARRONAX.

Two laboratories of LASA have been exploited during this thesis: physical measurement laboratory and radiochemistry laboratory.

Physical measurement laboratory The physical measurement laboratory is shown in Figure 3.21.

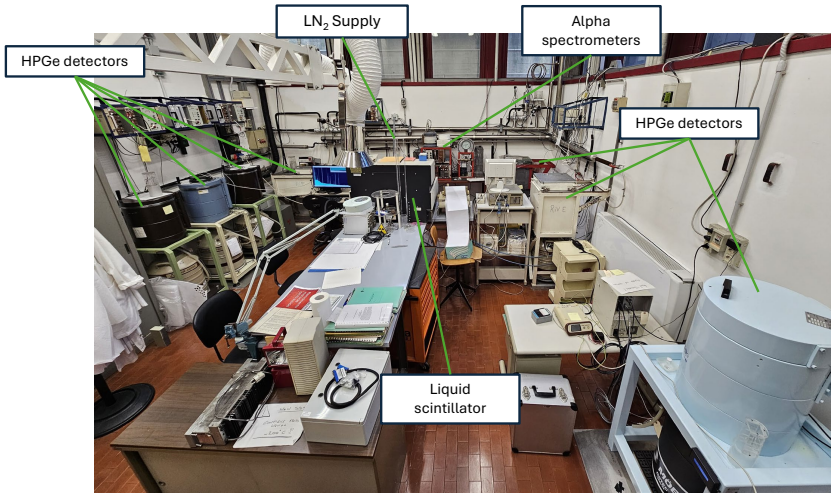

Figure 3.21: Physical measurement laboratory of LASA.

High-resolution γ-ray spectrometry is performed by 6 coaxial p-type HPGe detectors, with the following typical characteristics: intrinsic efficiency of 15 % (EG&G, USA), with a peak to Compton ratio of 30:1 at 1332.50 keV, FWHM 1.9 keV (^{60}Co point source). A DSPEC Pro Digital Signal Processing Gamma Ray Spectrometer is also available (EG&G, USA). Gamma spectra in the energy range up to 2000 keV are acquired and analyzed by advanced s/w packages. The efficiency data, obtained by decay corrected certified point source of ^{152}Eu and ^{133}Ba (2 %, Cerca LEA, France) are fitted by Gamma Vision, or by using OriginPro OriginLab Corporation [2022]. An example of detector is reported in Figure 3.22

At LASA laboratory β spectrometry in liquid samples can be performed using two detection systems (Groppi et al. [2005]):

- Liquid Scintillation Counter (Beckman, mod. LS5000TD, USA) with three energy window capability, random coincidence monitor and Horrocks Number quenching correction method
- A high-resolution liquid scintillation portable spectrometer with α/β pulse shape analysis (PSA) discriminator (Hidex, Finland, mod. Triathler).

α-spectrometry can be performed in liquid samples with the high-resolution liquid scintillation portable spectrometer. In a surface-like sample this can be achieved using a Si surface barrier detector (EG&G, Ortec, 600 mm^2), with resolution of 27 keV (FWHM). The detector is calibrated with certified sources of ^{241}Am and ^{233}U (2 %, Cerca LEA, France) (Groppi et al. [2009]).

Radiochemistry laboratory A radiochemistry laboratory is available at LASA where it is possible to manipulate short/medium-lived radionuclides and of medium activity, to perform radiochemical separation for the determination of the radionuclidic purity.

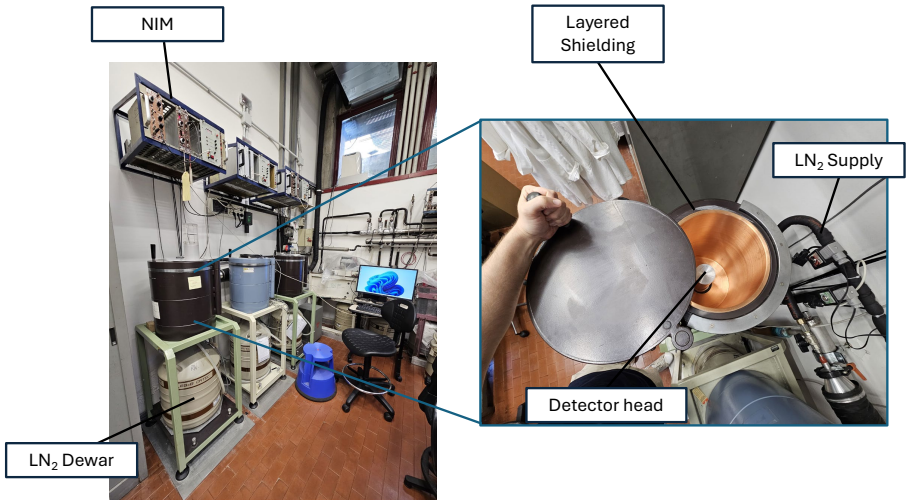

Figure 3.22: Picture of a HPGe detector of LASA laboratory. The element discussed in Section 3.1.1 are here illustrated.

Two different room in low pressure gradient conditions are available for cold and hot experiments. The room for the hot experiments is shown in Figure 3.23.

3.4.2 GIP ARRONAX

The GIP ARRONAX[3] is a "Groupement d'Intérêt Public" (Public Interest Group), a collaborative partnership that includes universities, research centers, hospitals, the Ministry of Research, and the Pays de la Loire Region. Located in Saint-Herblain (Nantes, France), its activities are centered around the Arronax cyclotron. The facility includes laboratories for radiochemistry, metrology, and shielded hot cells. It focuses on producing radionuclides, primarily for medical applications at both clinical and preclinical stages. Additionally, it conducts studies on radiolysis, radiobiology, physics, particle detector and the radiation resistance of materials.

The characteristics of the cyclotron, the experimental hall for cross-section measurements and the nuclear metrology laboratory are detailed in the following sections.

Cyclotron

The Arronax accelerator is a four-sector isochronous cyclotron with a maximum vertical magnetic field of 1.64 T, designed to accelerate multiple particle types: protons (H^+), alpha particles (He^{2+}), and deuterons (D^+). It can deliver kinetic energies ranging from 30 to 70 MeV for protons, 68 MeV for alpha particles, and up to 35 MeV for deuterons. The properties of the cyclotron are resumed in Table 3.4. The facility includes eight beamlines arranged radially around the cyclotron, suitable for various experimental and production purposes (GIP ARRONAX [2024]).

[3] ARRONAX stands for "Accélérateur pour la Recherche en Radiochimie et Oncologie à Nantes Atlantique" in French, which translates to "Accelerator for Radiochemistry and Oncology in Nantes Atlantique" in English. The name also references the character Aronnax from Jules Verne's novel "Twenty Thousand Leagues Under the Seas"; Jules Verne was born in Nantes in 1828.

Figure 3.23: Hot room of the radiochemistry laboratory of LASA.

The cyclotron features a 30.45 MHz radiofrequency, with RF cavities composed of two dees at 65 kV. The diameter of the cyclotron is approximately 4 m, with a height of 3.6 m and a weight of around 145 tons. The accelerator is located in a central vault, separated by thick walls of up to 4 meters from target and experimental vaults.

Table 3.4: Characteristics of the Arronax Cyclotron (from Haddad et al. [2008]).

Particle Type	Energy (MeV)	Maximum Intensity (µA)
Protons (H^+)	30 - 70	375 x 2
Alpha Particles (He^{2+})	68	70
HH^+	35	50
Deuterons (D^+)	15 - 35	50

The accelerator utilizes a pulsed mode system to control the number of particle bunches and includes multiple sections for particle source, injection, pulsation, acceleration, and extraction. The beamlines consist of magnetic elements such as dipoles and quadrupoles to maintain particle flow in a vacuum tube.

The Arronax cyclotron delivers particle beams to six experimental vaults named AX, A1, A2, P1, P2, and P3 (Figure 3.24). Due to the different extraction methods for negative and positive ions, protons and deuterons are available in all vaults, while alpha particles are limited to vaults A1, A2, and AX. Vaults A1, A2, P1, P2, and P3 focus on radionuclide production, equipped with target systems and a pneumatic transfer (rabbit) system connected to hot cells. Vault P1 is also used for research and development of high-intensity beams. Vault AX contains three beamline is dedicated to radiolysis, radiobiology, physics experiments (including cross-section measurements), and student training, featuring also a vertical beamline for specific experiments. The alpha beam in vault AX can be pulsed, delivering up to 7×10^6 alpha particles per pulse with a width of 3.3 ns, and a variable delay between pulses (from 1 ms to a few seconds) (Haddad et al. [2008]).

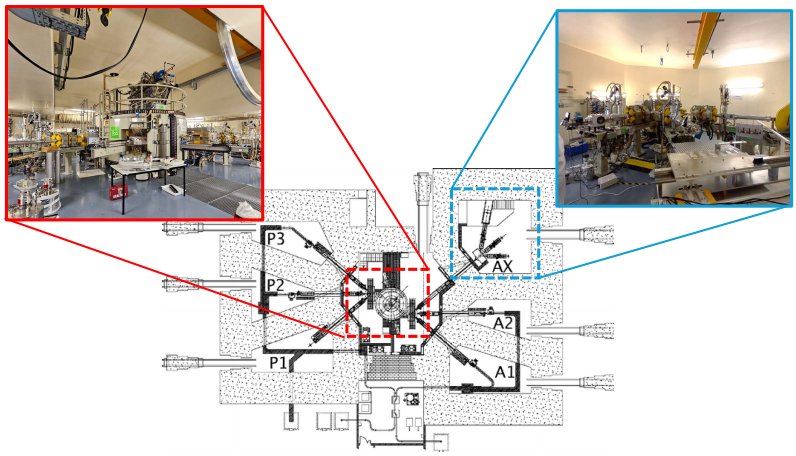

Figure 3.24: Map of the GIP ARRONAX beam lines (taken from Haddad et al. [2008]); pictures of the cyclotron and AX vaults are shown.

Target station for cross-section measurements

Within vault AX, there is a target station for cross-section measurements (see Figure 3.25). It consists of a movable base that allows for quick setup and dismantling of the experiment. A target holder is mounted on this base, with an adjustable distance from the beamline exit (typically set to 6 cm). The target is air-cooled, and after irradiation, it can be remotely dropped into lead shielding for safe extraction. A beam dump monitors beam intensity during irradiation, while a webcam provides visual feedback on the beam shape using an alumina foil with radioluminescent properties.

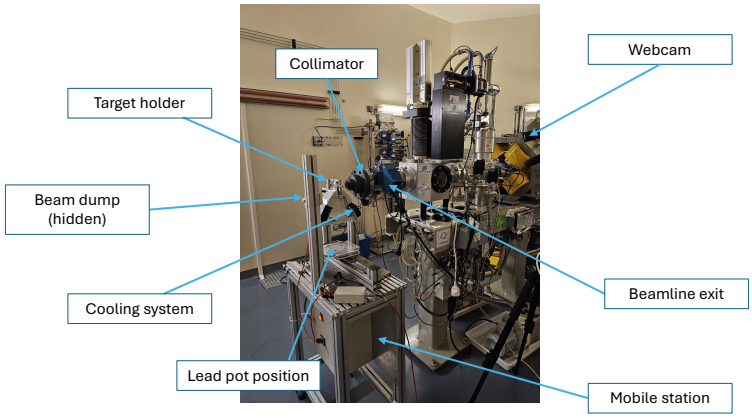

Figure 3.25: Picture of the target station for cross-section measurements at GIP ARRONAX.

Nuclear metrology laboratory

The nuclear metrology laboratory is equipped with three n-type HPGe detectors (Canberra Industries Inc., Meriden, CT, USA) and an Si-based alpha spectrometer with two vacuum cells. One of the HPGe detectors is coupled with an electronic system that allows automatic sample changes without human supervision; however, this system is not available for the geometry used in cross-section measurements. Samples are typically positioned about 19 cm from the detector. A longer distance geometry (50 cm from the detector) is also possible, but no shielding is available in this configuration.